Научном већу Института за физику у Београду

Београд, 01.08.2024.

Предмет:

Молба за покретање поступка за стицање звања истраживач-сарадник

На основу испуњености услова предвиђених Правилником о стицању истраживачких и научних звања, прописаног од стране ресорног Министарства, молим Научно веће института за физику у Београду да покрене поступак за мој избор у звање истраживач сарадник.
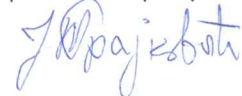
У прилогу достављам:

1. Мишљење руководиоца лабораторије са предлогом комисије за избор у звање

2. Стручну биографију

3. Преглед научних активности

4. Списак научних радова

5. Потврду о статусу студента докторских студија и пријављеној теми докторске

дисертације

6. Копије диплома основних и матер студија

7. Копије научних радова

С поштовањем,

Јелена Трајковић

истраживач приправник

Научном већу Института за физику у Београду

Предмет: Мишљење руководиоца лабораторије о избору Јелене Трајковић у звање истраживач сарадник

Јелена Трајковић је запослена на Институту за физику у Београду. Ангажована је у Лабораторији за истраживање у области електронских материјала, где израду докторске дисертације обавља под руководством др Анђелије Илић. С обзиром да испуњава све предвиђене услове у складу са Законом о науци и страживањима и Правилником о стицању истраживачких и научних звања Министарства науке, технолошког развоја и иновација, сагласан сам са покретањем поступка за избор Јелене Трајковић у звање истраживач сарадник.

др Небојша Ромчевић
научни саветник
руководилац Лабораторије за истраживање
у области електронских материјала

Научном већу Института за физику у Београду

За састав комисије за избор Јелене Трајковић у звање истраживач сарадник предлажем:

(1) др Анђелија Илић, научни саветник, Институт за физику у Београду

(2) др Предраг Коларж, научни саветник, Институт за физику у Београду

(3) проф. др Бећко Касалица, редовни професор, Универзитет у Београду, Физички факултет

Биографски подаци кандидаткиње

Јелена Трајковић је рођена 10. 12. 1994. године у Лазаревцу, где је завршила основну школу Свети Сава и средњу техничку школу - Финансијски техничар. Школске 2013/2014 године уписала је Физички факултет Универзитета у Београду, смер Општа физика. Дипломирала је на Физичком факултету 27. 09. 2017. године са просечном оценом 8,55.

Школске 2017/18 године уписала је мастер студије физике, смер Општа физика. Други семестар школске 2018/2019 године проводи на Политехничком Универзитету у Мадриду у оквиру студентске размене. Написала је истраживачки мастер рад: "Analitical opacity formulas for He, O, Fe and Xe", под руководством проф. Емилија Мингеза (Emilio Minguez Torres). Мастер студије физике, завршила је 28. 09. 2020. године са просечном оценом 9,25. Течно говори два светска језика - енглески и шпански.

За време и након завршетка мастер студија, две године је била запослена у настави физике у XIII београдској гимназији, Земунској гимназији и средњој музичкој школи Ватрослав Лисински.

Докторске студије, уже научне области: Примењена физика, уписала је школске 2021/2022 године на Физичком факултету у Београду. Свој научно истраживачки рад остварује у лабораторији за истраживање у области електронских материјала, Института за физику у Београду. Тема докторске дисертације под руководством др Анђелије Илић под називом "Униформни и неуниформни низови дискретних извора ОАМ зрачења за формирање снопа и мултиплексирање помоћу ОАМ модова" одбрањена је на колегијуму физичког факултета, 01. новембра 2023. године.

Преглед научне активности кандидаткиње

Главна област истраживања Јелене Трајковић су таласи са орбиталним угаоним моментом, у литератури познатији као ОАМ (Orbital Angular Momentum) таласи. Истраживање обухвата пројектовање и оптимизацију различитих низова дискретних извора ОАМ таласа са униформним и неуниформним распоредима елемената. Поред главне области, њено истраживање укључује, физику јона, компјутерско моделовање као и компјутерску обраду медицинских слика.

Други семестар школске 2018/2019 године мастер студија проводи на Политехничком Универзитету у Мадриду у оквиру студентске размене. Написала је истраживачки мастер рад: "Analitical opacity formulas for He, O, Fe and Xe", под руководством проф. Емилија Мингеза (Emilio Minguez Torres).

На Институт за физику у Београду долази у децембру 2021 године, где се као истраживач приправник бави истраживачким радом у Лабораторији за истраживање у области електронсих материјала. Тема докторске дисертације под руководством др Анђелије Илић под називом "Униформни и неуниформни низови дискретних извора ОАМ зрачења за формирање снопа и мултиплексирање помоћу ОАМ модова" одбрањена је на колегијуму физичког факултета, 01. новембра 2023. године. Касније је назив теме предлогом комисије измењен у „Дискретни извори таласа са орбиталним угаоним моментом (ОАМ) за мултиплексирање ОАМ модовима".

Учесник је на два пројекта Фонда за науку, једног билатералног пројекта и руководилац пројекта за младе истраживаче "SEED". У склопу пројекта ЗЕЛЕНИ под акронимом "IonCleanTech" Фонда за науку бави се физиком јона. На ПРИЗМА пројекту "ToxoReTREAT", бави се компјутерском обрадом медицинских слика. У оквиру билатералног DAAD пројекта "OAM MUX", као и пројекта „SEED" бави се истраживањем таласа са орбиталним угаоним моментом, што је и њена примарна област истраживања. У току три године рада на Институту за Физику, учествовала је на три конференције са шест радова, од којих су четири рада из примарне области истраживања. Њен фокус у даљем истраживању биће развој и реализација конфигурација ОАМ низова са веома високом ефикасношћу генерисања жељених ОАМ таласа. То укључује развој метода и приступа у компјутерском моделовању ОАМ низова, анализу перформанси, оптимизацију параметара, као и развој прототипова и експерименталну верификацију појединих примера таквих низова.

Списак објављених радова кандидаткиње

Категорија M$_{21a}$:

1. V. Makević, I. D. Milovanovich, N. Popovac, R. Janković**, J. Trajković**, A. Vuković, B. Milošević, J. Jevtić, S. R. de Luka, A. Ž. Ilić, "Fractal parameters as independent biomarkers in the early diagnosis of pediatric onset inflammatory bowel disease", *Fractal Fract*., vol. 7, Aug. 2023, p. 619. (DOI: https://doi.org/10.3390/fractalfract7080619)

2. N. Bauman, J. Srbljanović, I. Č. Čalovski, O. Lijeskić, V. Ćirković, **J. Trajković**, B. Bobić, A. Ž. Ilić, T. Štajner, "Structural Characterization of Toxoplasma gondii Brain Cysts in a Model of Reactivated Toxoplasmosis Using Computational Image Analysis", *Fractal Fract*., vol. 8(3), Mar. 2024, p. 175. (DOI: https://doi.org/10.3390/fractalfract8030175)

Категорија M$_{21}$:

3. A. Ž. Ilić, **J. Z. Trajković**, S. V. Savić, M. M. Ilić, "Near-field formation of the UCA-based OAM EM fields and short-range EM power flux profiles," *Journal of Physics A: Mathematical and Theoretical*, vol. 56, no. 25, May 2023, p. 255701.
(DOI: https://doi.org/10.1088/1751-8121/acd5bf)

Категорија M$_{22}$:

4. A. Ž. Ilić, **J. Z. Trajković**, S. V. Savić, M. M. Ilić, "Investigation of the OAM EM wave tissue irradiation at milimeter-wave frequencies", *Applied Radiation and Isotopes,* vol. 207, May 2024 (DOI: https://doi.org/10.1016/j.apradiso.2024.111261)

Категорија M$_{34}$:

5. A. Ž. Ilić, **J. Z. Trajković**, S. V. Savić, and M. M. Ilić, "Free-space OAM wave transmission: a short dipole modeling study," in Abstract Book of *IX International School and Conference on Photonics, PHOTONICA2023*, Belgrade, Serbia, August 28 – Sept. 01, 2023, p.100.(Available: https://www.photonica.ac.rs/docs/Book of Abstracts (online).pdf)

6. **J. Z. Trajković**, A. Ž. Ilić, S. V. Savić, N. Maletić, E. Grass, and M. M. Ilić, "OAM mode quality comparisons for discrete EM radiating sources", in Abstract Book of *IX International School and Conference on Photonics, PHOTONICA2023*, Belgrade, Serbia, Aug. 28–Sept. 1, 2023, p.101.(Available: https://www.photonica.ac.rs/docs/Book of Abstracts (online).pdf)

7. **J. Trajković**, S. Savić, M. Ilić, A. Ilić, "Investigation of the OAM EM wave interaction with tissue at microwave and millimeter wave frequencies," in Abstract Book of *International Conference On Radiation Applications (RAP 2023)*, May 29–June 2, 2023, Hellenic Centre for Marine Research (HCMR), Anavyssos, Attica, Greece, page 128. (Available: https://www.rap-conference.org/23/RAP_2023_Book_of_Abstracts.pdf)

8. **J. Trajković**, , S. Savić, M. Ilić, A. Ilić, "Transmission and attenuation of the milimeter-wave OAM beams through the layers of tissue", in Abstract Book of *International Conference On Radiation Applications (RAP 2024),* June 10-12, 2024, University of Granada, Spain, page. 157.
    (Available: https://www.rap-conference.org/24/RAP_2024_Book_of_Abstracts.pdf)

9. S. Mijatović , I. Aranđelović , A. Radalj, M. Janković , S. Đoković , **J. Trajković** , A. Ilić, P. Kolarž, "New experimental setup for exposure of gas-phase bio-aerosols to small air ions", in Abstract Book of *International Conference On Radiation Applications (RAP 2024),* June 10-12, 2024, University of Granada, Spain, page. 201.
    (Available: https://www.rap-conference.org/24/RAP_2024_Book_of_Abstracts.pdf)

10. **J. Trajković**, A. Ilić, J. Srbljanović , O. Lijeskić, N. Bauman , Đ. Zlatković, D. Vujić, V. Dobričić, B. Bobić, T. Štajner, "In vitro experimental model of reactivated toxoplasmosis through the prism of computational image analysis" in Abstract Book of *International Conference On Radiation Applications (RAP 2024),* June 10-12, 2024, University of Granada, Spain, page. 204.
    (Available: https://www.rap-conference.org/24/RAP_2024_Book_of_Abstracts.pdf)

УБ

Република Србија

Универзитет у Београду
Физички факултет, Београд

Оснивач: Република Србија
Дозволу за рад број 612-00-02666/2010-04 од 10. децембра 2010.
године је издало Министарство просвете и науке Републике Србије

Диплома

Јелена, Зоран, Трајковић

рођена 10. децембра 1994. године у Лазаревцу, Република Србија, уписана

школске 2013/2014. године, а дана 27. септембра 2017. године завршила је основне

академске студије, првог степена, на студијском програму Општа физика, обима

180 (сто осамдесет) бодова ЕСПБ са просечном оценом 8,55 (осам и 55/100).

На основу тога издаје јој се ова диплома о стеченом високом образовању и стручном називу

физичар

Број: 8595200

У Београду, 19. септембра 2018. године

Декан
Проф. др Јаблан Дојчиловић

Ректор
Проф. др Владимир Бумбаширевић

00086402

Република Србија
Универзитет у Београду
Оснивач: Република Србија
Дозволу за рад број 612-00-02666/2010-04 од 12. октобра 2011.
године је издало Министарство просвете и науке Републике Србије
Физички факултет, Београд
Оснивач: Република Србија
Дозволу за рад број 612-00-02409/2014-04 од 8. септембра 2014. године је издало
Министарство просвете, науке и технолошког развоја Републике Србије

Диплома

Јелена, Зоран, Трајковић

рођена 10. децембра 1994. године, Лазаревац, Република Србија, уписана школске

2017/2018. године, а дана 28. септембра 2020. године завршила је мастер

академске студије, другог степена, на студијском програму Општа физика,

обима 120 (сто двадесет) бодова ЕСПБ са просечном оценом 9,25 (девет и 25/100).

На основу тога издаје јој се ова диплома о стеченом високом образовању и академском називу
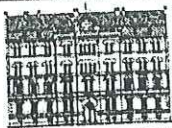
мастер физичар

Број: 13225600

У Београду, 1. фебруара 2022. године

Декан
Проф. др Иван Белча

Ректор
Проф. др Владан Ђокић

00132570

ПРЕДЛОГ ТЕМЕ ДОКТОРСКЕ ДИСЕРТАЦИЈЕ КОЛЕГИЈУМУ ДОКТОРСКИХ СТУДИЈА

Школска година
2023/2024

Подаци о студенту

Име	Јелена	Научна област дисертације	
Презиме	Трајковић	Примењена физика	
Број индекса	8022/2021		

Подаци о ментору докторске дисертације

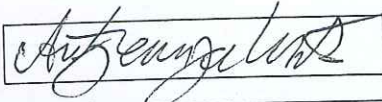|			
Име	Анђелија	Научна област	Примењена физика
Презиме	Илић	Звање	виши научни сарадник
		Институција	Институт за физику Београд

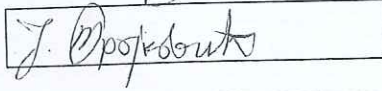### Предлог теме докторске дисертације

Наслов

Униформни и неуниформни низови дискретних извора ОАМ зрачења за формирање снопа и мултиплексирање помоћу ОАМ модова

Уз пријаву теме докторске дисертације Колегијуму докторских студија, потребно је приложити следећа документа:

1. Семинарски рад (дужине до 10 страница)
2. Кратку стручну биографију писану у трећем лицу једнине
3. Фотокопију индекса са докторских студија

Потпис ментора ⟨signature⟩

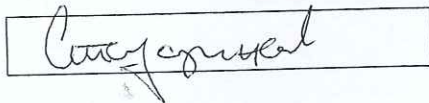Датум 24. 10. 2023   Потпис студента J. Ђукановић

Мишљење Колегијума докторских студија

Након образложења теме докторске дисертације Колегијум докторских студија је тему

прихватио ☑   није прихватио ☐

Датум   Продекан за науку Физичког факултета

01. 11. 2023   ⟨signature⟩

Република Србија
Универзитет у Београду
Физички факултет
Број индекса: 2021/8022
Датум: 03.11.2023.

На основу члана 29. Закона о општем управном поступку и службене евиденције издаје се

УВЕРЕЊЕ О ПОЛОЖЕНИМ ИСПИТИМА

Јелена Трајковић, име једног родитеља Зоран, рођена 10.12.1994. године, Лазаревац, Република Србија, уписана школске 2021/2022. године на докторске академске студије, школске 2023/2024. године уписана на статус финансирање из буџета, студијски програм Физика, током студија положила је испите из следећих предмета:

Р.бр.	Шифра	Назив предмета	Оцена	ЕСПБ	Фонд часова**	Датум
1.	ДС15ВО2	Монте Карло симулације у физици	9 (девет)	15	I:(8+0+0)	23.09.2022.
2.	ДС15ПФ7	Пројектовање оптичких система	10 (десет)	15	I:(8+0+0)	22.09.2022.
3.	ДС15ФРНД1	Рад на докторату 1. део	П.	30	I:(0+0+12) II:(0+0+12)	
4.	ДС15ПФ10	Примена плазме у биологији и медицини	10 (десет)	15	III:(8+0+0)	15.06.2023.
5.	ДС15ФЛ8	Макро и нано фотонске структуре у биофизици и оптичким комуникацијама	9 (девет)	15	III:(8+0+0)	22.09.2023.
6.	ДС15ФРНД2	Рад на докторату 2. део	П.	30	III:(0+0+12) IV:(0+0+12)	

*   - еквивалентиран/признат испит.
** - Фонд часова је у формату (предавања+вежбе+остало).

Општи успех: 9,50 (девет и 50/100) , по годинама студија (9,50, 9,50, /).

Овлашћено лице факултета
_____

Република Србија
Универзитет у Београду
Физички факултет
Д.Бр.2021/8022
Датум: 17.10.2023. године

На основу члана 161 Закона о општем управном поступку и службене евиденције издаје се

УВЕРЕЊЕ

Трајковић (Зоран) Јелена, бр. индекса 2021/8022, рођена 10.12.1994. године, Лазаревац, Република Србија, уписана школске 2023/2024. године, у статусу: финансирање из буџета; тип студија: докторске академске студије; студијски програм: Физика.

Према Статуту факултета студије трају (број година): три.
Рок за завршетак студија: у двоструком трајању студија.

Ово се уверење може употребити за регулисање војне обавезе, издавање визе, права на дечији додатак, породичне пензије, инвалидског додатка, добијања здравствене књижице, легитимације за повлашћену вожњу и стипендије.

Овлашћено лице факултета
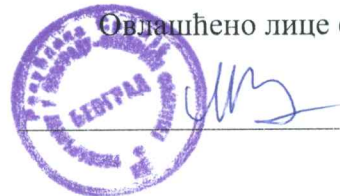
_____

Fractal Parameters as Independent Biomarkers in the Early Diagnosis of Pediatric Onset Inflammatory Bowel Disease

Vedrana Maković [1,†], **Ivan D. Milovanovich** [2,†], **Nevena Popovac** [2], **Radmila Janković** [3], **Jelena Trajković** [4,5], **Andrija Vuković** [1], **Bojana Milosević** [5], **Jovan Jevtić** [3], **Silvio R. de Luka** [1] and **Andjelija Ž. Ilić** [4,*]

1. Faculty of Medicine, Department of Pathological Physiology, University of Belgrade, Dr Subotica 1, 11000 Belgrade, Serbia; vedrana.parlic@med.bg.ac.rs (V.M.); andrija.vukovic@med.bg.ac.rs (A.V.); silvio.de-luka@med.bg.ac.rs (S.R.d.L.)
2. University Children's Hospital, University of Belgrade, Tiršova 10, 11000 Belgrade, Serbia; ivan.milovanovic@med.bg.ac.rs (I.D.M.); endoskopija@udk.bg.ac.rs (N.P.)
3. Faculty of Medicine, Institute of Pathology, University of Belgrade, Dr Subotica 1, 11000 Belgrade, Serbia; radmila.jankovic@med.bg.ac.rs (R.J.)
4. Institute of Physics Belgrade, University of Belgrade, Pregrevica 118, 11080 Belgrade, Serbia; jelena.trajkovic@ipb.ac.rs
5. Faculty of Physics, University of Belgrade, 11000 Belgrade, Serbia; milosevicbojana96@gmail.com
* Correspondence: andjelijailic@ieee.org; Tel.: +381-113713164
† These authors contributed equally to this work.

Abstract: Inflammatory bowel disease (IBD), which encompasses two different phenotypes—Crohn's disease (CD) and ulcerative colitis (UC)—consists of chronic, relapsing disorders of the gastrointestinal tract. In 20–30% of cases, the disease begins in the pediatric age. There have been just a few studies that used fractals for IBD investigation, but none of them analyzed intestinal cell chromatin. The main aim of this study was to assess whether it is possible to differentiate between the two phenotypes in pediatric patients, or either of the phenotypes versus control, using the fractal dimension and lacunarity of intestinal cell chromatin. We analyzed nuclei from at least seven different intestinal segments from each group. In the majority of colon segments, both the fractal dimension (FD) and the lacunarity significantly differed between the UC group and CD group, and the UC group and control group. In addition, the ileocecal valve and rectum were the only segments in which CD could be differentiated from the controls based on the FD. The potential of the fractal analysis of intestinal cell nuclei to serve as an observer-independent histological tool for ulcerative colitis diagnosis was identified for the first time in this study. Our results pave the way for the development of computer-aided diagnosis systems that will assist the physicians in their clinical practice.

Keywords: fractal dimension; lacunarity; medical image analysis; nucleus chromatin architecture; inflammatory bowel disease

1. Introduction

Over the past two decades, medical image analysis has become an invaluable tool in the field of life sciences. Amongst other descriptors, fractal-based parameters have been used with success. As pointed out in [1], many natural and man-made objects can be characterized using the classical geometry and integer dimension; however, the random growth and/or branching of natural objects, at different scales, can be described in a sufficiently precise and concise way only by means of a non-integer fractal dimension. Some of the representative examples include a fern leaf, the branching in human lungs, a broccoli head, and the electric discharge in a storm [1]. In fractal objects, self-similarity at varying scales can be observed. Applications of fractal analysis to biomedical problems have been well established in ophthalmology, in exhibiting the fractal structure of vascular networks, and in the study of branching patterns of nerve dendrites, as well as in the studies of altered tissue and cell characteristics in cancers [1–6].

The dependences of the structural or functioning-related parameters of interest on the scale can be expressed by the power-law equations [1,7,8]. The fractal dimension (FD), which corresponds to the first-order mass moment of probability of finding a certain fractal measure amount at a certain scale [9,10], can be easily determined from the power-law dependence. In medical image analysis, the FD provides a statistical index that quantifies complexity and pattern reproducibility. As the biological specimens exhibit pronounced self-similarity at different scales, the FD is being increasingly used for diagnostic purposes in medicine [3]. Another parameter, which is often used alongside the FD, is the lacunarity (also sometimes referred to as "gappiness" or inhomogeneity). The lacunarity is calculated by taking into account the first-order and second-order mass moments of probability of finding a certain fractal measure amount at a certain scale [9]. It is a measure of heterogeneity and translational and rotational invariance that describes the space-filling property of fractals [9]. It is highly useful as an additional parameter to differentiate natural surfaces and textures with the same or similar fractal dimension [6,11].

In the field of medical science, the concept of fractals has been used for both image [1–6,12–14] and signal [15–18] analysis. The fractal feature-based image analysis employed so far in gastroenterology has shown promising results in cancer research [19–23] and has helped in the analysis of wireless capsule endoscopy [24] and colonoscopy images [25]. On the other hand, fractal-based signal analysis methods have been applied in gastroenterology in the study of digestion [26], colonic pressure [27], and intestinal sound analysis [28]. Although it produced very good results in the investigations of other intestinal pathologies, fractal-based methodology has rarely been used in inflammatory bowel disease (IBD) research [11,29,30].

The FD of nuclear chromatin [31,32] proved to be a sensitive parameter capable of the early detection of fine structural and textural changes in the cell nucleus. Nuclear chromatin FD changes have been found during the processes of cell differentiation, development, mitosis, apoptosis, aging, and cancer development [33,34]. Lacunarity has also been employed for chromatin structure evaluation in, among others, studies of apoptosis, postnatal development, and aging. In many of the studies, lacunarity has been inversely related to the FD, i.e., there has been a negative correlation between the FD and lacunarity, although, depending on the underlying processes, this association does not apply in general [33].

IBD, which encompasses two major phenotypes—Crohn's disease (CD) and ulcerative colitis (UC)—consists of chronic, relapsing disorders of the gastrointestinal tract [35,36]. Continuous mucosal inflammation that starts from the rectum and proceeds to more proximal colon segments, with variability in extent, is typical for UC [37]. On the other hand, discontinuous transmural granulomatous inflammation occurring at any part of the gastrointestinal tract characterizes CD [38]. The disease etiology is still not fully elucidated, but it has become clear that genetic factors, environment, diet, and changes in the microbiome are implicated in the pathogenesis. CD can affect any part of the gastrointestinal system, although it is most often evidenced in the terminal part of small intestine (terminal ileum) and the colon. On the other hand, UC is a disease restricted to the colon and rectum [35]. Both phenotypes sometimes display extraintestinal manifestations, which might stem from factors such as chronic inflammation or nutrient malabsorption [36]. In 20–30% of cases the disease begins in the pediatric age. We are currently witnessing an increase in incidence in the pediatric population [39]. Pediatric ulcerative colitis sometimes has an atypical endoscopic presentation like rectal sparing or patchy disease, which makes the differentiation between the two IBD phenotypes far more challenging [40]. The new European Crohn's and Colitis Organization (ECCO) guidelines [41] stress the importance of novel and possibly noninvasive biomarkers in diagnostics. The only recommended biomarker of intestinal inflammation so far is fecal calprotectin. Hence, there is a great demand for the invention of new efficient biomarkers for IBD, which could be combined with the standard medical procedures [42].

There have been just a few studies [11,29,30] which have employed fractals for IBD investigation. To the best of our knowledge, the fractals have not yet been applied in the

analysis of the chromatin structure in the intestinal cells. However, there are indications that alterations in nuclear chromatin are very likely to occur in many functional gastrointestinal and motility disorders [43]. It has been demonstrated that the gene regulation by the microbiota is linked to DNA methylation and chromatin accessibility changes [44]. The underlying epigenetic mechanisms have recently been recognized as highly important in the pathogenesis of inflammatory bowel disease (IBD). Therefore, possible alterations of the fractal parameters describing the intestinal cell chromatin structure need to be investigated. The main aim of this study was to assess whether it is possible to differentiate between children with one of the two IBD phenotypes and children in a control group and to differentiate between the two phenotypes, based on the intestinal cell chromatin fractal dimension and lacunarity. Also, we checked the potential and the methods of application of fractal analysis as an observer-independent tool for IBD diagnosis.

2. Materials and Methods

2.1. Patients

The current study was conducted on children newly diagnosed with IBD (14 cases of CD and 10 cases of UC). The control group (N = 16) comprised children with irritable bowel syndrome (IBS) (without intestinal inflammation) or healthy controls. Seven tissue samples per patient were obtained by colonoscopy, corresponding to seven intestinal segments. Each sample contained one to four endoscopic biopsies. The samples belonged to the terminal ileum, cecum, ascending, transversal, descending, and sigmoid colon, and rectum, respectively. In cases when the ileocecal valve appeared affected, an additional 8th sample from the valve was obtained.

2.2. Intestinal Tissue Preparation and Staining

Intestinal tissue was fixed in 4% neutral buffered formaldehyde. The tissues were dehydrated in graded ethanol, according to the routine procedure, and then embedded in paraffin blocks and sectioned. The paraffin tissue blocks were cut into 4 μm thick sections and stained with hematoxylin and eosin.

2.3. Medical Image Preprocessing

The following image preprocessing procedure was employed for each intestinal segment. Four different micrographs containing at least one intestinal crypt each were acquired using the Olympus DP70 camera (Olympus BX50, Tokyo, Japan) and Analysis 5.0 software (SoftImaging System, Olympus, Tokyo, Japan). The total microscope magnification was 1000 times. All the micrographs were saved as TIFF files (dimensions 4080 × 3072 pixels, resolution 200 DPI, bit depth 24). Using the polygon tool of the ImageJ software (NIH, Bethesda, MD, USA), twenty crypt cell nuclei per segment were acquired for every patient and transferred to the white background images (500 × 500 pixels). Such newly acquired micrographs of nuclei were converted to monochromatic images using the Colour Deconvolution plugin of the ImageJ software [45,46], with an option denoted as H&E 2. The hematoxylin component (R: 0.49015734, G: 0.76897085, B: 0.41040173) is dominant for nuclei; it was recorded as an 8-bit grayscale image and used in further analyses.

2.4. Niblack Thresholding

Prior to fractal analysis, all the nuclei images underwent local Niblack thresholding and conversion to binary images. The local threshold value at each pixel was calculated by taking into account the neighborhood around that pixel and summing the neighborhood mean value of the grayscale intensity with the weighted standard deviation of the grayscale intensity. Both the window radius defining a neighborhood size and the weighting coefficient have to be adjusted empirically. The default value of the weighting coefficient is 0.2 for bright objects on a dark background and −0.2 for dark objects on a light background. In our case, the default coefficient provided very good results for all the images, and it was not changed. A window of a radius of w = 6 px, chosen empirically, was centered around

each considered pixel. The local threshold at each pixel was then calculated according to the expression:

$$t_{\text{Ni}} = \mu(w) - 0.2 \cdot \sigma(w) \tag{1}$$

In (1), $\mu(w)$ and $\sigma(w)$ correspond to the mean and standard deviation of the grayscale intensities within a local neighborhood window of size w. Thus, a different threshold for every pixel is based on the grayscale properties of the neighboring pixels [47]; this was employed to better outline the spatial distribution of two types of chromatin—euchromatin (lighter) and heterochromatin (darker in appearance) [33]. Specifically, the altered spatial distribution of these regions seems to appear macroscopically mostly through altered nuclei texture.

2.5. Fractal Analysis

Fractal analysis was carried out on binary images using the FracLac plugin (A. Karperien, Charles Sturt University, Australia) for the ImageJ software [48]. The fractal dimension (D_b) was calculated using the box counting method as well as the cumulative mass method, with agreement of the results for the same sets of grids. We applied a scaled series 7/8, meaning that an enlargement of a consequent grid cell size was about 1/8. By using a scaled series, a sufficient number of relatively dense data points for fitting the regression lines was easily obtained. Here, a total of 18 grid cell sizes were used to obtain data points for fitting the regression curves to describe the scale–count power law dependence. Specifically, grid cells sized $\varepsilon \in \{5, 6, 7, 8, 9, 10, 12, 14, 16, 18, 20, 23, 27, 30, 35, 40, 46, 52\}$ px were used in both the box counting method and the cumulative mass method. Figure 1 shows an example binary image of a nucleus and also illustrates the typical nucleus size and the look of the chromatin texture, covered by grid cells of different sizes, ε. Typical grid cell arrangements are shown for four out of the eighteen utilized sizes, as denoted above each of the four plots. Twelve random grid origin positions per nucleus, per each grid cell size, were used.
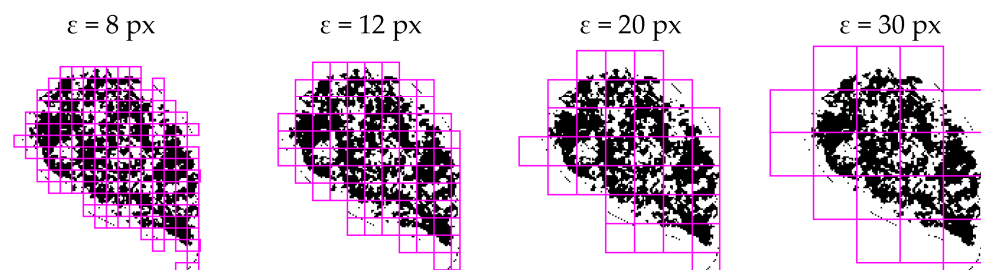

$\varepsilon = 8$ px $\varepsilon = 12$ px $\varepsilon = 20$ px $\varepsilon = 30$ px

Figure 1. Grids of different grid cell sizes, ε, used to cover a binary two-dimensional (2D) object while obtaining data points for the scale–count dependence. The example nucleus shown corresponds to the 2nd patient in the CD group.

A change in the number of non-empty grid cells, $N(\varepsilon)$, with a change in the grid cell size, ε, was modeled by a best-fit regression line, whose slope served to estimate D_b.

$$D_b = -\lim_{\varepsilon \to 0} \frac{\ln N(\varepsilon)}{\ln \varepsilon} \tag{2}$$

The cumulative mass method makes an assessment of the probability of finding m pixels inside the cell of a size ε, $P(m, \varepsilon)$, by counting the pixels inside the grid cells and normalizing the obtained pixel count data for the total probability of one, $\sum_m P(m, \varepsilon) = 1$.

The first-order mass moment, $M(\varepsilon)$, and the second-order mass moment, $M^2(\varepsilon)$, were obtained as:

$$M(\varepsilon) = \sum_m m P(m, \varepsilon), \ M^2(\varepsilon) = \sum_m m^2 P(m, \varepsilon) \tag{3}$$

The FD was then estimated from the $(\varepsilon, M(\varepsilon))$ data, as:

$$D_{\mathrm{m}} = \lim_{\varepsilon \to 0} \frac{\ln M(\varepsilon)}{\ln \varepsilon} \tag{4}$$

In both cases, the adequacy of the regression line fit was estimated based on the correlation coefficient, r^2, which was close to one in all cases, confirming almost linear data and high FD estimate accuracy. The lacunarity is calculated from the first-order and second-order mass moments as:

$$\lambda(\varepsilon) = \frac{\langle M^2(\varepsilon) \rangle - \langle M(\varepsilon) \rangle^2}{\langle M(\varepsilon) \rangle^2} \tag{5}$$

2.6. Statistical Analysis

The normality of distribution was tested with the Shapiro–Wilk test. Depending on the type of variables and the normality of the distributions, the results are presented as frequency (percent), mean ($\pm$SD), and median (range). Statistical hypotheses were tested using the ANOVA, Kruskal–Wallis, and Mann–Whitney tests and the chi square test. The statistical hypotheses were analyzed at the significance level of 0.05. Statistical data analysis was performed using IBM SPSS Statistics 22 (IBM Corporation, Armonk, NY, USA).

3. Results

3.1. Demographic and Clinical Characteristics

The demographic and clinical characteristics of the study participants, i.e., the pediatric patients used in this particular study, are shown in Table 1.

Table 1. Demographic and clinical characteristics of IBD groups and control patients.

Variable	Control	UC	CD	Overall *p*
Gender				
Male	60.0%	60.0%	78.6%	0.498
Female	40.0%	40.0%	21.4%	
Age	11.3 ± 5.1	14.4 ± 3.3	12.1 ± 4.8	0.271
PUCAI		32.5 ± 19.0		
PCDAI			17.5 ± 6.3	

Abbreviations: CD—Crohn's disease; UC—ulcerative colitis; PUCAI—Pediatric Ulcerative Colitis Activity Index; PCDAI—Pediatric Crohn's Disease Activity Index.

3.2. Histological Activity

The histological activities of UC and CD are represented with the corresponding regional histological activity score and are presented in Table 2 and Figure 2 (Nancy score for UC) and Table 3 and Figure 3 (GHAS score for CD).

Table 2. Regional Nancy score in six different colon segments.

Segment	Nancy 0, 1	Nancy 2	Nancy 3	Nancy 4
S2	1 (10.0%)	3 (30.0%)	5 (50.0%)	1 (10.0%)
S3	2 (20.0%)	4 (40.0%)	2 (20.0%)	2 (20.0%)
S4	2 (22.2%)	3 (33.3%)	4 (44.4%)	
S5	2 (20.0%)	3 (30.0%)	5 (50.0%)	
S6	1 (10.0%)	3 (30.0%)	5 (50.0%)	1 (10.0%)
S7	2 (20.0%)	2 (20.0%)	5 (50.0%)	1 (10.0%)

Segment notation: S2—cecum; S3—ascending colon; S4—transversal colon; S5—descending colon; S6—sigmoid colon; S7—rectum.
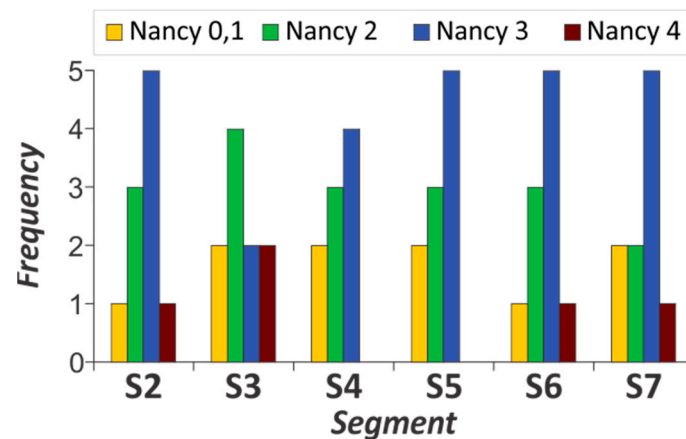
Figure 2. Regional Nancy score in six different colon segments.

Table 3. Regional GHAS score in seven different colon segments.

Segment	GHAS 1,2,3,4	GHAS 5,6,7	GHAS 8,9,10	GHAS 11–16
S1	3 (21.43%)	6 (42.86%)	4 (28.57%)	1 (7.14%)
S2	6 (42.86%)	5 (35.71%)	1 (7.14%)	2 (14.29%)
S3	6 (42.86%)	4 (28.57%)	2 (14.29%)	2 (14.29%)
S4	4 (28.57%)	4 (28.57%)	5 (35.71%)	1 (7.14%)
S5	7 (50.00%)	2 (14.29%)	2 (14.29%)	3 (21.43%)
S6	5 (35.71%)	4 (28.57%)	3 (21.43%)	2 (14.29%)
S7	7 (50.00%)	3 (21.43%)	4 (28.57%)	

Segment notation: S1—terminal ileum; S2—cecum; S3—ascending colon; S4—transversal colon; S5—descending colon; S6—sigmoid colon; S7—rectum.
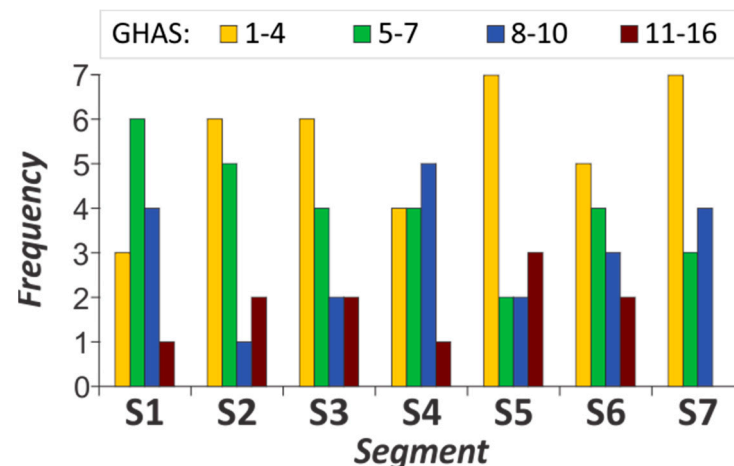

Figure 3. Regional GHAS score in seven different colon segments.

3.3. Fractal Dimension

We estimated the FD of the epithelial cell nuclei to assess potential differences in the chromatin organizational complexity between the two major IBD subtypes in the pediatric age. The same analysis was performed to assess differences in the intestinal cell chromatin complexity between either of the IBD phenotypes and the control subjects. A comparison was performed on seven different intestinal segments (terminal ileum, cecum, ascending, transversal, descending and sigmoid colon and rectum). The differences in the FDs of the investigated nuclei are shown in Figure 4 and Table 4. Figure 4 shows the mean ranks according to the nonparametric Kruskal–Wallis H test, where the mean rank is the arithmetic

average of the positions in the sorted FD list for a total of 780 analyzed epithelial cell nuclei. The blue lines show the statistically significant mean rank differences. The children with UC had a significantly higher FD of the cell nuclei chromatin texture than the controls in all colonic segments except for the rectum ($p \leq 0.035$). Similar differences were revealed between the UC and CD children. Specifically, the UC patients had significantly higher FDs in comparison with the CD patients in every colon part except for the transversal colon ($p \leq 0.010$). On the other hand, the children with Crohn's disease had FDs that were statistically different from those of the controls only in the ileocecal valve and rectum ($p = 0.005$, $p = 0.014$; respectively), with lower median FD values in the CD patients. Interestingly, the terminal ileum of the CD patients, which is one of the most frequent localizations affected by the disease, had a statistically different nuclear FD only when compared with that of the UC patients.

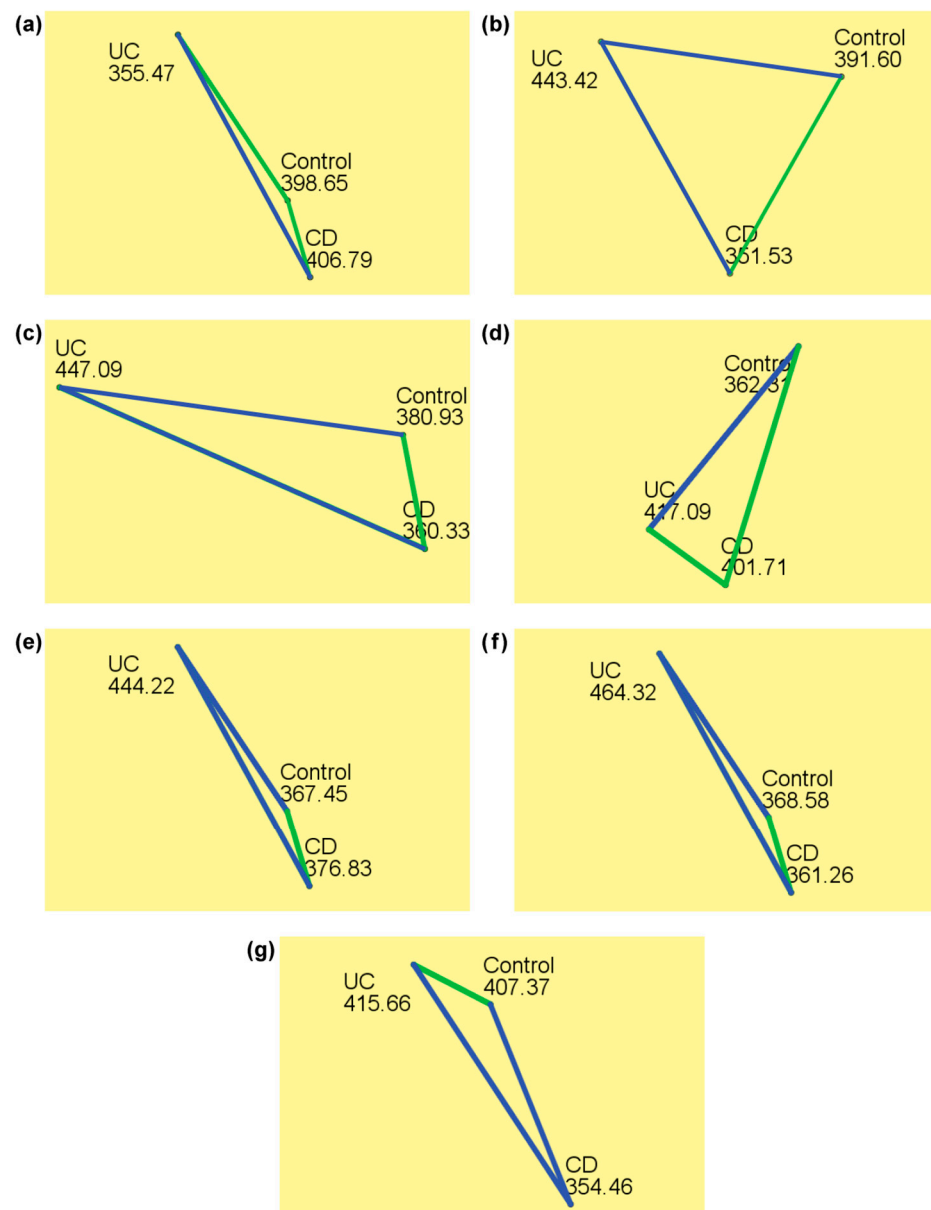**Figure 4.** Fractal dimension mean rank comparison between CD, UC, and control group, for 7 different intestinal segments: (**a**) terminal ileum, (**b**) cecum, (**c**) ascending colon, (**d**) transversal colon, (**e**) descending colon, (**f**) sigmoid colon, (**g**) rectum.

Table 4. Fractal dimension comparison between CD, UC, and control group.

Intestinal Segment	Fractal Dimension (FD)			Statistical Signif. (*p* Values)
	Crohn's Disease (CD)	Ulcerative Colitis (UC)	Control Group	
S1	1.728(1.586–1.831)	1.722 (1.593–1.802)	1.728 (1.531–1.819)	**CD–UC (0.042)**
				CD–Control (1.000)
				UC–Control (0.107)
S2	1.732 (1.523–1.842)	1.755 (1.559–1.834)	1.741 (1.599–1.818)	**CD–UC (<0.0001)**
				CD–Control (0.097)
				UC–Control (0.035)
S3	1.732 (1.529–1.829)	1.752 (1.135–1.840)	1.736 (1.547–1.835)	**CD–UC (<0.0001)**
				CD–Control (0.814)
				UC–Control (0.004)
S4	1.736 (1.566–1.831)	1.738 (1.048–1.843)	1.728 (1.538–1.812)	CD–UC (1.000)
				CD–Control (0.106)
				UC–Control (0.023)
S5	1.734 (1.593–1.816)	1.747 (1.118–1.948)	1.734 (1.555–1.810)	**CD–UC (0.004)**
				CD–Control (1.000)
				UC–Control (0.001)
S6	1.722 (1.521–1.940)	1.749 (1.601–1.947)	1.727 (1.585–1.826)	**CD–UC (<0.0001)**
				CD–Control (1.000)
				UC–Control (<0.0001)
S7	1.719 (1.524–1.944)	1.733 (1.511–1.824)	1.730 (1.536–1.818)	**CD–UC (0.010)**
				CD–Control (0.014)
				UC–Control (1.000)
S8	1.731 (1.617–1.788)		1.749 (1.605–1.834)	**CD–Control (0.005)**

The results are presented as median (range). Segment notation: S1—terminal ileum; S2—cecum; S3—ascending colon; S4—transversal colon; S5—descending colon; S6—sigmoid colon; S7—rectum; S8—ileocecal valve.

3.4. Lacunarity

The size and spatial distribution of the gaps in the cell nuclei textures, their spatial diversity, and the level of the image deviation from the rotational and translational invariance was measured by determining the texture lacunarity. Lacunarity analysis revealed additional significant differences between the Crohn's disease and ulcerative colitis ($p \leq 0.001$), as well as between the ulcerative colitis and the control ($p \leq 0.002$) (Figure 5, Table 5). In Figure 5, the blue lines show the statistically significant mean rank differences for lacunarity. A statistically significant difference was present throughout the colon with the exception of the same segments as those in the FD comparison (the transversal part for the CD–UC and the rectum for the UC–control comparison). The difference in the terminal ileum nuclear lacunarity was not statistically significant among the compared groups. The colon enterocyte nuclear lacunarity was the lowest in the UC group.
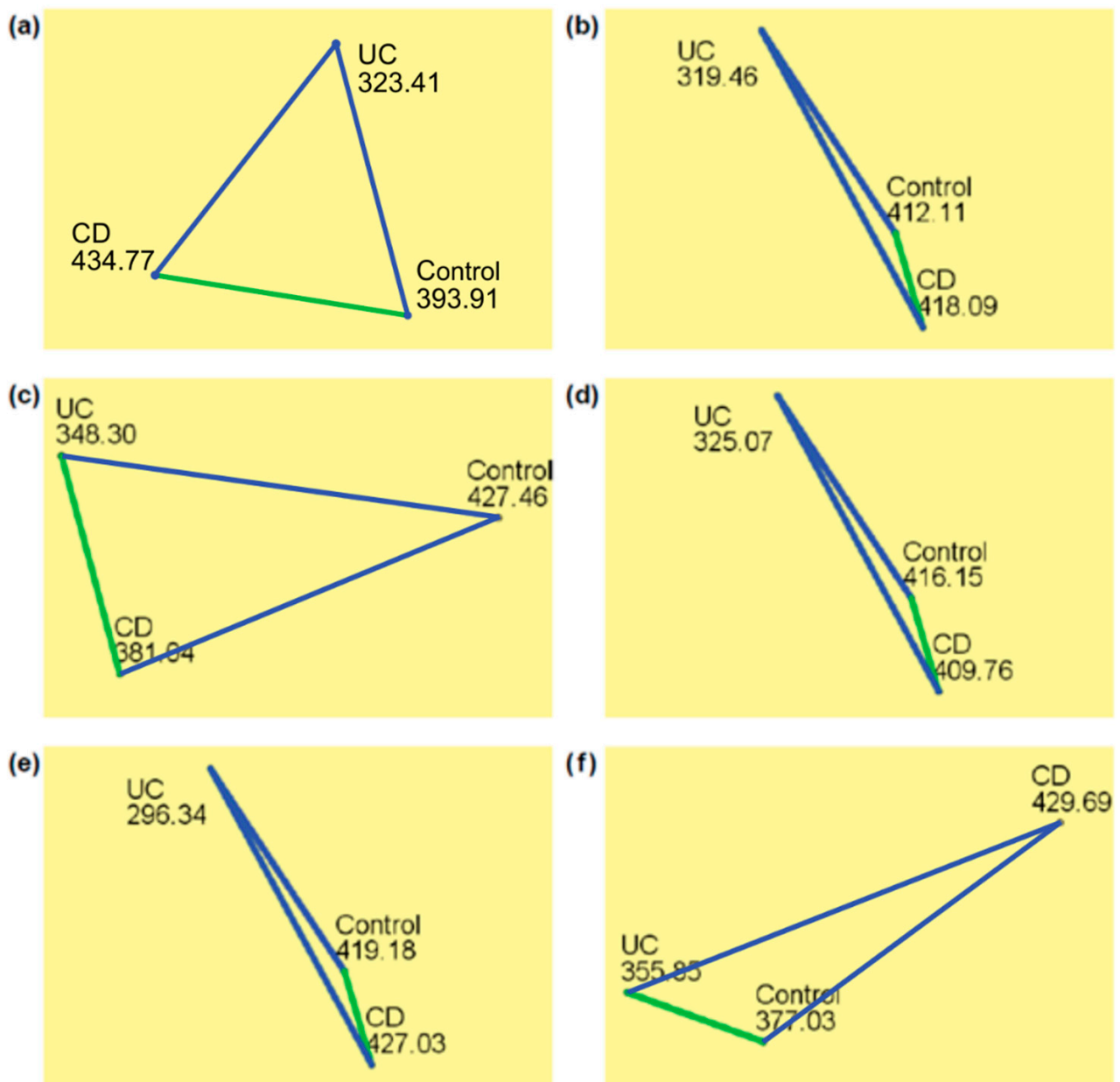
Figure 5. Lacunarity mean rank comparison between CD, UC, and control group for intestine segments: (**a**) cecum, (**b**) ascending colon, (**c**) transversal colon, (**d**) descending colon, (**e**) sigmoid colon, (**f**) rectum.

3.5. Intersegmental Comparison

Intersegmental comparisons of the fractal dimension and lacunarity of the cell nuclei texture are presented in Tables 6 and 7, respectively. One of the prominent results is a statistically lower rectal nuclear FD in comparison with the other segments (except for the sigmoid colon) in Crohn's disease patients. When the UC pediatric patients were considered, the nuclear FD proved highly useful in differentiating the colon (except for the rectum) and terminal ileum, the bowel part not affected by disease ($p < 0.002$). On the other hand, the FD across the control intestinal segments tended to be more uniform. As for the nuclear lacunarity, statistically significant differences were, with few exceptions, detected between the same segments as those in the case of the FD segment intercomparison.

Table 5. Lacunarity comparison between CD, UC, and control group.

Intestinal Segment	Lacunarity (Lac)			Statistical Signif. (p Values)
	Crohn's Disease (CD)	**Ulcerative Colitis (UC)**	**Control Group**	
S1	0.279 (0.172–0.430)	0.285 (0.209–0.455)	0.279 (0.197–0.517)	All groups (0.074)
S2	0.282 (0.163–0.470)	0.253 (0.167–0.422)	0.266 (0.178–0.407)	**CD–UC (<0.0001)** CD–Control (0.087) **UC–Control (0.002)**
S3	0.279 (0.174–0.460)	0.260 (0.175–0.404)	0.274 (0.192–0.481)	**CD–UC (<0.0001)** CD–Control (1.000) **UC–Control (<0.0001)**
S4	0.271 (0.184–0.442)	0.269 (0.181–0.554)	0.280 (0.198–0.482)	CD–UC (0.350) **CD–Control (0.039)** **UC–Control (<0.0001)**
S5	0.273 (0.273–0.430)	0.258 (0.037–0.365)	0.275 (0.191–0.475)	**CD–UC (<0.0001)** CD–Control (1.000) **UC–Control (<0.0001)**
S6	0.287 (0.042–0.510)	0.257 (0.038–0.378)	0.280 (0.190–0.467)	**CD–UC (<0.0001)** CD–Control (1.000) **UC–Control (<0.0001)**
S7	0.289 (0.040–0.480)	0.272 (0.183–0.450)	0.276 (0.182–0.504)	**CD–UC (0.001)** **CD–Control (0.015)** UC–Control (0.909)
S8	0.276 (0.221–0.396)		0.263 (0.199–0.418)	CD–Control (0.126)

The results are presented as median (range). Segment notation: S1—terminal ileum; S2—cecum; S3—ascending colon; S4—transversal colon; S5—descending colon; S6—sigmoid colon; S7—rectum; S8—ileocecal valve.

Table 6. Intersegmental comparison of nuclear fractal dimension.

Intestinal Segment	Fractal Dimension (FD)		
	Crohn's Disease (CD)	**Ulcerative Colitis (UC)**	**Control Group**
S1	1.728 (1.586–1.832)	1.723 (1.593–1.802)	1.728 (1.531–1.819)
S2	1.732 (1.524–1.843)	1.755 (1.559–1.834)	1.741 (1.600–1.819)
S3	1.732 (1.529–1.829)	1.752 (1.135–1.840)	1.736 (1.547–1.835)
S4	1.736 (1.567–1.831)	1.738 (1.048–1.843)	1.728 (1.538–1.812)
S5	1.734 (1.593–1.816)	1.747 (1.118–1.948)	1.734 (1.555–1.811)
S6	1.722 (1.521–1.940)	1.749 (1.601–1.948)	1.727 (1.585–1.826)
S7	1.719 (1.524–1.944)	1.733 (1.511–1.824)	1.729 (1.536–1.818)
Stat.sign. (p values)	**S7-S1, S7-S3, S7-S2, S7-S5, S7-S4** ($p < 0.025$)	**S1-S4, S1-S6, S1-S5, S1-S3, S1-S2** ($p < 0.002$) **S7-S6, S7-S5, S7-S3, S7-S2** ($p < 0.013$)	**S1-S2, S4-S2, S7-S2** ($p < 0.090$)

The results are presented as median (range). Segment notation: S1—terminal ileum; S2—cecum; S3—ascending colon; S4—transversal colon; S5—descending colon; S6—sigmoid colon; S7—rectum.

Table 7. Intersegmental comparison of cell nuclei texture lacunarity.

Intestinal Segment	Lacunarity (Lac)		
	Crohn's Disease (CD)	Ulcerative Colitis (UC)	Control Group
S1	0.279 (0.173–0.430)	0.285 (0.209–0.455)	0.279 (0.197–0.517)
S2	0.279 (0.163–0.470)	0.253 (0.167–0.422)	0.266 (0.178–0.407)
S3	0.279 (0.174–0.460)	0.259 (0.175–0.404)	0.274 (0.192–0.482)
S4	0.271 (0.184–0.442)	0.269 (0.181–0.555)	0.280 (0.198–0.482)
S5	0.273 (0.184–0.430)	0.258 (0.037–0.365)	0.275 (0.191–0.475)
S6	0.287 (.0420–0.510)	0.257 (0.038–0.378)	0.280 (0.190–0.467)
S7	0.289 (0.040–0.480)	0.272 (0.183–0.450)	0.276 (0.182–0.504)
Stat.sign. (*p* values)	**S2-S7, S3-S7, S4-S7, S5-S7** (*p* < 0.022)	**S2-S1, S3-S1, S4-S1, S6-S1** (*p* < 0.0001), **S2-S7, S3-S7, S6-S7** (*p* < 0.011) **S2-S4** (*p* < 0.025)	**S2-S1, S2-S4, S2-S6** (*p* < 0.040)

The results are presented as median (range). Segment notation: S1—terminal ileum; S2—cecum; S3—ascending colon; S4—transversal colon; S5—descending colon; S6—sigmoid colon; S7—rectum.

4. Discussion

Our results indicate that pediatric UC patients have a significantly increased nuclear structure and texture complexity, as measured with the FD, and decreased lacunarity compared to the children suffering from CD and the controls. This is a very important finding, given that the two IBD phenotypes are sometimes hard to distinguish. A significant difference was confirmed in most of the colon parts. In addition, the only intestinal segment with a significantly different nuclear fractal dimension and lacunarity between the CD patients and the controls was the rectum. However, the ileocecal valve of the CD children had a significantly decreased nuclear FD while the colon transversum had a statistically decreased lacunarity compared to the controls.

To the best of our knowledge, our study is the first which employed the calculations of the fractal dimension and lacunarity of intestinal cell nuclear chromatin in the IBD investigation. However, fractal analysis has previously been applied in the study of other intestinal pathologies. This methodology proved to be a promising aid in diagnosis [19,20] and therapy response [22,23] in intestinal carcinomas. Furthermore, a methodology based on fractal analysis was very accurate in abnormality detection in wireless capsule endoscopy (WCE) images [24]. Moreover, the differentiation between healthy and pathologic rectal mucosal vasculature can be accomplished with the fractal analysis of endoscopy images. The same analysis also proved to be useful for distinguishing between different rectal pathologies, e.g., colitis and vascular malformations [25]. Regarding IBD, fractals have been successful in ulcer identification from WCE images (caused by CD and UC, among other causes) [11] and bowel sounds detection in different intestinal pathologies, e.g., UC [30]. Finally, promising results were obtained in estimating the severity of intestinal fibrosis in a study conducted on histological slides stained with Masson's trichrome stain, which were derived from surgical specimens of CD patients. Specifically, an extracellular matrix (ECM) FD showed a significant correlation with a histological fibrosis score, and sections with different histological fibrosis scores had significantly different FDs. Thus, this investigation indicates that fibrosis progression in CD is more than a pure ECM accumulation and that it also includes structural ECM changes [29].

It should be mentioned, however, that our FD results, although they were consistent through the colon segments, still had some exceptions. Specifically, the nuclear chromatin FD of the transversal colon epithelial cells was similar in the CD and UC patients. In the CD patients, the median FD values were the highest in this segment. To better understand these intersegmental differences, we calculated regional scores that represented the histological disease activity for every segment. It appeared, in our group of patients with Crohn's disease, that in general its symptoms less often skipped the transversal segment than the other segments (fewer patients had GHAS < 4, indicating remission). Furthermore, in this

segment more Crohn's disease patients had moderate active disease (GHAS 8–10) than in the others. So, it appears that CD was more active in this part of colon. This finding strongly suggests the possibility that differences in the pathophysiological disease activity might have some influence on the FD results. However, this does not make fractal analysis less attractive for future diagnostic applications since in routine pathohistological diagnostics all seven different intestinal segments are being evaluated. Looking at the results of all the segments comparatively, it was confirmed without any doubt that the UC fractal dimension differed in a statistically significant way from the controls, as well as from the CD patient group.

UC is known as a disease exclusive to the colon. Therefore, as expected, in these patients the nuclear chromatin FDs in the terminal ileum were significantly lower than those of the rest of the colon (the rectum was an exception). This finding proves once more that the FD could serve as a very good discriminator of the UC-affected tissue.

In our study, the nuclear FD in the rectum was higher in the UC patients than in the other groups; however, in this case the difference was not sufficiently pronounced to provide a statistically significant result. Furthermore, in the UC patients, the nuclear FD in this segment was statistically different from those of the other colon segments (apart from the transversal colon). In general, the rectum is affected in a large majority of UC patients, but in the pediatric population, rectal sparing is not unusual. Histological rectal sparing absolute (normal rectum) or relative (less severe inflammation than in other colon parts) rectal sparing is present in 30% of pediatric patients [49]. Among our patients, 20% had absolute rectal sparing (Nancy 0 or 1), which probably mitigated the results. Therefore, rectal biopsies, although the easiest to obtain, will not be sufficient for UC diagnostics based on the FD, at least not in the pediatric population.

The rectum was also an interesting segment for the CD patients. This was the only segment in which the nuclear FDs of these patients statistically differed from those of the controls. The Crohn FDs generally tended to be lower than in the other groups, indicating decreased complexity of textures for those nuclei. However, the FD in the rectum was the lowest of all. In the intersegmental comparison among the CD patients, the rectal FD was statistically lower than in any other segment except for the sigmoid colon ($p < 0.025$). This makes the rectal nuclear chromatin FD a feature with a potential to be exploited in CD diagnosis.

One possible explanation for the increased FD in most of the colon parts in the UC patients might be an increase in euchromatin ("open" chromatin) versus the heterochromatin ratio. "Open" DNA is less densely packed, resulting in less intense staining and lighter color. In a study exploring the effects of the chromatin physical structure on the transcription of genes [31], both the mathematical predictions and the experimental evidence pointed to a link between the increased heterogeneity of the chromatin structure (increased fractal dimension) and the increased variation of the gene expression for most biological processes. The chromatin heterogeneity is considered a ubiquitous hallmark of cancer aggressiveness in tumor research [2,3,31,33]. However, changes in protein binding and chromatin structure have also been shown to play a role in gastrointestinal diseases and disorders, including the pathogenesis of inflammatory bowel disease (IBD) [44]. It might be challenging to recognize the chromatin structural changes on standard HE-dyed tissue slides [2]; this is of primary interest given that only such slides are available for diagnostic purposes. On the other hand, open chromatin can be distinguished by applying fractal analysis as it gives higher nuclear FD values [2,50]. The results of our study suggest that UC patients have a predominantly increased euchromatin/heterochromatin ratio in enterocyte nuclei compared to the CD patients and controls. One of the epigenetic mechanisms causing chromatin to be in a more open state is histone acetylation. In this process, the enhanced unwrapping ("opening") of DNA allows transcription [51]. On the other hand, the opposite process, histone deacetylation, enables histone and DNA binding, limiting access to DNA again [52]. It has been demonstrated that certain enzymes responsible for histone deacetylation—Sirtuin (SIRT)1, SIRT6 and histone deacetylase (HDAC)9—are

decreased in the inflamed colon tissue of UC patients compared to the same tissue of CD patients [53]. Decreased HDAC activity in UC patients might lead to enhanced histone acetylation and an increased amount of euchromatin, which in turn leads to a significantly higher FD compared to that of the CD patient group. Interestingly, HDAC inhibitors are seen as possible new drugs for UC considering their ability to decrease inflammation in colonic epithelial cells and dextran sulfate sodium-induced colitis [54].

According to the literature, the increase in chromatin lacunarity is often followed by the decrease in chromatin FD [33]. In this regard, our study is in line with the others. In colon tissue, nuclear lacunarity revealed the same statistically significant differences as the FD. However, lacunarity proved to be an even better colon CD discriminator than the FD since it was able to differentiate CD from the controls in more intestinal segments than the FD.

5. Conclusions

We conducted a detailed study of the fractal parameters corresponding to the altered textures of intestinal cell nuclei in pediatric patients as the prospective biomarkers for IBD. Although the changes in cell nuclei chromatin structure have been observed in cancers and have been observed to also coincide with the altered nuclei textures seen in histological samples [2,4,33], here, for the first time, a similar methodology was applied to IBD. The changes occurring in the protein binding and chromatin structure in gastrointestinal diseases motivated us to investigate the cell nuclei textures in IBD. We demonstrated that the intestinal nuclei of children suffering from UC compared with children with CD and a control group statistically increased the nuclear FD and decreased nuclear lacunarity. Furthermore, the current study provided evidence that in CD pediatric patients the rectum had a decreased nuclear FD and an increased lacunarity compared to the control group. Additionally, in the comparison between the segments, the rectum was different from almost all the other segments in terms of the nuclear FD and lacunarity. Therefore, the fractal analysis of intestinal cell nuclei was proven to have the potential to be an observer-independent histological tool for ulcerative colitis diagnosis. In addition, the rectum of CD pediatric patients also seems to be a very good candidate for the development of fractal-based diagnostics. Further studies are necessary to confirm our findings and to check on the consistency of the results in repeated trials. Furthermore, the inconsistency of the nuclear FD and lacunarity between the rectum and rest of the colon in children with CD is interesting, and it should be more thoroughly investigated. Our results pave the way for the development of computer-aided diagnosis systems that will assist in the clinical practice in gastroenterology.

Author Contributions: Conceptualization, A.Ž.I., S.R.d.L. and I.D.M.; methodology, A.Ž.I., S.R.d.L., I.D.M., R.J. and V.M.; software, A.Ž.I. and J.T.; validation, A.Ž.I. and I.D.M.; formal analysis, V.M., R.J., A.V., J.T. and B.M.; investigation, V.M., J.J., R.J. and A.V.; resources, I.D.M. and N.P.; data curation, V.M.; writing—original draft preparation, V.M. and I.D.M.; writing—review and editing, A.Ž.I. and S.R.d.L.; visualization, A.Ž.I. and V.M.; supervision, A.Ž.I. and S.R.d.L.; project administration, A.Ž.I. and S.R.d.L.; funding acquisition, S.R.d.L., I.D.M. and N.P. All authors have read and agreed to the published version of the manuscript.

Institutional Review Board Statement: The study was conducted in accordance with the Declaration of Helsinki.

Informed Consent Statement: Informed consent was obtained from all subjects involved in the study.

Data Availability Statement: Fractal analysis and statistical data presented in this study are available on request from the corresponding author. Patient-related data cannot be shared due to ethical, legal, and privacy issues.

References

1. Husain, A.; Nanda, M.N.; Chowdary, M.S.; Sajid, M. Fractals: An eclectic survey, part II. *Fractal Fract.* **2022**, *6*, 379. [CrossRef]
2. de Mattos, A.C.; Florindo, J.B.; Adam, R.L.; Lorand-Metze, I.; Metze, K. The fractal dimension suggests two chromatin configurations in small cell neuroendocrine lung cancer and is an independent unfavorable prognostic factor for overall survival. *Microsc. Microanal.* **2022**, *28*, 522–526. [CrossRef]
3. Karri, S.; Aviel-Ronen, S.; Firer, M.A. Fractal and textural imaging identify new subgroups of patients with colorectal cancer based on biophysical properties of the cancer cells. *Pathol. Res. Pract.* **2022**, *238*, 154040. [CrossRef]
4. Dinčić, M.; Todorović, J.; Nešović-Ostojić, J.; Kovačević, S.; Dunđerović, D.; Lopičić, S.; Spasić, S.; Radojević-Škodrić, S.; Stanisavljević, D.; Ilić, A.Ž. The fractal and GLCM textural parameters of chromatin may be potential biomarkers of papillary thyroid carcinoma in Hashimoto's thyroiditis specimens. *Microsc. Microanal.* **2020**, *26*, 717–730. [CrossRef]
5. Dinčić, M.; Popović, T.B.; Kojadinović, M.; Trbovich, A.M.; Ilić, A.Ž. Morphological, fractal, and textural features for the blood cell classification: The case of acute myeloid leukemia. *Eur. Biophys. J.* **2021**, *50*, 1111–1127. [CrossRef] [PubMed]
6. Einstein, A.J.; Wu, H.-S.; Gil, J. Self-affinity and lacunarity of chromatin texture in benign and malignant breast epithelial cell nuclei. *Phys. Rev. Lett.* **1998**, *80*, 397–400. [CrossRef]
7. Ioelovich, M. Fractal dimensions of cell wall in growing cotton fibers. *Fractal Fract.* **2020**, *4*, 6. [CrossRef]
8. Arsac, L.M.; Weissland, T. Multifractality in the movement system when adapting to arm cranking in wheelchair athletes, able-bodied athletes, and untrained people. *Fractal Fract.* **2022**, *6*, 176. [CrossRef]
9. Smith, T.G., Jr.; Lange, G.D.; Marks, W.B. Fractal methods and results in cellular morphology—Dimensions, lacunarity and multifractals. *J. Neurosci. Methods* **1996**, *69*, 123–136. [CrossRef] [PubMed]
10. Tél, T. Fractals, multifractals, and thermodynamics: An introductory review. *Z. Naturforschung A* **1988**, *43*, 1154–1174. [CrossRef]
11. Charisis, V.S.; Hadjileontiadis, L.J.; Liatsos, C.N.; Mavrogiannis, C.C.; Sergiadis, G.D. Capsule endoscopy image analysis using texture information from various colour models. *Comput. Methods Programs Biomed.* **2012**, *107*, 61–74. [CrossRef]
12. Oprić, D.; Stankovich, A.D.; Nenadović, A.; Kovačević, S.; Obradović, D.D.; De Luka, S.; Nešović-Ostojić, J.; Milašin, J.; Ilić, A.Ž.; Trbovich, A.M. Fractal analysis tools for early assessment of liver inflammation induced by chronic consumption of linseed, palm and sunflower oils. *Biomed. Sign. Process. Control* **2020**, *61*, 101959. [CrossRef]
13. Stojić, D.; Radošević, D.; Rajković, N.; Marić, D.L.; Milošević, N.T. Classification by morphology of multipolar neurons of the human principal olivary nucleus. *Neurosci. Res.* **2021**, *170*, 66–75. [CrossRef]
14. Lyu, X.; Jajal, P.; Tahir, M.Z.; Zhang, S. Fractal dimension of retinal vasculature as an image quality metric for automated fundus image analysis systems. *Sci. Rep.* **2022**, *12*, 11868. [CrossRef]
15. Freeborn, T.J.; Fu, B. Fatigue-induced Cole electrical impedance model changes of biceps tissue bioimpedance. *Fractal Fract.* **2018**, *2*, 27. [CrossRef]
16. Gladun, K.V. Higuchi fractal dimension as a method for assessing response to sound stimuli in patients with diffuse axonal brain injury. *Sovrem. Tehnologii Med.* **2020**, *12*, 63. [CrossRef]
17. Naik, G.R.; Arjunan, S.; Kumar, D. Applications of ICA and fractal dimension in sEMG signal processing for subtle movement analysis: A review. *Australas. Phys. Eng. Sci. Med.* **2011**, *34*, 179–193. [CrossRef] [PubMed]
18. Stylianou, O.; Kaposzta, Z.; Czoch, A.; Stefanovski, L.; Yabluchanskiy, A.; Racz, F.S.; Ritter, P.; Eke, A.; Mukli, P. Scale-free functional brain networks exhibit increased connectivity, are more integrated and less segregated in patients with Parkinson's disease following dopaminergic treatment. *Fractal Fract.* **2022**, *6*, 737. [CrossRef]
19. Goh, V.; Sanghera, B.; Wellsted, D.M.; Sundin, J.; Halligan, S. Assessment of the spatial pattern of colorectal tumour perfusion estimated at perfusion CT using two-dimensional fractal analysis. *Eur. Radiol.* **2009**, *19*, 1358–1365. [CrossRef]
20. Streba, L.; Forţofoiu, M.C.; Popa, C.; Ciobanu, D.; Gruia, C.L.; Mogoantă, S.; Streba, C.T. A pilot study on the role of fractal analysis in the microscopic evaluation of colorectal cancers. *Rom. J. Morphol. Embryol.* **2015**, *56*, 191–196. [PubMed]
21. Watanabe, H.; Hayano, K.; Ohira, G.; Imanishi, S.; Hanaoka, T.; Hirata, A.; Kano, M.; Matsubara, H. Quantification of structural heterogeneity using fractal analysis of contrast-enhanced CT image to predict survival in gastric cancer patients. *Dig Dis Sci.* **2021**, *66*, 2069–2074. [CrossRef] [PubMed]
22. Dzik-Jurasz, A.; Walker-Samuel, S.; Leach, M.O.; Brown, G.; Padhani, A.; George, M.; Collins, D.J. Fractal parameters derived from analysis of DCE-MRI data correlates with response to therapy in rectal carcinoma. In Proceedings of the International Society for Magnetic Resonance in Medicine 11, ISMRM 12th Scientific Meeting, Kyoto, Japan, 15–21 May 2004; p. 2503.
23. Tochigi, T.; Kamran, S.C.; Parakh, A.; Noda, Y.; Ganeshan, B.; Blaszkowsky, L.S.; Ryan, D.P.; Allen, J.N.; Berger, D.L.; Wo, J.Y.; et al. Response prediction of neoadjuvant chemoradiation therapy in locally advanced rectal cancer using CT-based fractal dimension analysis. *Eur. Radiol.* **2022**, *32*, 2426–2436. [CrossRef]
24. Jain, S.; Seal, A.; Ojha, A.; Krejcar, O.; Bureš, J.; Tacheci, I.; Yazidi, A. Detection of abnormality in wireless capsule endoscopy images using fractal features. *Comput. Biol. Med.* **2020**, *127*, 104094. [CrossRef] [PubMed]

25. Gryglewski, A.; Henry, B.M.; Mrozek, M.; Żelawski, M.; Piech, K.; Tomaszewski, K.A. Sensitivity and specificity of fractal analysis to distinguish between healthy and pathologic rectal mucosa microvasculature seen during colonoscopy. *Surg. Laparosc. Endosc. Percutan. Tech.* **2016**, *26*, 358–363. [CrossRef] [PubMed]

26. Paramasivam, A.; Kamalanand, K.; Emmanuel, C.; Mahadevan, B.; Sundravadivelu, K.; Raman, J.; Jawahar, P.M. Influence of electrode surface area on the fractal dimensions of electrogastrograms and fractal analysis of normal and abnormal digestion process. In Proceedings of the 2018 International Conference on Recent Trends in Electrical, Control and Communication (RTECC 2018), Malaysia, Malaysia, 20–22 March 2018; pp. 245–250. [CrossRef]

27. Yan, R.; Guo, X. Nonlinear fractal dynamics of human colonic pressure activity based upon the box-counting method. *Comput. Methods Biomech. Biomed. Eng.* **2013**, *16*, 660–668. [CrossRef]

28. Dimoulas, C.; Kalliris, G.; Papanikolaou, G.; Kalampakas, A. Long-term signal detection, segmentation and summarization using wavelets and fractal dimension: A bioacoustics application in gastrointestinal-motility monitoring. *Comput. Biol. Med.* **2007**, *37*, 438–462. [CrossRef]

29. Weber, M.C.; Schmidt, K.; Buck, A.; Kasajima, A.; Becker, S.; Wilhelm, D.; Friess, H.; Neumann, P.A. P067 Fractal analysis of extracellular matrix as a new histological method for observer-independent quantification of intestinal fibrosis in Crohn's disease. *J. Crohn's Colitis* **2023**, *17* (Suppl. 1), i234. [CrossRef]

30. Hadjileontiadis, L.J.; Rekanos, I.T. Detection of explosive lung and bowel sounds by means of fractal dimension. *IEEE Signal Process. Lett.* **2003**, *10*, 311–314. [CrossRef]

31. Almassalha, L.; Tiwari, A.; Ruhoff, P.; Stypula-Cyrus, Y.; Cherkezyan, L.; Matsuda, H.; Dela Cruz, M.A.; Chandler, J.E.; White, C.; Maneval, C.; et al. The global relationship between chromatin physical topology, fractal structure, and gene expression. *Sci. Rep.* **2017**, *7*, 41061. [CrossRef]

32. Bancaud, A.; Lavelle, C.; Huet, S.; Ellenberg, J. A fractal model for nuclear organization: Current evidence and biological implications. *Nucl. Acids Res.* **2012**, *40*, 8783–8792. [CrossRef]

33. Metze, K.; Adam, R.; Florindo, J.B. The fractal dimension of chromatin—A potential molecular marker for carcinogenesis, tumor progression and prognosis. *Expert Rev. Mol. Diagn.* **2019**, *19*, 299–312. [CrossRef] [PubMed]

34. Vesković, M.; Labudović-Borović, M.; Zaletel, I.; Rakočević, J.; Mladenović, D.; Jorgačević, B.; Vučević, D.; Radosavljević, T. The effects of betaine on the nuclear fractal dimension, chromatin texture, and proliferative activity in hepatocytes in mouse model of nonalcoholic fatty liver disease. *Microsc. Microanal.* **2018**, *24*, 132–138. [CrossRef]

35. Ray, G.; Longworth, M.S. Epigenetics, DNA organization, and inflammatory bowel disease. *Inflamm. Bowel Dis.* **2019**, *25*, 235–247. [CrossRef]

36. Fedor, I.; Zold, E.; Barta, Z. Temporal relationship of extraintestinal manifestations in inflammatory bowel disease. *J. Clin. Med.* **2021**, *10*, 5984. [CrossRef] [PubMed]

37. Gajendran, M.; Loganathan, P.; Jimenez, G.; Catinella, A.P.; Ng, N.; Umapathy, C.; Ziade, N.; Hashash, J.G. A comprehensive review and update on ulcerative colitis. *Dis. Mon.* **2019**, *65*, 100851. [CrossRef] [PubMed]

38. Sathiyasekaran, M.; Shivbalan, S. Crohn's disease. *Indian J. Pediatr.* **2006**, *73*, 723–729. [CrossRef]

39. Fuller, M.K. Pediatric inflammatory bowel disease: Special considerations. *Surg. Clin. N. Am.* **2019**, *99*, 1177–1183. [CrossRef]

40. De Roche, T.C.; Xiao, S.Y.; Liu, X. Histological evaluation in ulcerative colitis. *Gastroenterol. Rep.* **2014**, *2*, 178–192. [CrossRef]

41. Torres, J.; Bonovas, S.; Doherty, G.; Kucharzik, T.; Gisbert, J.P.; Raine, T.; Adamina, M.; Armuzzi, A.; Bachmann, O.; Bager, P.; et al. ECCO Working Group. ECCO Guidelines on Therapeutics in Crohn's Disease: Medical Treatment. *J. Crohn's Colitis* **2020**, *14*, 4–22. [CrossRef]

42. Szymanska, E.; Wierzbicka, A.; Dadalski, M.; Kierkus, J. Fecal zonulin as a noninvasive biomarker of intestinal permeability in pediatric patients with inflammatory bowel diseases—Correlation with disease activity and fecal calprotectin. *J. Clin. Med.* **2021**, *10*, 3905. [CrossRef]

43. Ordog, T.; Syed, S.; Hayashi, Y.; Asuzu, D.T. Epigenetics and chromatin dynamics: A review and a paradigm for functional disorders. *Neurogastroenterol. Motil.* **2012**, *24*, 1054–1068. [CrossRef]

44. Ansari, I.; Raddatz, G.; Gutekunst, J.; Ridnik, M.; Cohen, D.; Abu-Remaileh, M.; Tuganbaev, T.; Shapiro, H.; Pikarsky, E.; Elinav, E.; et al. The microbiota programs DNA methylation to control intestinal homeostasis and inflammation. *Nat. Microbiol.* **2020**, *5*, 610–619. [CrossRef] [PubMed]

45. Ruifrok, A.C.; Johnston, D.A. Quantification of histochemical staining by color deconvolution. *Anal. Quant. Cytol. Histol.* **2001**, *23*, 291–299.

46. Landini, G.; Martinelli, G.; Piccinini, F. Colour deconvolution: Stain unmixing in histological imaging. *Bioinformatics* **2021**, *37*, 1485–1487. [CrossRef] [PubMed]

47. Singh, T.R.; Roy, S.; Singh, O.I.; Sinam, T.; Singh, K.M. A new local adaptive thresholding technique in binarization. *IJCSI Int. J. Comp. Sci.* **2011**, *8*, 271–277. [CrossRef]

48. Karperien, A.L.; Jelinek, H.F. Box-counting fractal analysis: A primer for the clinician. In *The Fractal Geometry of the Brain*; Di Ieva, A., Ed.; Springer: New York, NY, USA, 2016; pp. 91–108. [CrossRef]

49. Glickman, J.N.; Bousvaros, A.; Farraye, F.A.; Zholudev, A.; Friedman, S.; Wang, H.H.; Leichtner, A.M.; Odze, R.D. Pediatric patients with untreated ulcerative colitis may present initially with unusual morphologic findings. *Am. J. Surg. Pathol.* **2004**, *28*, 190–197. [CrossRef]

50. Bancaud, A.; Huet, S.; Daigle, N.; Mozziconacci, J.; Beaudouin, J.; Ellenberg, J. Molecular crowding affects diffusion and binding of nuclear proteins in heterochromatin and reveals the fractal organization of chromatin. *EMBO J.* **2009**, *28*, 3785–3798. [CrossRef] [PubMed]

51. Mobley, A.S. Chapter 4—Induced pluripotent stem cells. In *Neural Stem Cells and Adult Neurogenesi*; Mobley, A.S., Ed.; Academic Press: London, UK, 2019; ISBN 9780128110140. [CrossRef]

52. Chessum, N.; Jones, K.; Pasqua, E.; Tucker, M. Recent advances in cancer therapeutics. *Prog. Med. Chem.* **2015**, *54*, 1–63. [CrossRef]

53. De Bruyn, J.; Wichers, C.; Radstake, T.; Broen, J.; D'Haens, G. Histone deacetylases in inflammatory mucosa distinguish Crohn's disease from ulcerative colitis. *J. Crohn's Colitis* **2015**, *9* (Suppl. 1), S87–S88. [CrossRef]

54. Blanchard, F.; Chipoy, C. Histone deacetylase inhibitors: New drugs for the treatment of inflammatory diseases? *Drug. Discov. Today* **2005**, *10*, 197–204. [CrossRef] [PubMed]

Structural Characterization of *Toxoplasma gondii* Brain Cysts in a Model of Reactivated Toxoplasmosis Using Computational Image Analysis

Neda Bauman [1], Jelena Srbljanović [1], Ivana Čolović Čalovski [2], Olivera Lijeskić [1], Vladimir Ćirković [1], Jelena Trajković [3,4], Branko Bobić [1], Andjelija Ž. Ilić [3,*] and Tijana Štajner [1,*]

1   National Reference Laboratory for Toxoplasmosis, Group for Microbiology and Parasitology, Centre of Excellence for Food- and Vector-Borne Zoonoses, Institute for Medical Research, National Institute of Republic of Serbia, University of Belgrade, 11000 Belgrade, Serbia; neda.bauman@imi.bg.ac.rs (N.B.); jelena.srbljanovic@imi.bg.ac.rs (J.S.); olivera.lijeskic@imi.bg.ac.rs (O.L.); vladimir.cirkovic@imi.bg.ac.rs (V.Ć.); bobicb@imi.bg.ac.rs (B.B.)
2   Department of Parasitology and Mycology, Institute of Microbiology and Immunology, Faculty of Medicine, University of Belgrade, 11000 Belgrade, Serbia; ivana.colovic-calovski@med.bg.ac.rs
3   Institute of Physics Belgrade, University of Belgrade, Pregrevica 118, 11080 Belgrade, Serbia; jelena.trajkovic@ipb.ac.rs
4   Faculty of Physics, University of Belgrade, 11000 Belgrade, Serbia
*   Correspondence: andjelijailic@ieee.org (A.Ž.I.); tijana.stajner@imi.bg.ac.rs (T.Š.); Tel.: +381-113713164 (A.Ž.I.); +381-112685788 (T.Š.)

Abstract: *Toxoplasma gondii* is an obligate intracellular parasite existing in three infectious life stages—tachyzoites, bradyzoites, and sporozoites. Rupture of tissue cysts and re-conversion of bradyzoites to tachyzoites leads to reactivated toxoplasmosis (RT) in an immunocompromised host. The aim of this study was to apply ImageJ software for analysis of *T. gondii* brain cysts obtained from a newly established in vivo model of RT. Mice chronically infected with *T. gondii* (BGD1 and BGD26 strains) were treated with cyclophosphamide and hydrocortisone (experimental group—EG) or left untreated as infection controls (ICs). RT in mice was confirmed by qPCR (PCR+); mice remaining chronically infected were PCR−. A total of 90 images of cysts were analyzed for fractal dimension (*FD*), lacunarity (*L*), diameter (*D*), circularity (*C*), and packing density (*PD*). Circularity was significantly higher in PCR+ compared to IC mice ($p < 0.05$ for BGD1, $p < 0.001$ for the BGD26 strain). A significant negative correlation between *D* and *PD* was observed only in IC for the BGD1 strain ($\varrho = -0.384$, $p = 0.048$), while fractal parameters were stable. Significantly higher *D*, *C*, and *PD* and lower lacunarity, *L*, were noticed in the BGD1 compared to the more aggressive BGD26 strain. In conclusion, these results demonstrate the complexity of structural alterations of *T. gondii* cysts in an immunocompromised host and emphasize the application potential of ImageJ in the experimental models of toxoplasmosis.

Keywords: *Toxoplasma gondii*; reactivated toxoplasmosis; brain cysts; computational image analysis

1. Introduction

Toxoplasma gondii is an obligate intracellular parasite with a worldwide distribution. It exists in three infectious life stages—rapidly dividing tachyzoites, slowly growing bradyzoites, and sporozoites. Conversion of tachyzoites into encysted bradyzoites is a particular feature of the complex life cycle of this parasite but essential for its persistence in the host [1]. However, rupture of tissue cysts with an egress of bradyzoites and their re-conversion to proliferating tachyzoites results in life-threatening reactivated toxoplasmosis (RT), which is an expected outcome of impaired immune control of the chronic infection [2].

Although *T. gondii* cyst stage has been extensively studied for decades, there are still controversies regarding mechanisms responsible for its latency in an immunocompe-

tent host, as well as events preceding reactivation in the setting of a weakened immune system [3]. Furthermore, despite some existing drugs (used for the treatment of other diseases) [4,5] and novel compounds [6] with documented efficacy on *T. gondii* cyst stage in murine models of chronic toxoplasmosis, there is still a small arsenal of registered drugs available for the treatment of toxoplasmosis, and none of them are able to eradicate the parasite from an infected host [7,8]. In addition, the analysis of chemotherapy results in animal models often requires the application of a complex and heterogeneous methodology and needs to be improved in the future [9].

Computational image analysis is now increasingly used in biomedical research, offering a precise quantitative approach in describing complex objects [10–13]. Fractal-based image analysis methods can be used, solely or in combination with other methods such as the gray-level co-occurrence matrix (GLCM) analysis [14,15], discrete wavelet transform (DWT) [14], and the finite-element method (FEM) [16] to point out the structural alterations, i.e., different degrees of irregularity in the structure of signals and images of human biological samples obtained from a wide range of clinical conditions, predominantly carcinoma and chronic noncommunicable diseases. Depending on the studied problem, certain parameters were selected to conduct the analyses. In [14], fractal dimension was used alongside GLCM and DWT features in the classification of cells exposed to a hyperosmotic environment versus controls. In [16], fractal dimension combined with FEM was employed to assess the mechanical properties of liver tissue affected by fibrosis. Fractal lacunarity has been used in [15,17]. Multifractal features (generalized dimensions, singularity spectrum) have provided excellent classification accuracy in [18–20].

In microbiology, computational image analysis has also been proposed as a promising tool that could facilitate both research and diagnostics [21–23]. However, its application potential for in-depth studies focused on *T. gondii* is still limited. In fact, we were the first to introduce the use of freely available ImageJ software v. 1.52i (NIH, Bethesda, MD, USA), along with its fractal analysis plugin [24], as an affordable and widely accessible methodology for detailed observational analysis of *T. gondii* brain cysts [25]. For example, such a novel yet mathematically objective study approach on *T. gondii* cysts in murine models of toxoplasmosis would enable standardized analysis and interpretation of experimental results, and eventually facilitate drug development process.

Even though a variety of animal models of toxoplasmosis have been developed so far, primarily for chemotherapy studies [9], only few have been focused on RT. Indeed, development of an up-to-date murine model of RT that would allow for evaluation of drug efficacy in a rapidly rising population of immunocompromised patients, especially those undergoing organ or tissue transplantation [26], has become a research priority. Most in vivo models of RT established so far included only the high-dosage corticosteroid treatment [9,27]. Corticosteroids are indeed the first-line drugs used for the treatment of graft versus host disease (GVHD) in transplant recipients. In addition, cyclophosphamide is one of the widely used immunosuppressants in transplantation-related protocols [28] and has also been used in some experimental models of RT [29,30]. Combining these two drugs would enable closer simulation of one of the most common iatrogenic immunosuppression protocols in human transplantation medicine.

The aim of this study was to apply computer image analysis on high-resolution images of *T. gondii* brain cysts obtained from a newly established in vivo model of RT, using *T. gondii* strains isolated from human biological samples for infection and immunosuppressant drugs commonly administered in transplant recipients.

2. Materials and Methods

2.1. Mice

For in vivo experimental models of RT, Swiss Webster female mice (Medical Military Academy Animal Research Facility, Belgrade, Serbia) weighing 18–20 g at the beginning of the experiment were used. Mice were housed five per cage at the Institute for Medical

Research Animal Research Facility, Belgrade, Serbia, and offered regular mouse feed and drinking water ad libitum.

2.2. Parasites

Two *T. gondii* strains of human origin genotyped as type II *T. gondii* strains (referred to as BGD1 and BGD26) were included in the study. These strains were previously isolated from human biological materials and thereafter regularly maintained in Swiss Webster mice in the National Reference Laboratory (NRL) for Toxoplasmosis, Belgrade, Serbia [31,32]. Tachyzoites used for experimental infection were obtained based on a previously established protocol [33]. Briefly, tachyzoites of the BGD1 and BGD26 strains were harvested from peritoneal exudates of Swiss Webster mice previously inoculated intraperitoneally (i.p.) with cysts, then propagated in Vero cells (ATCC No. CCL-81) and harvested before the inoculation. To determine the precise number of parasites needed for infection, 20 μL of suspension was stained with Trypan blue and counted using a Burker-Turk hemocytometer.

2.3. Experimental Design

The mice were inoculated i.p. with tachyzoites of the BGD1 (10^4, $n = 102$ mice) and BGD26 (10^2, $n = 50$ mice) strains. The doses of tachyzoites for each strain were determined based on the results of the survival rate in mice infected with 10^2 and 10^4 tachyzoites in our preliminary experiments. Signs of clinical aggravation (ruffled fur, apathy, loss of appetite/anorexia, etc.) and survival were monitored daily during the 42-day period needed for complete establishment of chronic infection. On day 21, *T. gondii* infection was confirmed in the surviving mice by the detection of specific IgG antibodies from serum using in-house high-sensitivity direct agglutination assay (HSDA), using approximately 20 μL of peripheral blood, drawn from the saphenous vein [34]. Seronegative mice were eliminated from the study.

To establish the in vivo model of RT that would respond to real-life challenges, Swiss Webster mice infected six weeks before with tachyzoites of BGD1 *T. gondii* strain were assigned to treatment with cyclophosphamide (150 mg/kg per dose in three doses every third day) and hydrocortisone (50 mg/kg per dose 3 times a week) (experimental group—EG) over a period of 4 weeks or left untreated as infection controls (ICs). Hence, immunosuppression in treated mice was achieved by using both drugs during the first two weeks and maintained only by the corticosteroid drug for the last two weeks of treatment/experiment. After the establishment of the model with BGD1, the same protocol was applied to the BGD26 strain, which was used to compare the results obtained with the main (BGD1) strain. The immunosuppressive drug regimen used in this study was based on the literature data [27,35] and results of our preliminary experiments, which showed a fast drop in leukocyte count in peripheral blood of treated animals (as low as 0.66×10^6/mL peripheral blood (SD = 0.357) at day 10 of the treatment) and a mortality rate (30%) not exceeding the percentage reported for the usual corticosteroid regimen used in previous model of RT [27].

Peripheral blood (50 μL) for qPCR analysis was drawn from 1–5 mice (depending on survival) per strain at day 42 (IC mice) and at 6 more time points (IC and EG mice), defined within the treatment timeline (day 46, 49, 52, 58, 65, and 70 post-infection), if applicable (if there were surviving mice available at that particular time point). Upon collection of peripheral blood, mice were humanely sacrificed by cervical dislocation. Their brains were harvested, homogenized in 1 mL of saline solution using a syringe and a needle (21 gauge), and microscopically examined for the presence of *T. gondii* cysts.

RT in mice was diagnosed based on the detection of *T. gondii* 529-bp repetitive element in peripheral blood sample using qPCR [36]. Amplification was performed in a StepOnePlus Real-Time PCR System (Applied Biosystems, Foster City, CA, USA) using the following cycling conditions: 2 min at 50 °C, 10 min at 95 °C followed by 40 cycles of 15 s at 95 °C and 60 s at 60 °C. Apart from samples, the reaction mix-

ture contained Maxima Probe/ROX qPCR Master Mix (2×) (Thermofisher Scientific, Waltham, MA, USA), forward (5′-AGAGACACCGGAATGCGATCT) and reverse (5′-CCCTCTTCTCCACTCTTCAATTCT) primers (25 µM), TaqMan probe (5′-6FAM-ACGCTTT-CCTCGTGGTGATGGCG-TAMRA) (10 µM) (Invitrogen, Carlsbad, CA, USA), and nuclease-free water in a final volume of 20 µL. Samples were analyzed in duplicate. According to these results, treated mice were classified as *T. gondii*-reactivated (PCR+) or not (PCR−).

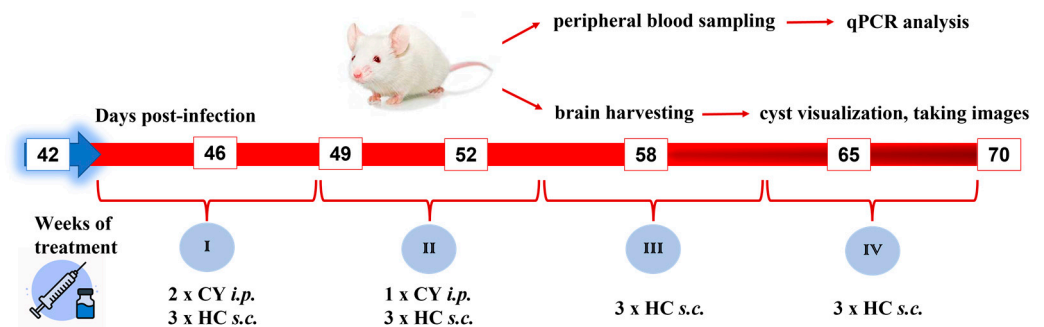The experimental design of the model is presented in Figure 1.

Figure 1. Model of RT—experimental design. Time points for IC (blue and red) and EG (red) are presented on the timeline. CY—cyclophosphamide; HC—hydrocortisone.

2.4. Image Acquisition

Computer image analysis was performed on images of *T. gondii* cysts obtained from established in vivo models. For cyst visualization, 25 µL of the brain suspension was placed on glass slides without fixation. The cysts were morphologically recognized using a phase-contrast microscope (Axioskop 2 Plus, Zeiss, Jena, Germany), under magnification of 1000× (oil immersion), and photographed by Zeiss Axio-CamMRc 5 in a live image window. The cyst diameter was measured using AxioVision Rel. 4.8.2 software. The images were saved as 2584 × 1936 px^2 TIFF files (image format 24 bit RGB). Several images of the same cyst were taken, and the best-focused one was selected for further analysis.

2.5. Image Analysis

All of the computer image analyses necessary for cyst characterization were performed using the ImageJ software package v. 1.52i (NIH, Bethesda, MD, USA), which is widely available, straightforward to apply, and amongst the tools of choice in the biomedical community. The acquired phase-contrast images appeared in shades of gray and were converted to 8-bit grayscale images prior to any analyses. Figure 2 shows several representative example cyst images, illustrating the initial appearance of bradyzoites within a cyst, as well as the transformations performed to prepare the original images for particle and fractal analysis. There are no obvious, to the human observer, differences in the visual appearance of bradyzoites between the two studied *T. gondii* strains; thus, only images for the BGD1 strain are shown. Examples are given for the IC and EG groups, for three time points. Contrast enhancements allowing 0.4% of saturated pixels and histogram equalization were carried out for all images, rendering high-contrast high-resolution images shown in the leftmost column of Figure 2.
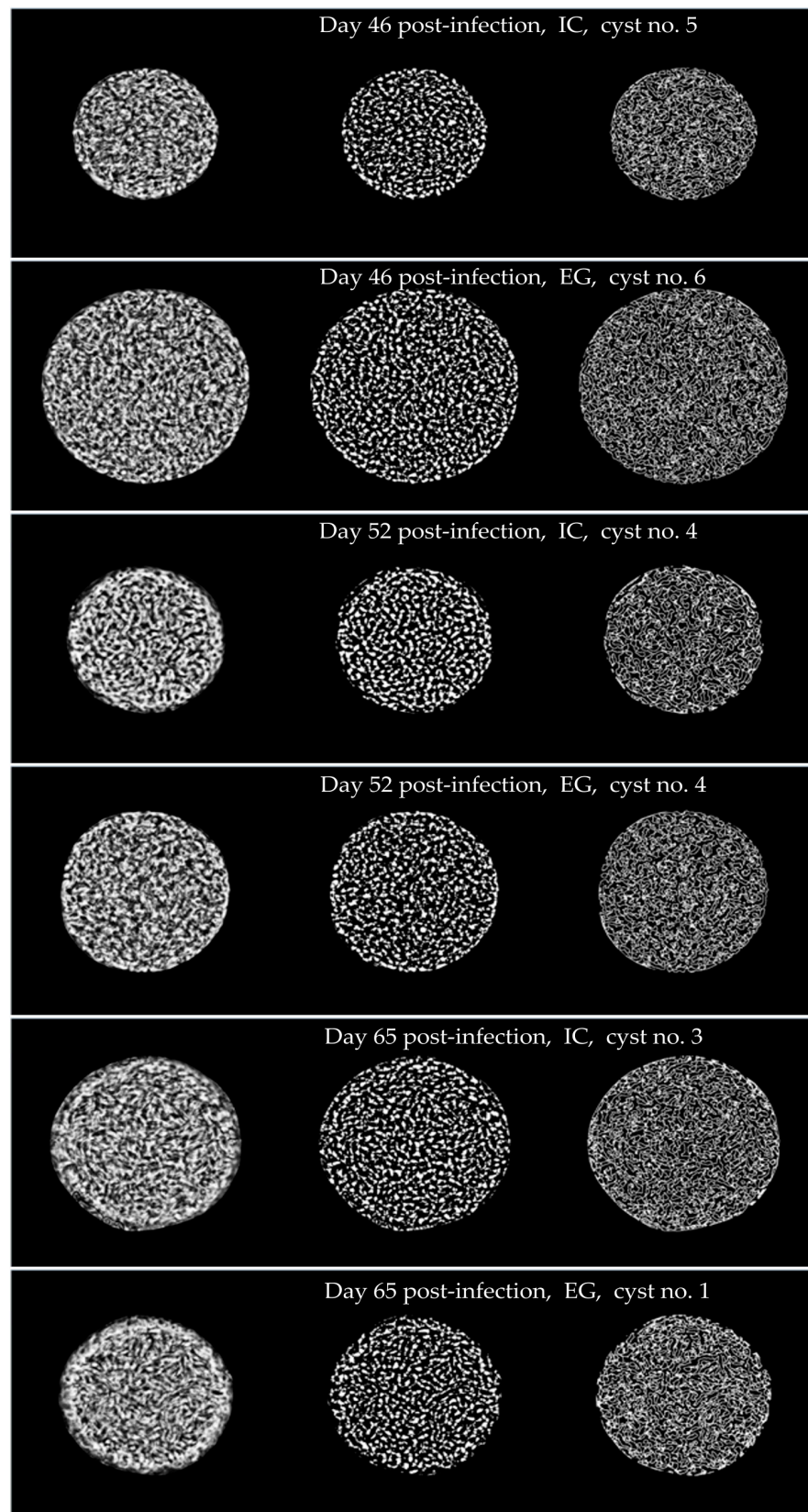
Figure 2. High-contrast high-resolution *T. gondii* cyst images (several representative example images). Leftmost: contrast enhanced; middle: transformed images used for particle analysis; rightmost: transformed images used for fractal analysis.

2.5.1. Morphological Analysis

Morphological analysis was employed to check the cysts' size and shape. The cyst *Area*, *Perimeter*, and circularity, *C*, were accurately determined by the ImageJ software. The cyst circularity, *C*, is defined as

$$C = 4\pi \times \frac{Area}{(Perimeter)^2}. \tag{1}$$

It is a measure of how close a shape is to a perfect circle. Shapes close to a circle have a *C* close to 1.0, whereas elongated shapes have a *C* close to 0.0. The cyst *Perimeter* was used to calculate the mean diameter for each cyst, which showed an excellent agreement with the diameters measured directly under the microscope. The *Area* was saved to be used in the calculation of packing density, *PD*.

2.5.2. Particle Analysis

For particle analysis, the enhanced contrast images underwent local Niblack thresholding and conversion to binary images. The default Niblack weighting coefficient of 0.2 for light objects on the dark background was kept for all images. The local threshold value at each pixel was calculated taking into account the neighborhood around that pixel, which was empirically chosen as a circular area (window) of a 28 px window radius. The neighborhood mean value of grayscale intensity was summed with the weighted standard deviation of grayscale intensity, resulting in the local threshold at each pixel:

$$t_{\mathrm{Ni}} = \mu(w) - 0.2{\cdot}\sigma(w). \tag{2}$$

In (2), $\mu(w)$ and $\sigma(w)$ correspond to the mean and standard deviation of grayscale intensities within a local neighborhood window of size $w = 28$ px. A different threshold for every pixel is based on the grayscale properties of the neighboring pixels [37].

The images were converted to binary. The watershed segmentation in ImageJ was performed next, in order to somehow work around the fact that the bradyzoites are extremely densely packed and overlap each other. The term watershed originates from the analogy with topography [38,39], where a catchment basin corresponds to the set of points whose path of steepest descent terminates in the same local minimum of the "height" function (pixel grayscale intensity minima, or pixel grayscale intensity maxima if an image is inverted). One of the very efficient early algorithms used an "immersion simulation" [38], imagining a water level rising from the local minima and flooding the basins. At each pixel where the water from two different minima would merge, a "dam" has to be built. At the end of the "immersion", each minimum is completely surrounded by dams, i.e., watersheds delimiting its associated catchment basin. Algorithms working with binary images often use the inversed distance transformation.

Although the number of particles generated by segmentation could be somewhat larger than the actual number of bradyzoites in a studied cross-section, e.g., the front part and the rear part of an overlapped bradyzoite could be counted as two particles, identical treatment of all cyst images ensured an accurate assessment of relative particle numbers. The particle counting procedure, currently available in ImageJ, is known to work properly only with clearly separated particle areas. The obtained particle numbers, N_{p}, were expected to be proportional to the actual numbers of bradyzoites within a cyst. The parameter of interest for cyst characterization, packing density, expressed in μm^{-2}, was obtained as

$$PD = \frac{N_{\mathrm{p}}}{Area}. \tag{3}$$

2.5.3. Fractal Analysis

As has been shown previously [25], the patterns of bradyzoite packing exhibit a fractal character, with the fractal dimension around 1.75. Whereas the *PD* describes the

occupancy of the cysts, fractal parameters relate to the structural and textural properties of a pattern of bradyzoite contours. For example, if the bradyzoites underwent changes in size and particularly in roughness or raggedness of their contours, due to some external factors, one could expect to observe changes in the fractal parameters. These changes occur independently of the possible alterations in the numbers of bradyzoites and *PD*.

Starting from the high-contrast images in the leftmost column of Figure 2, we applied the global Otsu threshold to the entire cyst images, adjusting the threshold grayscale intensity to best outline the bradyzoite contours. Then, we adjusted the lower histogram value to keep only the narrow interval of gray tones including the Otsu threshold. In that manner, we obtained the relatively thin lines outlining the bradyzoite contours, shown in the right column of Figure 2. We took the 520×520 px^2 sized cutouts from the region close to the cyst center to acquire equally sized visual texture images for all analyzed cysts. Fractal analysis was carried out on binary images (contour outlines) using the FracLac plugin (A. Karperien, Charles Sturt University, Bathurst, Australia) for ImageJ software [24].

We applied scaled series with a 7/8 ratio, meaning that an enlargement of consequent grid cell size was about 1/8, guaranteeing a sufficient number of relatively dense data points for fitting the regression lines. Here, a total of 25 grid cell sizes were applied to obtain the data points used for fitting the regression curves, describing the scale–count power law dependence. Namely, grid cells sized $\varepsilon \in \{16, 19, 21, 24, 28, 32, 36, 41, 47, 54, 62, 70, 81, 92, 105, 120, 137, 157, 180, 205, 234, 268, 306, 350, 400\}$ px were used. Figure 3 shows an example bradyzoite contour outline covered by grid cells of different sizes, ε. Twelve random grid positionings per image were used.

$\varepsilon = 16$ px $\qquad\qquad \varepsilon = 36$ px $\qquad\qquad \varepsilon = 81$ px
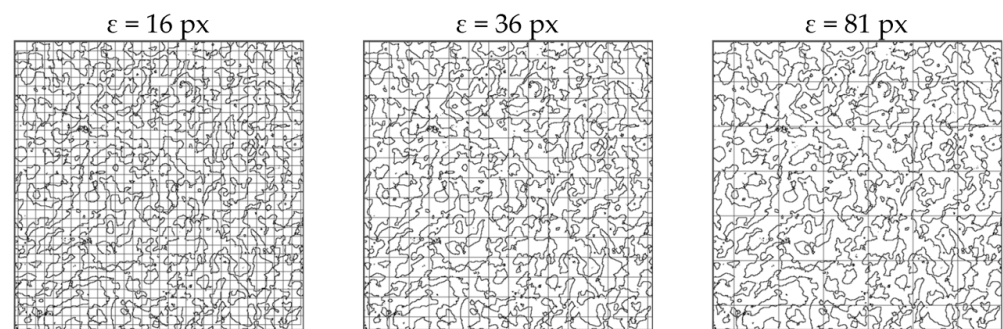
Figure 3. Grids of different grid cell sizes, ε, used to cover a binary two-dimensional (2D) pattern while obtaining the data points for the scale–count dependence.

The cumulative mass method, to determine the fractal dimension, *FD*, and fractal lacunarity, *L*, makes an assessment of the probability of finding m pixels inside a cell of size ε, $P(m, \varepsilon)$. This is carried out by counting pixels inside the grid cells and normalizing the obtained pixel count data for the total probability of one, $\sum_m P(m, \varepsilon) = 1$. The first-order mass moment, $M(\varepsilon)$, and the second-order mass moment, $M^2(\varepsilon)$, were obtained as:

$$M(\varepsilon) = \sum_m m P(m, \varepsilon), \ M^2(\varepsilon) = \sum_m m^2 P(m, \varepsilon). \tag{4}$$

The *FD* was then estimated from the $(\varepsilon, M(\varepsilon))$ data as:

$$FD = \lim_{\varepsilon \to 0} \frac{\ln M(\varepsilon)}{\ln \varepsilon}. \tag{5}$$

Adequacy of regression line fit was estimated based on the correlation coefficient, r^2, which was close to one for all analyzed images, confirming almost linear data and high *FD* estimate accuracy. The mean lacunarity, *L*, is obtained by averaging lacunarities per

grid size, ε, calculated from the first-order and second-order mass moments as given below. The lacunarity for each grid size corresponds to the squared coefficient of variation.

$$\lambda(\varepsilon) = \frac{\langle M^2(\varepsilon)\rangle - \langle M(\varepsilon)\rangle^2}{\langle M(\varepsilon)\rangle^2}, \; L = \langle \lambda(\varepsilon)\rangle. \tag{6}$$

2.6. Statistical Analysis

Statistical analysis was performed using GraphPad Prism 8.0.1. (GraphPad Software, San Diego, CA, USA). Shapiro–Wilk and Kolmogorov–Smirnov tests, as well as Q–Q plots, were used to test the normality of the dataset. Image data were evaluated by analysis of variance (ANOVA) and Tukey's test for post hoc analysis, or Kruskal–Wallis with Dunn's post hoc test, depending on the data distribution. The independent-samples *t*-test was used when comparing two sets of data, as well as the Mann–Whitney U test for comparing data with non-normal distribution. For analysis of correlation, Spearman's or Pearson's rank correlation tests were used, depending on the data distribution. The level of significance was $p \le 0.05$.

2.7. Ethics Statement

The study protocol was approved by the State Ethics Committee (Veterinary Directorate of the Ministry of Agriculture, Forestry and Water Management of Serbia decision no. 323-07-07496/2022-05). The animal experiments were conducted concordant to procedures described in the National Institutes of Health Guide for Care and Use of Laboratory Animals (Washington, DC, USA). All efforts were made to minimize suffering.

3. Results

In vivo models of RT used for harboring images required for ImageJ analysis conducted in this study were established by administering the combination of cyclophosphamide and hydrocortisone to mice chronically infected with one of two available *T. gondii* strains of human origin. After the establishment of chronic infection, and exclusion of uninfected mice ($n = 4$ for BGD1, and $n = 1$ for the BGD26 strain), surviving animals were assigned to treatment with immunosuppressant drugs (EG, $n = 54$ for BGD1 and $n = 5$ for the BGD26 strain) or left untreated as IC ($n = 28$ for BGD1 and $n = 3$ for the BGD26 strain). Signs of clinical deterioration in mice infected with either of the two strains were most pronounced in the second week of infection, as well as during the second week of combined treatment using both immunosuppressant drugs. The BGD26 strain appeared to be more virulent with a mortality rate of 83.7%, compared to BGD1 (16.3%). The majority of animals infected with either the BGD1 or BGD26 strain that succumbed to the infection died during the second week post-infection (10.2% and 61.2%, respectively) (Figure 4). During the treatment, the mortality rate was 7.4% for the BGD1 strain, while all treated animals infected with the BGD26 strain survived. According to qPCR results from peripheral blood samples, RT was diagnosed in 26.7% and 60% of animals infected with the BGD1 and BGD26 strain, respectively. Positive qPCR reactions from peripheral blood are presented in Figures S1–S10.

A total of 90 high-resolution images of *T. gondii* brain cysts obtained from established in vivo models of RT were analyzed for diameter (*D*), circularity (*C*), packing density (*PD*), fractal dimension (*FD*), and lacunarity (*L*), using ImageJ software. The analyzed cysts differed according to the parasite strain, treatment (IC or EG), and peripheral blood qPCR result (PCR+ or PCR−) (Table 1). The results of the analyzed parameters are summarized in Table 2.
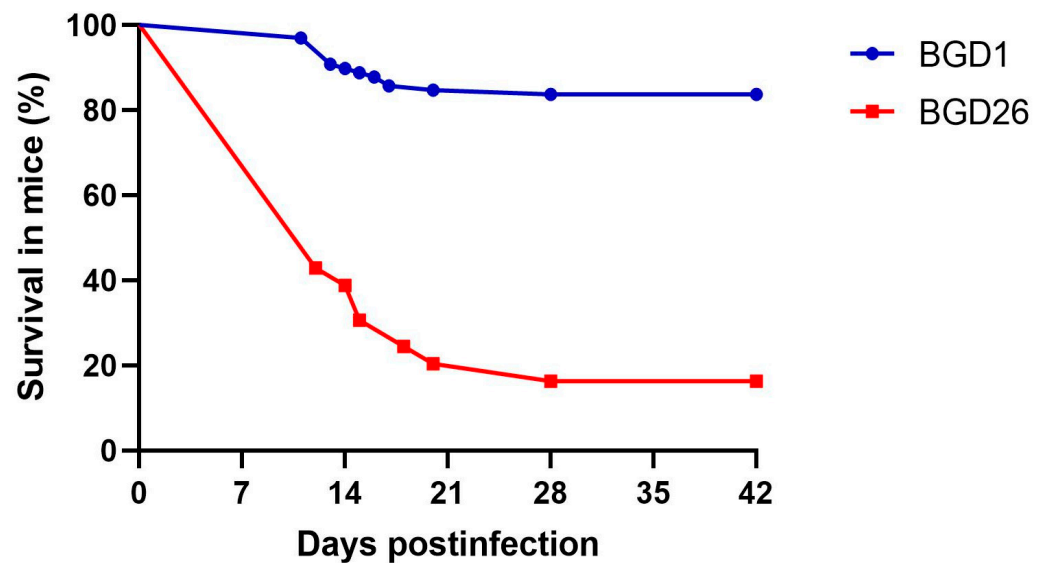
Figure 4. Survival in mice upon infection with *T. gondii* strains of human origin, BGD1 or BGD26.

Table 1. Number of analyzed cysts (images *) per strain.

Strain	IC	EG		Total
		PCR+	PCR−	
BGD1	27	7	21	**55**
BGD26	10	15	10	**35**

IC—infection control; EG—experimental group. * Only one image per cyst was selected for the final analysis.

Table 2. Strain-related differences in parameters of structural complexity of *T. gondii* cysts (mean ± SD).

Strain	Group	*D* (μm)	*C*	*PD* (μm^{-2})	*FD*	*L*
BGD1	**IC**	45.80 ± 13.00	0.994 ± 0.003	0.533 ± 0.060	1.746 ± 0.070	0.259 ± 0.076
	EG PCR−	44.55 ± 11.68	0.994 ± 0.002	0.604 ± 0.242	1.748 ± 0.069	0.259 ± 0.076
	EG PCR+	46.32 ± 16.71	0.996 ± 0.001	0.553 ± 0.073	1.749 ± 0.069	0.252 ± 0.073
	Total	45.52 ± 12.85	0.994 ± 0.002	0.563 ± 0.159	1.747 ± 0.070	0.258 ± 0.076
BGD26	**IC**	32.97 ± 5.45	0.979 ± 0.011	0.415 ± 0.034	1.746 ± 0.071	0.289 ± 0.082
	EG PCR−	41.02 ± 9.86	0.988 ± 0.006	0.452 ± 0.139	1.749 ± 0.070	0.285 ± 0.083
	EG PCR+	34.29 ± 8.26	0.989 ± 0.007	0.480 ± 0.059	1.750 ± 0.067	0.294 ± 0.082
	Total	35.84 ± 8.55	0.986 ± 0.009	0.454 ± 0.087	1.749 ± 0.069	0.290 ± 0.082
p **values**		0.0049	<0.0001	<0.0001	0.6341	<0.0001

IC—infection control; EG—experimental group; *D*—diameter; *C*—circularity; *PD*—packing density; *FD*—fractal dimension; *L*—lacunarity. *p* values are shown for comparison of parameters among cysts of different strains in the IC group.

Parameters of interest (*D*, *C*, *PD*, *FD*, and *L*) were compared among four different groups within a particular strain (IC, EG, PCR+, and PCR−), as well as between the two strains.

Cyst circularity was significantly higher in the mice with confirmed RT (PCR+) compared to untreated controls (ICs) ($p < 0.05$ for BGD1 and $p < 0.001$ for the BGD26 strain) and mice with no detected reactivation (PCR−) (only for the BGD1 strain, $p < 0.05$). However, in case of the BGD26 strain, the difference was also observed in all treated mice (EG) compared to the untreated ones (IC), regardless of reactivation ($p < 0.05$).

PD analysis showed no statistically significant differences among cysts regardless of the treatment and data on reactivation of *T. gondii* infection in mice. However, a significant negative correlation between *D* and *PD* was observed in the group of untreated mice for the BGD1 strain ($\varrho = -0.384$, $p = 0.048$), but not in the treated ones. However, an inversed correlation was not found in either group of mice infected with the BGD26 strain.

In contrast to morphological and particle analysis, we have found that fractal analysis parameters (*FD* and *L*) were not altered by administered immunosuppressant drugs.

Comparison of ImageJ-derived parameters between images of cysts obtained throughout infection with *T. gondii* strains used for our model of RT revealed that *D*, *C*, and *PD* were significantly higher, while *L* was lower in the BGD1 strain in comparison to the BGD26 strain. Moreover, the differences in *C*, *PD*, and *L* between the two strains were highly significant. Opposed to that, there were no statistically significant differences in *FD* between the BGD1 and BGD26 strains (Table 2).

4. Discussion

Determination of quantitative parameters describing tissue cyst shape and occupancy, as well as their changes in various experimental settings in murine models of toxoplasmosis, could help gain further insights into the *T. gondii* strain-dependent cyst structure in brain tissue and its alterations under drug-induced immunosuppression. In our previous work, we have suggested the application potential of computational image analysis in revealing the complexity of *T. gondii* brain cysts. The majority of analyzed parameters were stable among cysts, indicating a highly uniform structure and occupancy of the *T. gondii* brain cysts of different age and parasite strains, as well as of those derived from mice of different genetic backgrounds [25].

A total of 90 high-resolution computer images of *T. gondii* brain cysts obtained from a model of RT established by using two different *T. gondii* strains (one per each experimental setting) and a combination of immunosuppressant drugs (cyclophosphamide and hydrocortisone) were analyzed in this study. We applied the methodology for image analysis, using the freely available ImageJ software, that we have previously published [25]. Morphological, particle, and fractal analysis was used to quantify the geometrical complexity of *T. gondii* brain cysts, as well as to determine if shape uniformity or structural organization of parasites inside tissue cysts were altered by applied immunosuppressive regimen.

Morphological and particle analysis revealed changes in cyst shape and occupancy in immunosuppressed mice. Circularity values in this study were remarkably close to one, confirming the almost perfectly round shape of *T. gondii* brain cysts, concurring our previous findings [25]. However, here, we observed a statistically significant increase in *C* in mice with confirmed RT. Apparently, excystation of bradyzoites in ruptured cysts triggered microscopically undetectable but statistically significant changes in cyst shape. It is known that a sphere has the lowest surface area for a given volume, and thus requires the least energy for maintaining its shape. Moreover, an increased pressure within a cyst, e.g., due to the slightly increased numbers of bradyzoites, would drive an increase in cyst circularity. Perhaps the additional rounding of brain cysts could also be interpreted as a parasite response to unfavorable events in its surroundings. This could be explained as a defense mechanism of *T. gondii* to maintain its persistence, as well as transmission to the new host, which is a tendency of every parasite [40]. Moreover, these results indicate that *C*, as a quantitative and easily obtained parameter, could be used as an additional tool for tracking the reactivation in murine models of RT and eventually replace more expensive molecular methods. Indeed, even though peripheral blood samples are extensively used for monitoring of *T. gondii* reactivation via state-of-the-art qPCR methodology, blood is not an ideal sample for PCR since it is abundant in DNA polymerase inhibitors, e.g., hem from hemoglobin, which could lead to false-negative results and undetectable reactivation. Further development of ImageJ plugins could not only minimize inconclusive or false-negative findings derived from PCR but also offer a more precise perspective into ultrastructural modifications leading to cyst instability and eventually, rupture. However, this should be

confirmed on a larger scale, by expanding the experimental model through increase in the number and variety of mice species and parasite strains.

Our methodology used for particle analysis, with a watershed algorithm as an additional tool offering precise estimation of the relative number of closely packed parasites inside cysts, was previously underlined as simple, yet highly convenient, for this purpose [25]. As other authors [41], we [25] have also previously shown that *D* and *PD* of tissue cysts were inversely correlated. The same was observed here in the case of the BGD1 strain, albeit only in the group of infected untreated mice. In cysts derived from treated mice, on the other hand, the absence of a negative correlation between *D* and *PD* indicated changes in cyst occupancy in immunosuppressed mice. It is possible that cysts underwent significant structural changes as an effect of immunosuppressant treatment, leading to alterations of the relationship between *D* and *PD* that was previously established as stable. Never before were effects of immunosuppressants in chronic *T. gondii* infection, inevitably linked to reactivation risk, evaluated using ImageJ, even though it is a highly accessible piece of software. Possible reasons likely include a lack of publicly available data and the fact that the methodology itself is not standardized for evaluation of the infection stage. However, it should not be disregarded that the majority of PCR protocols used to diagnose and monitor infection are in-house and hence also unstandardized. The capacity of ImageJ to identify, to single out and mathematically prove new, treatment-related microscopic relations in the parasitic niche within the host organism, may complement a deeper understanding of not only the infection pathogenesis but also the mechanism of action of various drugs, both registered and experimental.

In contrast to morphological and particle analysis, the structure and organization of *T. gondii* cysts originating from either of those two strains did not change despite immunosuppressive treatment or reactivation of latent infection according to fractal analysis. *FD* was very uniform among the observed groups within a particular strain. Moreover, there was no difference between the two strains, which was in accordance with our previous findings [25]. Such results indicate that the immunosuppressive treatment did not in any way affect the contours of densely packed and overlapping bradyzoites inside the brain tissue cysts, i.e., it did not significantly affect bradyzoite shape. Whereas *PD* mainly describes the occupancy of the cysts, *FD* relates to the roughness or raggedness of contours of bradyzoites. It would be interesting to investigate if future treatment options aimed at having detrimental effects to *T. gondii* bradyzoites would perhaps modify otherwise very stable *FD*s. This observation also underlines the significance of *FD* as a well-established feature of *T. gondii* cysts from various sources. The ever-increasing number of immunocompromised patients prone to reactivation triggers more and more research aimed at the development of new compounds or repurposing of existing drugs that could be active towards bradyzoites, since none of the current treatment options are. These drug candidates are highly diverse, as is the methodology used for the evaluation of their effectiveness in many research centers worldwide, emphasizing the need to gather around a method that would be feasible, objective, and precise but also cost-effective. Armando et al. [42] have proposed an algorithm for an automated detection of *T. gondii* cysts on microscopic slides based on specific parameters of *T. gondii* cysts calculated with MatLab software (v. 2013). Defining the range of *FD* values in our research is a valuable result which could be used as a valuable parameter for developing such an algorithm and associated software. Time-consuming detection of *T. gondii* cysts by microscopic slide examination requires experienced microscopist. Thus, ImageJ could be used for the future upgrade of bioassay, a gold-standard, confirmatory diagnostic test based on microscopic identification of *T. gondii* cysts in brain samples of mice inoculated with biological samples (blood, amniotic fluid, cerebrospinal fluid, etc.). Although still used in specialized laboratories, time-consuming and labor-intensive bioassay is largely obsolete in most diagnostic and research centers, often due to deficiency in highly trained staff and objective, quantifiable approach in results interpretation, which is an undisputable asset of an ImageJ-based methodology. Moreover, ImageJ could find its application in chemotherapy studies as well. Namely, brain cyst

counts, but also their in-depth characteristics, are valuable experimental results in murine models of toxoplasmosis. Tracking the reduction of brain cyst burden in chemotherapy experiments by automatic detection of brain cysts on microscopic slides by ImageJ could facilitate evaluating the effects of therapeutics with anti-*T. gondii* properties, particularly those effective against cyst stage of this parasite.

T. gondii strains used for our models of RT were previously classified as type II strains and were both isolated from cases of human congenital toxoplasmosis. The presented results of the computer analysis of brain cysts highlight the digital methodology as an additional objective approach in distinguishing strains of *T. gondii*, which can be combined with the known clinical presentation in congenitally infected infants and data obtained from extensive in vivo studies. Namely, while there were no clinical signs of infection in newborns infected with the BGD1 strain, the one infected with BGD26 presented with hydrocephalus and epilepsy. Furthermore, the results derived from established models of RT indicate that there is a difference in virulence between these strains. During acute toxoplasmosis, the mortality rate in mice infected with the BGD26 strain was five times higher than in BGD1-infected mice. This virulence apparently also affected the incidence of RT, as the mice infected with the BGD26 strain were almost three times more prone to reactivation. Furthermore, according to computational analysis, these differences reflected in the structure of tissue cysts, since the majority of analyzed parameters were strain-dependent. Namely, we have shown that cysts of a less virulent BGD1 strain were larger, more densely packed, and with a more pronounced spherical shape. The higher circularity of the strain could be responsible for its better stability in brain tissue of an immunocompromised host. In contrast to *FD*, which remained uniform, lacunarity, *L*, was significantly lower in the BGD1 strain compared to BGD26, which confirmed our previous observations [25]. Apparently, the homogeneity of structure inside tissue cysts quantified here by *L* depends on the *T. gondii* strain. Although we have previously speculated it could be associated with the number of passages in laboratory animals, the intrinsic features such as virulence of a particular strain could be another explanation. According to our results, more homogeneous cysts originated from the BGD1 strain, which is a strain of lower virulence and reactivation rate compared to BGD26.

The results of the present study indicate that there is in fact a low level of uniformity in the structure of brain cysts derived from two different *T. gondii* strains, as opposed to our previous observation regarding the complexity of *T. gondii* cysts [25]. In addition to parasite strains used for infection, other experimental conditions such as life stage of the parasite, route of infection, and genetic background of the host affect infection dynamics and further hamper the interpretation of experimental results [43,44]. In the present study, the possible impact of such variables was excluded by providing identical, strictly controlled experimental conditions. Namely, the i.p. application of the precisely counted exact number of tachyzoites per mouse (Swiss-Webster females, 18–20 g) herein allowed for more precise comparison of strain-related differences in the structure of *T. gondii* brain cysts. On the other hand, almost half of the analyzed images from previously published studies originated from a collection stored in the NRL's photo archive [25], thus lacking the uniform standard.

In conclusion, these results pave the way for the further application of image analysis in experimental models of toxoplasmosis. This innovative approach sheds new light on structural changes of the *T. gondii* cyst stage in an immunocompromised host, allowing for their objective quantitative analysis. Furthermore, the availability of a sustainable animal model of RT alongside advanced, computer-based image analysis of cysts obtained in chemotherapy experiments offers an immense potential to, in time, enable optimization and standardization of the evaluation of effects of novel therapeutics for *T. gondii*. It could provide a straightforward and cost-effective mathematically quantifiable computer-based approach to analysis of the effectiveness of potential drug candidates in chemotherapy experiments, which remains to be investigated in future studies.

References

1. Dubey, J.P. Advances in the life cycle of *Toxoplasma gondii*. *Int. J. Parasitol.* **1998**, *28*, 1019–1024. [CrossRef]
2. Weiss, L.M.; Dubey, J.P. Toxoplasmosis: A history of clinical observations. *Int. J. Parasitol.* **2009**, *39*, 895–901. [CrossRef]
3. Augusto, L.; Wek, R.C.; Sullivan, W.J., Jr. Host sensing and signal transduction during *Toxoplasma* stage conversion. *Mol. Microbiol.* **2021**, *115*, 839–848. [CrossRef]
4. Martynowicz, J.; Doggett, J.S.; Sullivan, W.J., Jr. Efficacy of Guanabenz Combination Therapy against Chronic Toxoplasmosis across Multiple Mouse Strains. *Antimicrob. Agents. Chemother.* **2020**, *64*, e00539-20. [CrossRef]
5. Hamie, M.; Najm, R.; Deleuze-Masquefa, C.; Bonnet, P.A.; Dubremetz, J.F.; El Sabban, M.; El Hajj, H. Imiquimod Targets Toxoplasmosis Through Modulating Host Toll-Like Receptor-MyD88 Signaling. *Front. Immunol.* **2021**, *12*, 629917. [CrossRef]
6. Rodriguez, J.B.; Szajnman, S.H. An updated review of chemical compounds with anti-*Toxoplasma gondii* activity. *Eur. J. Med. Chem.* **2023**, *262*, 115885. [CrossRef]
7. Angel, S.O.; Vanagas, L.; Ruiz, D.M.; Cristaldi, C.; Saldarriaga Cartagena, A.M.; Sullivan, W.J., Jr. Emerging Therapeutic Targets Against *Toxoplasma gondii*: Update on DNA Repair Response Inhibitors and Genotoxic Drugs. *Front. Cell. Infect. Microbiol.* **2020**, *10*, 289. [CrossRef] [PubMed]
8. Silva, M.D.; Teixeira, C.; Gomes, P.; Borges, M. Promising Drug Targets and Compounds with Anti-*Toxoplasma gondii* Activity. *Microorganisms* **2021**, *9*, 1960. [CrossRef] [PubMed]
9. Dunay, I.R.; Gajurel, K.; Dhakal, R.; Liesenfeld, O.; Montoya, J.G. Treatment of toxoplasmosis: Historical perspective, animal models, and current clinical practice. *Clin. Microbiol. Rev.* **2018**, *31*, e00057-17. [CrossRef] [PubMed]
10. Koundal, D.; Gupta, S. *Advances in Computational Techniques for Biomedical Image Analysis*; Academic Press: Cambridge, MA, USA, 2020; pp. 299–308.
11. Madabhushi, A.; Lee, G. Image analysis and machine learning in digital pathology: Challenges and opportunities. *Med. Image Anal.* **2016**, *33*, 170–175. [CrossRef]
12. Sbalzarini, I.F. Seeing is Believing: Quantifying is Convincing: Computational image analysis in biology. In *Focus on Bio-Image Informatics. Advances in Anatomy, Embryology and Cell Biology*; De Vos, W., Munck, S., Timmermans, J.P., Eds.; Springer: Cham, Switzerland, 2016; Volume 219. [CrossRef]
13. AlSheikh, M.H.; Al-Saidi, N.M.G.; Ibrahim, R.W. Dental X-ray identification system based on association rules extracted by k-symbol fractional Haar functions. *Fractal Fract.* **2022**, *6*, 669. [CrossRef]
14. Pantic, I.; Valjarevic, S.; Cumic, J.; Paunkovic, I.; Terzic, T.; Corridon, P.R. Gray level co-occurrence matrix, fractal and wavelet analyses of discrete changes in cell nuclear structure following osmotic stress: Focus on machine learning methods. *Fractal Fract.* **2023**, *7*, 272. [CrossRef]
15. Djuričić, G.J.; Radulović, M.; Sopta, J.P.; Nikitović, M.; Milošević, N.T. Fractal and Gray Level Cooccurrence Matrix computational analysis of primary osteosarcoma magnetic resonance images predicts the chemotherapy response. *Front. Oncol.* **2017**, *7*, 246. [CrossRef] [PubMed]

16. Prieto-Vázquez, A.Y.; Cuautle-Estrada, A.; Grave-Capistrán, M.A.; Ramírez, O.; Torres-SanMiguel, C.R. Fractal analysis and FEM assessment of soft tissue affected by fibrosis. *Fractal Fract.* **2023**, *7*, 661. [CrossRef]

17. Zaia, A.; Maponi, P. Mitochondrial DNA profiling by fractal lacunarity to characterize the senescent phenotype as normal aging or pathological aging. *Fractal Fract.* **2022**, *6*, 219. [CrossRef]

18. Atupelage, C.; Nagahashi, H.; Yamaguchi, M.; Abe, T.; Hashiguchi, A.; Sakamoto, M. Computational grading of hepatocellular carcinoma using multifractal feature description. *Comput. Med. Imaging Graph.* **2013**, *37*, 61–71. [CrossRef]

19. Abdelsalam, M.M.; Zahran, M.A. A novel approach of diabetic retinopathy early detection based on multifractal geometry analysis for OCTA macular images using support vector machine. *IEEE Access* **2021**, *9*, 22844–22858. [CrossRef]

20. He, S.; Thangaraj, C.; Easwaramoorthy, D.; Muhiuddin, G. Multifractal analysis on age-based discrimination in X-ray images for sensing the severity of COVID-19 disease. *Eur. Phys. J. Spec. Top.* **2022**, *231*, 3663–3671. [CrossRef]

21. Rani, P.; Kotwal, S.; Manhas, J.; Sharma, V.; Sharma, S. Machine Learning and Deep Learning Based Computational Approaches in Automatic Microorganisms Image Recognition: Methodologies, Challenges, and Developments. *Arch. Comput. Methods. Eng.* **2022**, *29*, 1801–1837. [CrossRef]

22. Shambhu, S.; Koundal, D.; Das, P.; Hoang, V.T.; Tran-Trung, K.; Turabieh, H. Computational Methods for Automated Analysis of Malaria Parasite Using Blood Smear Images: Recent Advances. *Comput. Intell. Neurosci.* **2022**, *2022*, 3626726. [CrossRef]

23. Jeckel, H.; Drescher, K. Advances and opportunities in image analysis of bacterial cells and communities. *FEMS Microbiol. Rev.* **2021**, *45*, fuaa062. [CrossRef]

24. Karperien, A.L.; Jelinek, H.F. Box-counting fractal analysis: A primer for the clinician. In *The Fractal Geometry of the Brain*; Di Ieva, A., Ed.; Springer: New York, NY, USA, 2016; pp. 91–108. [CrossRef]

25. Bauman, N.; Ilić, A.; Lijeskić, O.; Uzelac, A.; Klun, I.; Srbljanović, J.; Ćirković, V.; Bobić, B.; Štajner, T.; Djurković-Djaković, O. Computational image analysis reveals the structural complexity of *Toxoplasma gondii* tissue cysts. *PLoS ONE* **2020**, *15*, e0234169. [CrossRef] [PubMed]

26. Passweg, J.R.; Baldomero, H.; Bader, P.; Bonini, C.; Cesaro, S.; Dreger, P.; Duarte, R.F.; Dufour, C.; Kuball, J.; Farge-Bancel, D.; et al. Hematopoietic stem cell transplantation in Europe 2014: More than 40000 transplants annually. *Blood Marrow Transplant.* **2016**, *51*, 786–792. [CrossRef] [PubMed]

27. Djurkovic-Djakovic, O.; Milenkovic, V. Murine model of drug induced reactivation of *Toxoplasma gondii. Acta Protozool* **2001**, *40*, 99–106.

28. Carreras, E.; Dufour, C.; Mohty, M.; Kröger, N. (Eds.) *The EBMT Handbook: Hematopoietic Stem Cell Transplantation and Cellular Therapies*, 7th ed.; Springer: Cham, Switzerland, 2019.

29. Silva, L.A.; Brandão, G.P.; Pinheiro, B.V.; Vitor, R.W. Immunosuppression with cyclophosphamide favors reinfection with recombinant *Toxoplasma gondii* strains. *Parasite* **2012**, *19*, 249–257. [CrossRef] [PubMed]

30. Jin, Y.; Yao, Y.; El-Ashram, S.; Tian, J.; Shen, J.; Ji, Y. The Neurotropic Parasite *Toxoplasma gondii* Induces Astrocyte Polarization through NFκB Pathway. *Front. Med.* **2019**, *6*, 267; Erratum in *Front. Med.* **2019**, *6*, 299. [CrossRef]

31. Djurković-Djaković, O.; Klun, I.; Khan, A.; Nikolić, A.; Knezević-Usaj, S.; Bobić, B.; Sibley, L.D. A human origin type II strain of *Toxoplasma gondii* causing severe encephalitis in mice. *Microbes Infect.* **2006**, *8*, 2206–2212. [CrossRef] [PubMed]

32. Stajner, T.; Bobic, B.; Klun, I.; Nikolic, A.; Srbljanovic, J.; Uzelac, A.; Rajnpreht, I.; Djurkovic-Djakovic, O. Prenatal and early postnatal diagnosis of congenital toxoplasmosis in a setting with no systematic screening in pregnancy. *Medicine* **2016**, *95*, e2979. [CrossRef]

33. Rajnpreht, I.; Klun, I.; Uzelac, A.; Bobić, B.; Nikolić, A.; Srbljanović, J.; Djurković-Djaković, O. Vero cells as an in vitro model system for the propagation of type-3 *Toxoplasma gondii* tachyzoites. In Proceedings of the 12th European Multicolloquium of Parasitology, Turku, Finland, 20–24 July 2016.

34. Desmonts, G.; Remington, J.S. Direct agglutination test for diagnosis of Toxoplasma infection: Method for increasing sensitivity and specificity. *J. Clin. Microbiol.* **1980**, *11*, 562–568. [CrossRef]

35. Huyan, X.H.; Lin, Y.P.; Gao, T.; Chen, R.Y.; Fan, Y.M. Immunosuppressive effect of cyclophosphamide on white blood cells and lymphocyte subpopulations from peripheral blood of Balb/c mice. *Int. Immunopharmacol.* **2011**, *11*, 1293–1297. [CrossRef]

36. Stajner, T.; Vasiljević, Z.; Vujić, D.; Marković, M.; Ristić, G.; Mićić, D.; Pasić, S.; Ivović, V.; Ajzenberg, D.; Djurković-Djaković, O. Atypical strain of *Toxoplasma gondii* causing fatal reactivation after hematopoietic stem cell transplantion in a patient with an underlying immunological deficiency. *J. Clin. Microbiol.* **2013**, *51*, 2686–2690. [CrossRef]

37. Singh, T.R.; Roy, S.; Singh, O.I.; Sinam, T.; Singh, K.M. A new local adaptive thresholding technique in binarization. *Int. J. Comp. Sci.* **2011**, *8*, 271–277. [CrossRef]

38. Soille, P.; Vincent, L. Watersheds in digital spaces: An efficient algorithm based on immersion simulations. *IEEE Trans. Pattern Anal. Mach. Intell.* **1991**, *13*, 583–598. [CrossRef]

39. Kornilov, A.S.; Safonov, I.V. An overview of watershed algorithm implementations in open source libraries. *J. Imaging* **2018**, *4*, 123. [CrossRef]

40. Rougier, S.; Montoya, J.G.; Peyron, F. Lifelong persistence of toxoplasma cysts: A questionable dogma? *Trends Parasitol.* **2017**, *33*, 93–101. [CrossRef] [PubMed]

41. Watts, E.; Zhao, Y.; Dhara, A.; Eller, B.; Patwardhan, A.; Sinai, A.P. Novel approaches reveal that *Toxoplasma gondii* bradyzoites within tissue cysts are dynamic and replicating entities *in vivo. mBio* **2015**, *6*, e01155-15. [CrossRef]

42. Armando, Q.; Graciela, J. Identification of *Toxoplasma gondii* cysts in samples from Colombia using digital image processing. In Proceedings of the 2014 IEEE ANDESCON, Cochabamba, Bolivia, 15–17 October 2014; p. 1. [CrossRef]

43. Howe, D.K.; Sibley, L.D. *Toxoplasma gondii* comprises three clonal lineages: Correlation of parasite genotype with human disease. *J. Infect. Dis.* **1995**, *172*, 1561–1566. [CrossRef] [PubMed]

44. Szabo, E.K.; Finney, C.A.M. *Toxoplasma gondii*: One organism, multiple models. *Trends Parasitol.* **2017**, *33*, 113–127. [CrossRef]

Near-field formation of the UCA-based OAM EM fields and short-range EM power flux profiles

Andjelija Ž Ilić[1,*] ⓘD, Jelena Z Trajković[1] ⓘD, Slobodan V Savić[2] and Milan M Ilić[2]

[1] Institute of Physics Belgrade, University of Belgrade, Pregrevica 118, 11080 Zemun-Belgrade, Serbia
[2] School of Electrical Engineering, University of Belgrade, 11120 Belgrade, Serbia

E-mail: andjelijailic@ieee.org

Abstract

Orbital angular momentum (OAM) multiplexing is a recently considered solution for enhancing wireless and free-space optical communications channel capacity, whether implemented separately or in combination with existing multiplexing techniques. The theoretically infinite number of paraxially propagating and mutually orthogonal OAM modes is expected to increase the channel capacity. However, the orthogonality for different OAM modes has been shown to decrease for far link range distances, and the paraxiality of the OAM beams is not very good for small radiating sources. Based on the current knowledge, OAM beams are most likely to be used for short-range communications. Many models of the electromagnetic (EM) fields carrying the OAM neglect the fact that the OAM beam sources could be electrically large or introduce other approximations that are appropriate for far-field analysis only. An in-depth analysis of the short-range properties of OAM EM fields is still lacking. To address this problem, we propose the use of the infinitesimal (Hertz) dipole method customized for the analysis of the OAM EM fields. This technique can model the positioning and basic radiation properties of separate antennas or antenna sub-arrays that are the building blocks of OAM arrays exactly and efficiently. Similar modeling can represent the OAM sources for free-space optical communications. We focus here on the uniform circular antenna arrays and provide an in-depth analysis of what can and cannot be expected, in the best case, in their utilization. We assume low losses, which is a common assumption for many methods, except for computationally much more demanding full-wave

---

* Author to whom any correspondence should be addressed.

simulations. The obtained results indicate the need to simultaneously optimize the transmission of all planned OAM modes and allow estimates of the link distances that could provide adequate OAM wave reception in various cases.

(Some figures may appear in colour only in the online journal)

1. Introduction

Electromagnetic (EM) waves carrying orbital angular momentum (OAM) have been recognized as one of the key technology enablers for future wireless communications, due to the orthogonality of the OAM modes [1]. As pointed out in [2, 3], the positions of zeros of complex two-dimensional functions, representing waves in the observed plane, are the positions of wave singularities, where the phase of the wave is undefined. These positions are known as phase vortices, around which the wave power circulates in spirals. In space, the phase generally varies along the longitudinal direction. Asymptotically close to the vortex, the flow lines form a tightly wound helix whose radius in general depends exponentially on the longitudinal coordinate [2]. In literature, waves carrying OAM are often denoted as vortex waves. It is important to note, however, that while eigenstates of OAM wave contain a vortex core of topological charge equal to the OAM mode number, there is no such general relation for beams that are superpositions of OAM eigenstates [4]. Although the general cases in [2, 3] were derived in the geometrical-optics regime, the same phenomena were observed at lower frequencies, provided that the source electric size was sufficiently large to support the propagation of paraxial waves.

A multitude of methods have been successfully implemented to generate the OAM modes, from microwave to optical frequencies [5–17]. Due to their relatively easy OAM mode reconfigurability and the possibility to use concentric OAM uniform circular antenna array (UCA) arrangements for multimode transmission, phased UCAs have been used with success for the generation of microwave, millimeter-wave (mmWave), and low terahertz OAM EM waves. Recently, the use of acoustic sources arranged in OAM UCAs has also been proposed [18], which can be employed in high-rate underwater acoustic communications. A review of the potential challenges for OAM wave transmission at the far-field distances can be found in [19], encompassing the power loss due to OAM beam divergence, as well as the channel crosstalk due to the transmitter–receiver misalignment. The turbulence-induced crosstalk between the modes has been studied analytically in [20]. Many of the previous investigations [21–26], have already pointed toward the most probable utility of OAM UCA in short-range communications. However, there is still a lack of in-depth investigations into the properties of such short-range OAM wave transmission.

Here we present a newly developed general method for EM wave analysis based on short dipole modeling, which is computationally efficient for large antenna arrays. We have customized this method for the analysis of UCA arrays carrying OAM waves. In antenna array optimization, this method can be combined with full-wave modeling in a trade-off between accuracy and speed. In our studied case, the OAM wave properties mostly depend on the arrangement of radiating antenna array elements, while an individual element's radiation pattern mainly

modifies the obtained EM field magnitudes. This is well-suited for short-range investigations, as it avoids approximations appropriate for far fields only. The goal of this work is (i) to introduce the method and its further possibilities apart from the single UCA case, and (ii) to utilize the method to gain detailed insights into what can be expected in short-range transmission at different frequencies, with different system electrical sizes, and at different distances from the source plane. Currently, to the best of the author's knowledge, it has not been clearly established what can be expected in different cases of short-range OAM wave transmission.

2. The method and the calculations

Several methods have been proposed so far for modeling the OAM waves used in wireless communications [21–24, 27]. In [21], the authors have developed a wireless channel matrix for an N_t-antenna UCA as a transmitter and an N_r-antenna UCA as a receiver, to study the capacity gain of the thus obtained multiple-input multiple-output system over a single-input single-output system. They have conducted an eigenvalue decomposition of a circulant matrix obtained for $N_t = N_r = N$. A similar modeling of the line of sight wireless transmission link comprising N transmitting and N receiving antennas, arranged in an UCA, has been performed in [22]. The ratio of the received and transmitted powers for each OAM order, ℓ, has been simplified using the circulant matrix properties, leading to an asymptotic formulation of the far-field link budget with equivalent OAM gains and free-space losses. In [23], a decomposition of the current distributions on the OAM antenna apertures into modified circle polynomials has been performed to derive a quasi-analytical solution for the transmittance between the two OAM antenna apertures. A method based on the aperture antennas theory has been presented in [24], combining the Hankel transforms relating source and far-field distributions with the singular value decomposition of radiation operators to quantitatively analyze the antenna performances. In [23, 24] a continuous coverage of the finite source aperture areas has been assumed. In [27], the electric field radiated by a phased UCA antenna has been expanded into a series of cylindrical waves using the Jacobi–Anger expansion. The so-obtained electric fields represent a sum of OAM modes and harmonic modes, with the ℓth OAM mode described by the Bessel function of the first kind of order ℓ.

We propose a quasi-analytical method to model OAM mode-generating antenna arrays starting from a short dipole antenna model. This was motivated by the need to build electrically large arrays necessary to generate higher-order OAM modes having a reasonably large link range [21–24]. On the other hand, the number of individually phased UCA elements should not be very large to avoid increasingly complex and costly feeding and phasing structures. In the literature, prototypes with 8 or 16 elements are typically used. Therefore, each UCA element could itself be an antenna sub-array having relatively high gain to address the increased propagation losses at high frequencies, where the use of OAM modes is envisioned. Additionally, sparsely arranged sub-arrays instead of the entire apertures being radiating surface would facilitate the transmission of multiple OAM modes through a single aperture in both millimeter-wave and optical domains.

For any antenna system, two sets of limits describing the radiating near-field (Fresnel) and far-field (Fraunhofer) regions [28] can be observed. As previously said, to boost up the overall OAM antenna array gain, the sub-array antennas would be closely packed, while the final OAM system consists of several differently phased sub-arrays. If the largest linear dimension of a sub-array equals D_s, the EM field region boundaries for sub-arrays equal

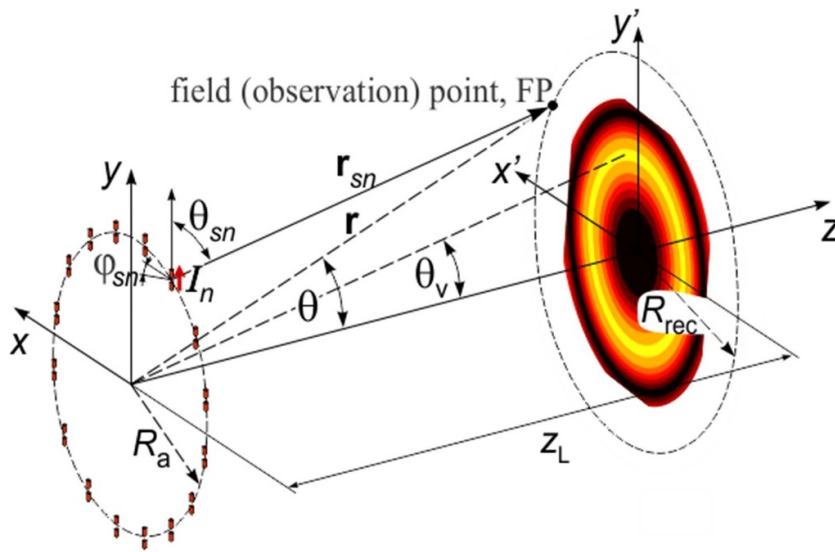$$R_{nfs} = 0.62\sqrt{D_s^3/\lambda_0}, \tag{1a}$$

Figure 1. An OAM UCA array for short-range communications ($N_a = 16$ is shown for illustration). The coordinate transformation between the global coordinate system, (x, y, z), and the local spherical coordinate system of the nth antenna, $(r_{sn}, \theta_{sn}, \varphi_{sn})$, took place to ensure the correctness of the calculations even for electrically large UCA radii, R_a. The vortex angle, θ_v, corresponds to the EM field maximum. The link distance is denoted as z_L.

$$R_{\text{ffs}} = 2D_s^2/\lambda_0, \ R_{\text{ffs}} >> D_s, \ R_{\text{ffs}} >> \lambda_0. \tag{1b}$$

The free-space wavelength corresponding to the central frequency of operation is denoted by λ_0. For distances larger than R_{nfs} (near-field boundary for sub-array), but shorter than R_{ffs} (far-field boundary for sub-array), there is still dependence of the EM field pattern on the radial distance and the radial field component is significant (Fresnel region). For distances larger than R_{ffs}, the EM field could be considered as far-field (Fraunhofer region). However, the largest linear dimension of an OAM array, equaling $2R_a$, where R_a denotes the UCA radius, is on an order of several times the sub-array size, D_s. In this case, the observation points of interest in the near-far-transition region of an OAM array belong to the far-field region of the antenna sub-arrays. Assuming that antenna and sub-array maximal linear dimensions are small compared to $2R_a$, for an OAM array as a whole we get:

$$R_{\text{nf}} = 0.62\sqrt{8R_a^3/\lambda_0}, \tag{2a}$$

$$R_{\text{ff}} = 8R_a^2/\lambda_0, \ R_{\text{ff}} >> R_a, \ R_{\text{ff}} >> \lambda_0. \tag{2b}$$

Therefore, when the observation point is in the far-field zone for the sub-array, the antennas belonging to the same sub-array can be assumed to share an identical direction vector towards the observation point. However, as shown in figure 1, when the observation point is not in the far-field zone for the whole OAM array, adopting a single direction vector towards the field (observation) point for all sub-array UCA elements would lead to inaccurate, if not entirely erroneous, results. As a result, the electric field generated by the sub-array can be modeled as

$$\mathbf{E}_{sn}(\mathbf{r}_{sn}) = \frac{F_{sn}(\beta, l_e, w_e, \theta_{sn}, \varphi_{sn})}{F_{\text{Hd}}(\beta, l_{\text{Hd}}, \theta_{sn})} \mathbf{E}_{\text{Hd},n}(\mathbf{r}_{sn}), \tag{3}$$

where $(\theta_{sn}, \varphi_{sn})$ are the direction angles of the nth sub-array towards the observation point, in a local spherical coordinate system of the nth sub-array and l_{Hd} is Hertz dipole length. Here the propagation wave number is denoted by β. Since circular polarization can be easily achieved with crossed dipoles, without the loss of generality we here focus on investigating the wave fronts resulting from linear polarization along the y-axis direction of the global coordinate system. The characteristic functions of the antennas are denoted by $F_{Hd}(\beta, l_{Hd}, \theta_{sn})$, for an infinitesimal (Hertz) dipole assuming that its axis is along y-axis, and by $F_{sn}(\beta, l_e, w_e, \theta_{sn}, \varphi_{sn})$, for the sub-arrays. The geometrical structure of a sub-array could be arbitrary; it is only symbolically represented by l_e, w_e. Let us assume F_{sn} to be independent of φ_{sn}, and the ratio of F_{sn} to F_{Hd} to depend only on θ_{sn}, as $K(\theta_{sn})$. The resulting OAM fields could then be obtained by summing the weighted dipole contributions,

$$\mathbf{E}(\mathbf{r}) = \sum_{n=1}^{N_a} \mathbf{E}_{sn}(\mathbf{r}_{sn}) = \sum_{n=1}^{N_a} K(\theta_{sn})\mathbf{E}_{Hd,n}(\mathbf{r}_{sn}). \tag{4}$$

In such cases, the $K(\theta_{sn})$ ratio would not affect the phase of $\mathbf{E}_{sn}(\mathbf{r}_{sn})$; it would only scale the magnitude. The array analysis and design could be conducted in two steps. In the first step, the ratio of characteristic functions would be calculated in advance for a known linearly polarized sub-array, to be applied in the OAM field calculations, or it could be adjusted upon determining the optimal weighting functions. In the second step, the infinitesimal (Hertz) dipoles would be used to model the helical wave fronts, which is very convenient because (i) they can be used as building blocks of more complex geometries, (ii) they can reproduce a measured or desired near-field pattern using optimization algorithms [29], and (iii) the exact calculation of their EM fields is possible [28], using the following analytical expressions:

$$\mathbf{E}_{Hd,n}(r_{sn}, \theta_{sn}, \varphi_{sn}) = \frac{j\beta}{4\pi} j\beta l_{Hd} Z_0 I_n e^{-j\beta r_{sn}} \cdot \left(((j\beta r_{sn})^{-2} + (j\beta r_{sn})^{-3}) \, 2\cos\theta_{sn} \mathbf{i}_{rn} \right.$$
$$\left. + ((j\beta r_{sn})^{-1} + (j\beta r_{sn})^{-2} + (j\beta r_{sn})^{-3}) \sin\theta_{sn} \mathbf{i}_{\theta n} \right), \tag{5a}$$

$$\mathbf{H}_{Hd,n}(r_{sn}, \theta_{sn}, \varphi_{sn}) = \frac{j\beta}{4\pi} j\beta l_{Hd} I_n e^{-j\beta r_{sn}} \cdot \left(((j\beta r_{sn})^{-1} + (j\beta r_{sn})^{-2}) \sin\theta_{sn} \mathbf{i}_{\varphi n} \right), \tag{5b}$$

where j denotes the imaginary unit, $\beta = 2\pi / \lambda_0$ is the wave number, $Z_0 \approx 120\,\pi\,\Omega$ is the vacuum intrinsic impedance, I_n is the feeding current for Hertz dipole, and $\mathbf{i}_{rn}$, $\mathbf{i}_{\theta n}$, and $\mathbf{i}_{\varphi n}$, represent the unit vectors of the spherical coordinate systems of the dipoles. Please note that $\mathbf{r}_n = (r_{sn}, \theta_{sn}, \varphi_{sn})$ represents the position vector in a local spherical coordinate system of the nth sub-array. It is obtained, for each n, by the coordinate transformation from the global Cartesian coordinates, (x, y, z) (please see figure 1). In the representation of results, the cylindrical coordinate system of an OAM array, (r, ϕ, z), is also used to represent OAM wave properties (e.g. the Poynting vector). Additionally, the polar angle, denoted as θ or θ_v, is measured from the positive z-axis, as in other works on paraxial beams. Points of interest for wireless transmission are in the vicinity and within the cone defined by θ_v, the OAM beam spreading angle, corresponding to the maxima of EM field intensity for different modes, and not near the OAM array or z-axis. The direction vectors to the observation points, therefore, differ for the different UCA elements (sub-arrays). Being far enough from the antenna sub-arrays, the $(j\beta r_{sn})^{-2}$ and $(j\beta r_{sn})^{-3}$ terms in (5a) and (5b) can be omitted and the EM field equations

simplified. We confirmed this assumption by comparing the fields in multiple examples. The radiation expressions in the simplified form are:

$$\mathbf{E}_{\mathrm{Hd},n}(r_{sn}, \theta_{sn}, \varphi_{sn}) = -\frac{\beta^2 l_{\mathrm{Hd}}}{4\pi} Z_0 I_n \frac{\mathrm{e}^{-\mathrm{j}\beta r_{sn}}}{\mathrm{j}\beta r_{sn}} \sin\theta_{sn} \mathbf{i}_{\theta n},$$ (6a)

$$\mathbf{H}_{\mathrm{Hd},n}(r_{sn}, \theta_{sn}, \varphi_{sn}) = -\frac{\beta^2 l_{\mathrm{Hd}}}{4\pi} I_n \frac{\mathrm{e}^{-\mathrm{j}\beta r_{sn}}}{\mathrm{j}\beta r_{sn}} \sin\theta_{sn} \mathbf{i}_{\varphi n}.$$ (6b)

To obtain the ℓth OAM mode, the antenna sub-arrays have to be properly phased. In UCA, radiating elements are equidistantly arranged along the circle; therefore, the phase increments in this case have to be uniform,

$$I_n = I_0 \, \mathrm{e}^{\mathrm{j}(\varphi_0 + \ell\varphi_n)} = I_0 \, \mathrm{e}^{\mathrm{j}(\varphi_0 + 2\pi\,\ell n/N_\mathrm{a})},$$ (7a)

$$|\ell_{\max}| = \tfrac{1}{2}(N_\mathrm{a} - 1).$$ (7b)

The number of elements in the OAM array, N_a, limits the number of achievable OAM modes to $\ell_{\max}$, as the EM wave front sources are defined in a finite number of points.

The main advantage of the proposed method is the use of exact analytical expressions for Hertz dipole modeling, which is computationally efficient. Additionally, the use of local spherical coordinate systems of sub-arrays (UCA elements) allows for accurate EM field calculations. Specifically, for observation points near the z-axis, distances r_{sn} to the UCA elements vary only slightly, enabling the simplification of equations. However, this simplification does not hold true for points away from the z-axis or for electrically large UCA. Such an assumption, sometimes found in literature, can limit the accuracy of the results. In [23, 24], modeling has been highly accurate, but mostly focused on the propagation direction broadside to the OAM array (along the z-axis). However, the reception of OAM waves in the regions of the EM field maxima could be much more interesting in the short-range data transmission. The OAM arrays for the short-range link can be made large enough to enable such reception. Moreover, point sources seem to be more suitable for modeling the UCA than partially continuous source area coverage. In [21, 22], antenna pairs were considered, whereas we here analyze the EM field distributions in several planes of interest. Although we plan to separately model and optimize the sub-array radiation in the future, our current work focuses on the main contribution of the phased UCA to the helical wave fronts and the formation patterns of near-field OAM waves. We considered different electric sizes of the OAM UCA arrays for OAM modes $\ell = 1$ to $\ell = 4$. It is worth noting the possibility to use the proposed method in optimizing the non-uniform as well as non-circular arrangements of the antenna sub-arrays, which can produce very high quality of the OAM waves. Such investigations will be conducted as a part of our future work. To facilitate comparison with other similar investigations, the longitudinal distances, z, were reported as the multiples of Rayleigh distance, z_R, which for the OAM UCA was approximated as [26]

$$z_\mathrm{R} = \pi R_\mathrm{a}^2/\lambda_0.$$ (8)

We have previously defined [26] the optimal link range for the short-range point-to-point and point-to-multipoint wireless communications using the OAM waves, as the distance enabling the reception in the regions of the EM field maxima. Based on the known expressions for the vortex angle θ_v [30], and assuming equal transmitting and receiving OAM array radius, R_a, the optimal link range equals

$$z_{\mathrm{L,opt}} = \frac{2\pi R_\mathrm{a}^2}{\lambda_0(|\ell| + 1)} = \frac{2z_\mathrm{R}}{(|\ell| + 1)}.$$ (9)

The vortex angle (in radians) was approximated as

$$\theta_{\mathrm{v}} \approx \frac{\lambda_0(|\ell|+1)}{2\pi R_{\mathrm{a}}}. \tag{10}$$

We note here, that the vortex angle approximation relies on the assumption of antenna currents and EM fields in the vicinity of the $z=0$ plane being non-negligible only around the R_{a} radius. An exact antenna current and EM field distribution could be obtained numerically; however, the above analytical treatment allows for a fast yet reliable assessment of the OAM EM fields of interest. From (9), it can be seen that the higher-order OAM modes should preferably be received in the Fresnel zone, requiring the appropriate modeling of the electrically large OAM arrays, even if the observation points are in the far field of the individual sub-arrays. The OAM wave reception could also occur at somewhat longer distances, but not deep in the far field, which is consistent with the conclusions given in [21, 23, 24].

3. Results and discussion

To conform to the requirement of the short dipole modeling, where the current along the dipole is uniform in each considered time instant, we took $l_{\mathrm{Hd}} = \lambda_0/25$ for the dipole length. The antenna current is set to 1 mA.

3.1. Frequency range considerations

To illustrate the possibilities of the OAM arrays at different frequencies, we present the results for several scaled models. The OAM array radius, at each frequency point, is set as $R_{\mathrm{a}} = 10\lambda_0$ ($\beta R_{\mathrm{a}} = 20\pi$), to have moderate vortex angle spreading. The OAM array is positioned in the $z=0$ plane and the observation plane is $z_{\mathrm{L}} = 200\lambda_0$. Expressed in terms of Rayleigh length, $z_{\mathrm{L}} \approx 0.64 z_{\mathrm{R}}$, which is close to optimal for $\ell = 2$. Figure 2 confirms that the vortex angle (dashed horizontal lines, axis on the right) for the fixed OAM UCA electrical size remains constant at different frequencies, as expected from (10). The angle θ_{v} obtained numerically from the scaled models is considered more accurate than the analytical result (10). The calculated differences between the two results were less than 8%. On the other hand, it is interesting to notice that the OAM field E_y in the observation plane at the θ_{v} angle, under an assumption of low losses, increases linearly with frequency. Such an assumption, of course, represents the upper limit or the best-case scenario of what can be expected for the OAM field E_y; it is depicted in figure 2 by the solid lines, axis on the left. In practice, the atmospheric absorption varies with frequency, making certain frequencies more suitable for wireless transmission. Additionally, due to different technological implementations in various bands, losses may occur due to feeding structures, OAM wave generation methods, and other factors, which may result in further decreases in the E_y values. However, it is important to keep in mind the upper limits of E_y, and therefore the maximal receivable power.

When the electrical size of the source is kept the same, the Rayleigh distance is inversely proportional to frequency. If some reasonable wireless communication distance is desired, the electrical size of the transmitting and receiving arrays has to be increased as the square root of frequency. The decrease in the Rayleigh distance would then be compensated for by the more collimated beams. For example, $R_{\mathrm{a}} = 10\lambda_0$ at 10 GHz corresponds to $z_{\mathrm{R}} \approx 9.42$ m. To keep the same z_{R} for different frequencies, R_{a} is taken to depend on the square root of wavelength λ_0, rather than on λ_0 as in the previous example. Figure 3 shows the electric field E_y (solid lines), and the vortex angle θ_{v} (dashed lines), as functions of frequency at the fixed plane $z_{\mathrm{L}} = 6$ m from the source plane.
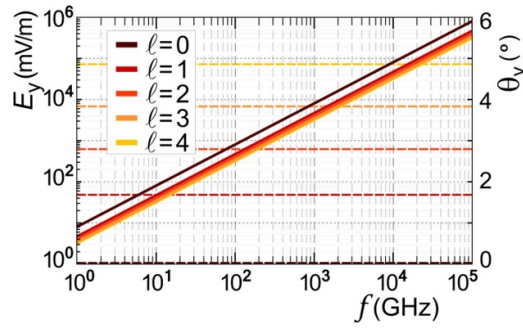
Figure 2. Dependence of the vortex angle θ_v (dashed lines) and the OAM field E_y (solid lines) on frequency, for the fixed electrical size of an OAM array, $R_a = 10\lambda_0$, and the observation plane $z_L = 200\lambda_0$.
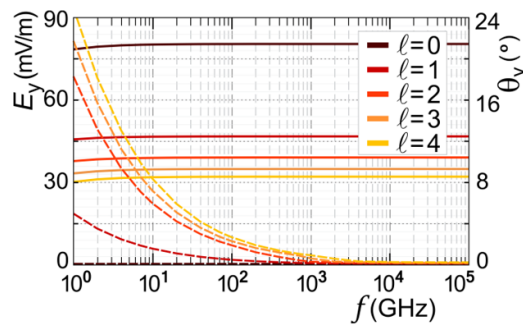

Figure 3. Dependence of the vortex angle θ_v (dashed lines) and the OAM field E_y (solid lines) on frequency, for the fixed Rayleigh distance, $z_R \approx 9.42$ m, and the observation plane $z_L = 6$ m.

Based on this example we see that similar link ranges and field levels can be achieved at different frequencies. However, due to the significant increase in electrical size at higher frequencies, both the source and the receiver would need to be implemented as radiating apertures instead of OAM UCA arrays. On the other hand, using OAM waves at lower frequencies may be impractical due to the large physical size of the systems. Finally, the limiting factor at higher frequencies might be technological in nature. The scaled models used in frequency analysis had 64 antennas along the UCA; the antenna spacing for $R_a = 10\lambda_0$ was $0.98\lambda_0$, making the side lobes negligible and keeping discretization effects low. We confirmed that the results, E_y, θ_v, did not depend on varying the number of antennas, except for the maximal realizable number of modes, defined by (7*b*), and the scaled field levels, E_y.

3.2. System electrical size and OAM beam spreading

While the relation of the Rayleigh distance to the electrical size of a system applies in general, it describes the limits of operability of the OAM systems such as the OAM UCA arrays. The main culprits, when it comes to the use of many OAM modes, are the OAM beam divergence (angle θ_v) and the rapid EM field decrease in the broadside direction (away from the maxima, defined by the angle θ_v). For short-range wireless transmission, problems can be overcome by
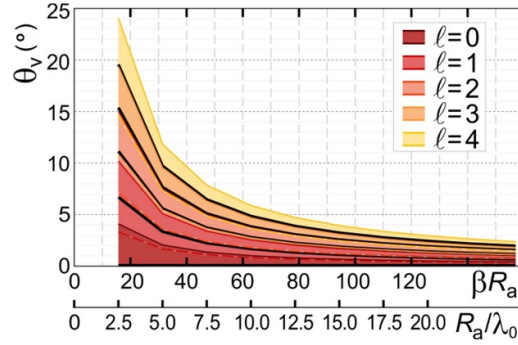
Figure 4. Dependence of the vortex angle θ_v (black thin lines) on the electrical size of an OAM UCA array source, for 60 GHz frequency ($\lambda_0 = 5$ mm). Shaded regions correspond to the angles of 3 dB EM field intervals about the maxima.

Table 1. Maximal EM fields corresponding to the vortex angle θ_v, for 60 GHz frequency and $z_L = 1$ m distance ($\beta z_L = 400\pi$)[a].

EM field component	OAM mode				
	$\ell = 0$	$\ell = 1$	$\ell = 2$	$\ell = 3$	$\ell = 4$
$|E_y|$ (mV m^{-1})	119.92	69.79	58.19	51.80	47.46
$|E_x|$ (mV m^{-1})	5.0×10^{-18}	0.14	0.13	0.14	0.16
$|E_z|$ (mV m^{-1})	1.7×10^{-16}	4.74	4.74	4.59	4.44
$|H_x|$ (μA m^{-1})	318.09	184.66	153.84	136.65	124.84
$|H_z|$ (μA m^{-1})	2.0×10^{-16}	21.52	29.45	35.49	40.28
$|H_{xz}|$ (μA m^{-1})	318.09	184.86	154.29	137.40	125.93

[a] with the adopted simulation settings, the radiated power per Hertz dipole equals 1.26 μW.

electrically large OAM UCA designs. Figure 4 shows the decrease in the OAM beam divergence (angle θ_v) with the OAM array size. The results correspond to the 60 GHz frequency ($\lambda_0 = 5$ mm), within the unlicensed millimeter-wave band offering 9 GHz of available communication bandwidth. We calculated the EM fields in the plane $z_L = 200\lambda_0$ ($\beta z_L = 400\pi$). Similar to the EM fields obtained by superimposing infinitesimal source point contributions of a circular OAM source area, the constructive or destructive summation of OAM UCA field components results in the same angles of EM field maxima and minima for OAM modes, when geometric dimensions are scaled. Our calculations also show that the EM field maxima, for an angle θ_v at a certain distance z_L, did not depend significantly on the electrical size of an array, but dominantly on the distance z_L. Table 1 lists the EM field's effective values in the plane $z_L = 200\lambda_0$ for different mode numbers. Please note that $|E_x|$ is negligible, less than 0.5% of $|E_y|$, and all other EM field components are in phase. We also notice that the field components are mainly those described by (6*a*) and (6*b*), and therefore, the simplified expressions can be used in system optimization. In addition to the vortex angle, θ_v, denoted by the black thick lines, figure 4 also shows the angles corresponding to the 3 dB intervals of EM fields about the maxima. In figure 4, the 3 dB EM field intervals are depicted by different colors (shades of gray in print, and shades of red online). There is some overlapping for the consecutive modes, which is why sometimes only the odd or only the even modes are used in practical implementations to provide spatial separation.

3.3. Poynting vector and EM power flux

As a further point of interest, we investigate the properties of the Poynting vector in a short-range scenario for different electrical sizes of OAM arrays and varying distances from the source plane, i.e. the assumed link range. Firstly, figure 5(a) depicts the dependence of the axial and radial components of the Poynting vector on the electrical size, R_a/λ_0, of an OAM UCA array. The imaginary parts of all components were confirmed to be negligible. The radial to the axial component ratio in all cases is consistent with the vortex angle, i.e. the Poynting vector direction is aligned with the cone of EM field maxima, as expected. This ratio decreases with the decrease of angle θ_v. All data presented in figures 5(a)–(d) correspond to the $z_L = 6.4$ m distance from the source plane, which is close to Rayleigh distance, z_R, for $R_a = 20\lambda_0$, for the 60 GHz frequency ($\lambda_0 = 5$ mm). In the source plane, 64 antennas were equidistantly arranged along the UCA, whereas in the observation plane, z_L, data was averaged over 720 equidistant points along the circle of the maximal EM field, as determined by the angle θ_v. Figure 5(b) shows the ratio of the maximal azimuthal component of the Poynting vector to its radial component, which decreases with the mode number and increases with the array's electrical size. Maximal variation of the azimuthal and radial components along the circle of maximal EM field in the z_L plane is presented in parts (c) to (f) of figure 5. The OAM UCA array size of $R_a = 20\lambda_0$ was considered in figures 5(c) and (e), while the size was $R_a = 5\lambda_0$ in figures 5(d) and (f). These azimuthal and radial component variations follow a certain development as the OAM wave propagates. In figure 5(e), azimuthal and radial variations are shown relatively close to the source plane, in terms of the Rayleigh distance, much before the Rayleigh distance for $R_a = 20\lambda_0$ was reached. As opposed to that, figure 5(d) shows variations for many multiples of the Rayleigh distance in the $R_a = 5\lambda_0$ case. The $z_L = 6.4$ m distance in part (c) is close to the Rayleigh distance for $R_a = 20\lambda_0$. The $z_L = 0.4$ m distance in part (f) is close to the Rayleigh distance for the array's electrical size $R_a = 5\lambda_0$. We notice mutual similarities in figures 5(c) and (f), apart from different ΔP_r variations for the two distances resulting from the differences in vortex spreading angles. Point (0,0) on the graphs corresponds to the points above the positive *x*-axis.

In relation to the maximal receivable power at the receiving end, many publications, e.g. [22–24], considered asymptotic expressions for large (far-field) distances, indicating the faster EM field decay for higher OAM modes:

$$\frac{P_{rec}}{P_{tr}} \sim \left(\frac{\lambda_0}{4\pi z_L}\right)^{2(\ell+1)}. \tag{11}$$

In the above equation, P_{rec} denotes the received power and P_{tr} the transmitted power. The free-space loss, usually proportional to the squared distance as for $\ell = 0$, is rapidly increased for higher-order OAM modes. This result is a consequence of the destructive summation of radiation of individual antennas leading to the ℓth order zeros in the array's radiation patterns for higher-order modes, in the broadside direction. In short-range transmission, however, it is possible to receive the EM wave in the region of EM field maxima. As the summation of radiation of individual antennas in this region is constructive, it seems reasonable to assume that the EM field decrease could easily be much slower than that given by equation (11).

We have investigated this possibility using the here proposed short (Hertz) dipole model, as well as the full-wave numerical calculations to confirm the result. Numerical EM simulations were carried out using the state-of-the-art full-wave EM modeling software package WIPL-D Pro [31–33], based on the method-of-moments. The short dipole model inherently neglects feeding and phasing losses as well as antenna element coupling. In the numerical model, azimuthally arranged microstrip patch antennas (MPAs) were used, taking the length
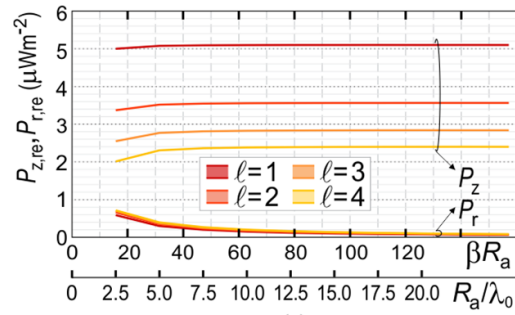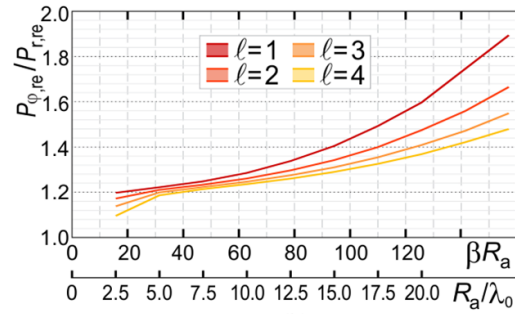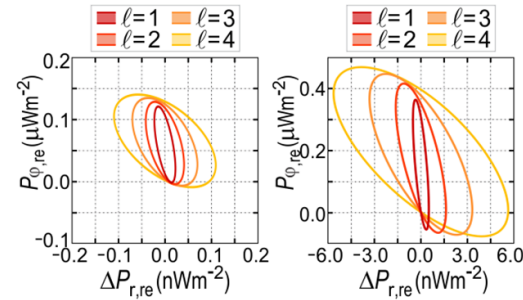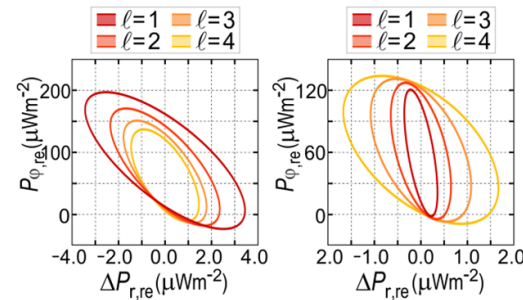
Figure 5. Dependence on the mode number and array's electrical size of the Poynting (a) axial and radial vector components, and (b) maximal azimuthal to radial component ratio. Variation of the azimuthal and radial Poynting vector components, along the ring of maximal EM field, for (c) $R_a = 20\lambda_0$, $z_L = 6.4$ m, (d) $R_a = 5\lambda_0$, $z_L = 6.4$ m, (e) $R_a = 20\lambda_0$, $z_L = 0.4$ m, (f) $R_a = 5\lambda_0$, $z_L = 0.4$ m.
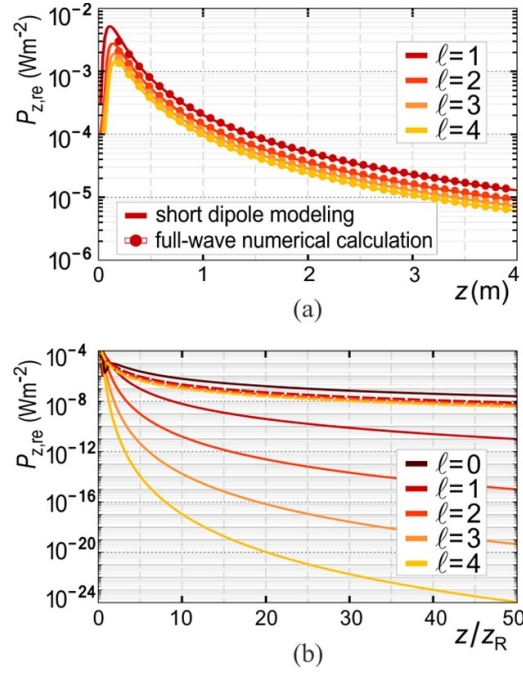
Figure 6. Axial Poynting vector decrease with distance from the source plane. (a) Comparison of short dipole modeling and numerical full-wave calculations for the short-range transmission, for a radial coordinate $R_{\text{rec}} = z_L \tan(\theta_v)$ in the observation plane, z_L, mimicking a matched size receiving UCA. (b) Comparison of results for the matched size (dashed lines) versus the fixed size (solid lines) receiving UCA (fixed $R_{\text{rec}} = R_a = 20\lambda_0$).

of the MPA as approximately one-half of the wavelength of the corresponding microstrip line [34]. The MPAs were linearly polarized with the electric field vector in the *y*-axis direction. Modeled losses were relatively low. Figure 6(a) shows the comparison of the results for the $P_{z,\text{re}}$ up to the $z_L = 4$ m observation plane, which is $z_L = 0.64 z_R$ in the considered case ($R_a = 20\lambda_0$). We used a relatively large transmitting UCA radius, with 64 antennas forming the UCA, in order to ensure small beam spreading angles ($\theta_v = 0.85°$ for $\ell = 1$ to $\theta_v = 2.44°$ for $\ell = 4$). The real part of the axial Poynting vector component, $P_{z,\text{re}}$, is shown in figure 6(a) for the cone of EM field maxima, i.e. the distance (radius) $R_{\text{rec}} = z_L \tan(\theta_v)$ from the *z*-axis in the observation plane $z = z_L$. This case corresponds to a receiving UCA which is matched in size for optimal reception. In figure 6(b), we compare the short dipole modeling results from figure 6(a), shown by the dashed lines, with those obtained assuming the fixed size receiving UCA of $R_{\text{rec}} = R_a = 20\lambda_0$ (solid lines). The 'fixed size' results in figure 6(b) match the approximate analytical estimates given by (11). The 'matched size' results in figure 6(a) exhibit a similar decrease as in the $\ell = 0$ case, emphasizing the need to stay close to the optimal reception region to avoid the rapid P_z decrease and the subsequent loss of information occurring for link distances much larger than z_R, as previously noted [22–24]. However, it is important to bear in mind that we performed calculations using the low-loss models. As the R_a and R_{rec} increase, limits to successful communication may be imposed by technological constraints.

The behavior of the axial Poynting vector in the vicinity of the Rayleigh distance, for small beam spreading angles, is illustrated by the results shown in figure 7. Simulation settings were
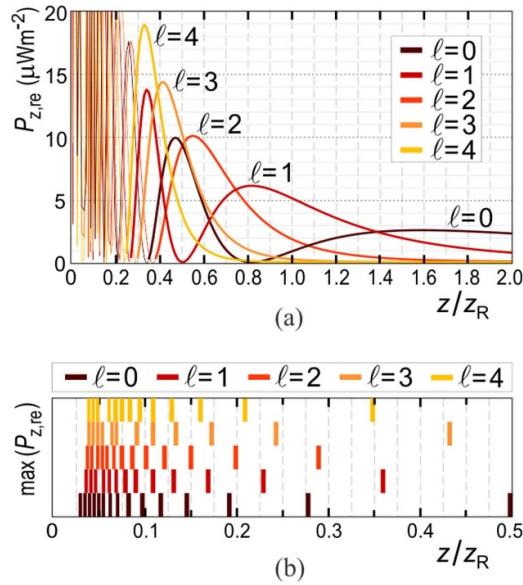
Figure 7. Axial Poynting vector maxima and the optimal receiving distance (link range). Fixed-size receiving UCA $R_{\text{rec}} = R_{\text{a}} = 20\lambda_0$ is assumed. For $z < 0.4z_{\text{R}}$, the axial Poynting vector component oscillates between many minima and maxima. (a) The optimal receiving distance, $z_{\text{L,opt}}$, for each mode is that corresponding to the maxima denoted by $\ell = 1$ to $\ell = 4$. Receiving distance could be somewhat larger than $z_{\text{L,opt}}$, but not without limit, having in mind a rapid decrease of all modes except the $\ell = 0$. (b) Positions of the local P_z maxima above the *x*-axis. Receiving distance adjustment might be needed in this region to avoid local minima of P_z.

taken identically as for the figure 6. We assumed that the transmitting UCA size, $R_{\text{a}} = 20\lambda_0$, and the receiving UCA size, R_{rec}, were both set in advance (here, $R_{\text{rec}} = R_{\text{a}}$). We can observe sharp oscillations between the local minima and maxima for distances very close to the source plane. We note here, that only the transmitting OAM UCA array has been modeled; in practice, when the antenna arrays are positioned close to each other, an additional oscillating behavior with distance should be expected due to a standing wave between the large ground planes of antenna arrays. The reason behind the oscillating behavior of P_z is that not the narrowest ring of EM field maxima is used for reception, but the surrounding local maxima resulting from a single UCA. For simplicity, figure 7(b) shows only the positions of the local maxima above the *x*-axis. In this region, OAM wave transmission is possible, but the distance adjustment aimed at increasing the received power could be useful. The local OAM wave's P_z maxima positioned most far away from the source plane are denoted in figure 7(a) by $\ell = 1$, $\ell = 2$, $\ell = 3$, and $\ell = 4$. In [26], we have analytically estimated the optimal link range based on the spreading cone of EM field maxima, given here as equation (9). The analytically estimated optimal receiving distance, $z_{\text{L,opt}}$, for each mode, matches very well with the P_z maxima positioned most far away from the source plane. Further away from the denoted maxima, the axial Poynting vector component decreases monotonically, tending asymptotically to data shown in figure 6(b) by the solid lines. Therefore, the receiving distance should preferably be set at $z_{\text{L,opt}}$ or somewhat larger distance where the EM fields have not yet decreased too much. In practice, as discussed in [26], a design approach where the desired link range is set first seems promising, as the sizes of the receiving OAM UCA arrays could then be estimated to enable near-optimal EM wave
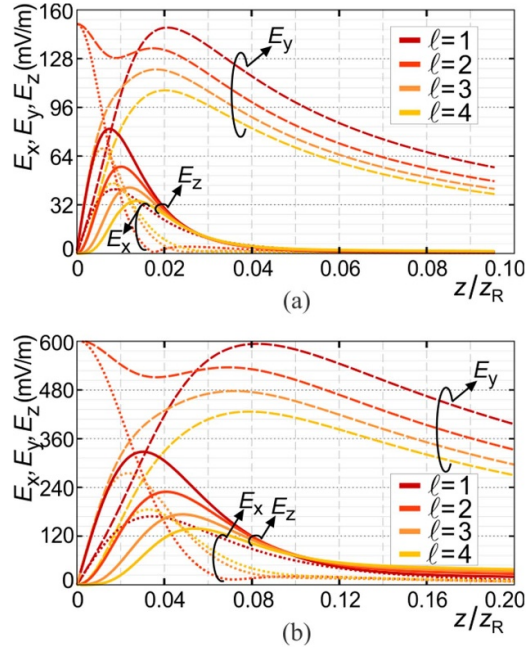
Figure 8. Dependence of the electric field components of the OAM wave, E_x, E_y, and E_z, on distance from the source plane expressed in terms of Rayleigh distance: (a) $R_a = 20\lambda_0$ and (b) $R_a = 5\lambda_0$.

reception at the same link range distance for multiple OAM modes. It should be noted that (9) corresponds to the case of an equally sized transmitting and receiving array, $R_{rec} = R_a$, while in the most general case, we would have to consider separately for each OAM mode [26], that

$$z_{L,opt} = \frac{R_{rec}}{R_a} \frac{2z_R}{(|\ell| + 1)}. \tag{12}$$

3.4. OAM wave pattern formation

Another question that has not been previously addressed is how close to the source plane a proper reception or data transfer of an OAM wave can occur. For instance, if an OAM wave-based radio frequency identification device (RFID) or near-field communication card (NFC) card/tag requires touch or close proximity to a reader, it is necessary to determine whether the EM field superposition at such a distance results in a recognizable OAM wave pattern. To investigate this, we analyzed all three electric field components of the OAM wave, E_x, E_y, and E_z, for distances from the source plane up to $0.2z_R$. Please note that this region corresponds to a sharply oscillating axial Poynting vector, P_z, as shown in figure 7.

The results have been repeated for $N_a = 16$ antennas, being the minimal number that allows a four-mode resolution, as well as $N_a = 64$, an antenna number used in some of the above examples ensuring low side lobes. The results did not differ in the two cases, except that the EM field strengths were scaled by N_a. Figure 8 shows the electric field corresponding to the OAM spreading angles in plane $x = 0$ for modes $\ell = 1$ to $\ell = 4$. Therefore, those are the maximal E_y values in the given observation plane for a particular mode and the corresponding
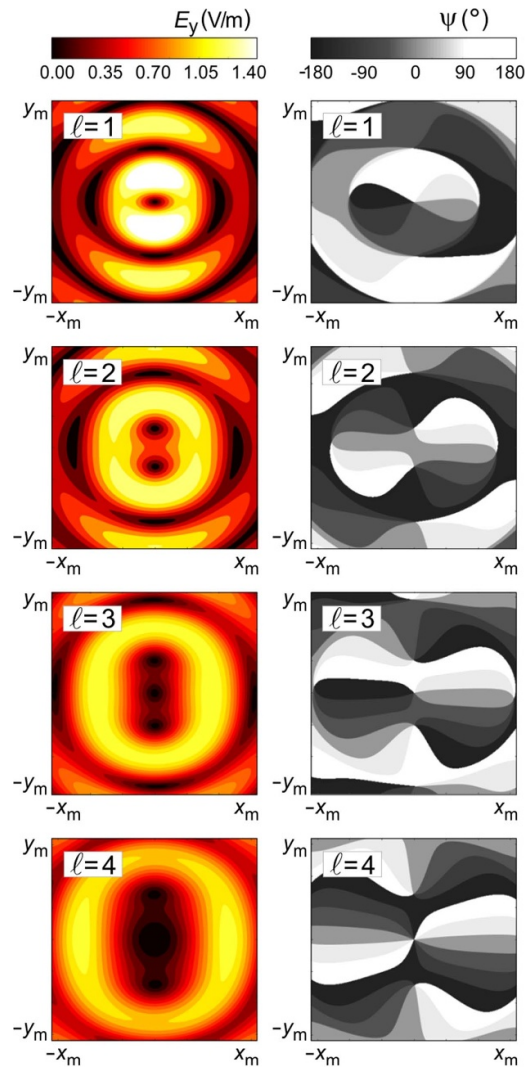
Figure 9. Near-field formation of OAM modes close to the OAM UCA source plane, at $z_L = 0.01 z_R$. The results shown are for $R_a = 20\lambda_0$. (Magnitudes shown in color in online version of the article.).

E_x and E_z.. As mentioned previously in the section 2, we here investigated the wave fronts resulting from linear polarization along the *y*-axis direction of the global coordinate system. Therefore, the E_x and E_z field components diminish with distance, while the E_y component dominates. The antenna array elements of the receiving arrays should not be orthogonal with the *y*-axis direction. If a circular polarization is desired, the crossed dipoles or other antenna type producing circular polarization is used, in which case E_x shown in figure 8 would interfere with the useful E_x component produced by the crossed dipoles. The E_z field component vanishes with the distance in any case, as the beam propagation is close to paraxial along the *z*-axis direction. For $R_a = 20\lambda_0$, the paraxiality of the beams is high with the OAM spreading angles of $0.85°$, $1.40°$, $1.92°$, and $2.44°$, for the first four modes. The E_x and E_z components become negligible at about $0.04 z_R$ (≈ 25 cm in the considered case). However, if a smaller
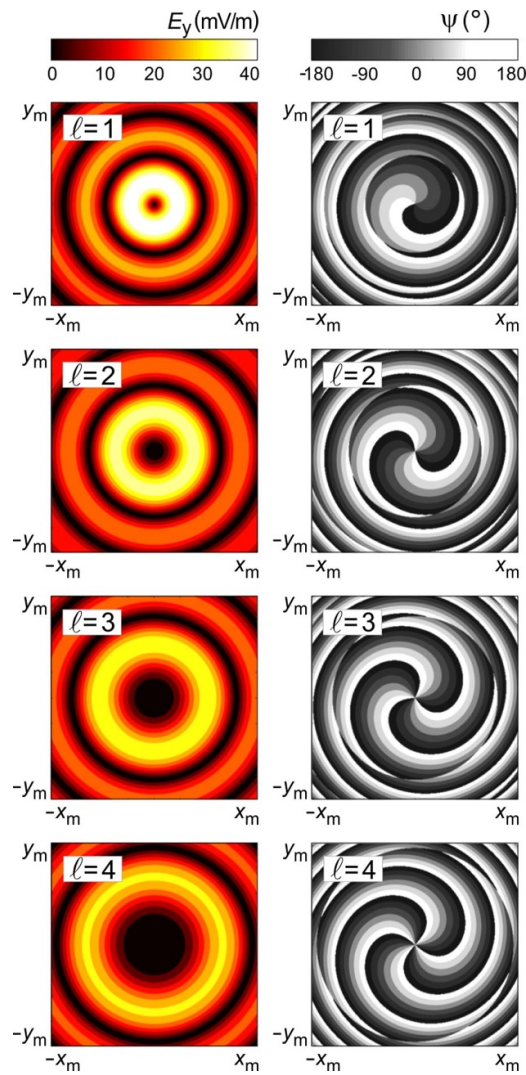
Figure 10. Completely formed OAM mode magnitudes and phases at a distance $z_L = z_R$ from the source. The results are shown for $R_a = 20\lambda_0$. (Magnitudes shown in color in online version of the article.).

source, UCA, is used in a RFID or NFC device, as seems more suitable, the Rayleigh distance is shorter, but the E_x and E_z decrease is also slower. For $R_a = 5\lambda_0$, E_x and E_z can be considered negligible at about $0.2z_R$ (≈ 8 cm). Slower EM field decrease is related to larger OAM beam angles of $3.35°$, $5.57°$, $7.67°$, and $9.72°$.

Finally, it might be interesting to check out on the phase and magnitude of the OAM wave close to the source plane and compare it with a fully formed characteristic OAM wave magnitude and phase. Figure 9 shows the formation of the OAM modes for $R_a = 20\lambda_0$, at a distance of only $0.01z_R$ from the source plane. As can be seen from figure 8, all three EM field components are still pronounced so close to the array. The observed phase distortion vanishes by

$0.04z_R$ and the OAM phase, ψ, gradually increases from $-180°$ to $180°$. The situation is similar for smaller arrays, (e.g. $R_a = 5\lambda_0$). The OAM phase, ψ, at the distance of $0.04z_R$ resembles the one shown in figure 9, for $0.01z_R$. The magnitude and phase for $R_a = 5\lambda_0$ become quite acceptable at about $0.12z_R$ distance ($\approx$5 cm). In any case, near-field formation of OAM waves mandates a distance of about 4–6 cm from the source plane, at 60 GHz, to avoid phase distortions. As opposed to that, both the magnitude and OAM phase at Rayleigh distance are completely formed and look very similar to those obtained by theoretical expressions. Figure 10 shows the magnitude and OAM phase at Rayleigh distance for $R_a = 20\lambda_0$.

4. Conclusions

In line with our expectations, the OAM EM wave modeling based on the infinitesimal (Hertz) dipole method proved highly efficient and versatile in modeling electrically large OAM antenna arrays. We presented a general framework where the infinitesimal dipole method could be combined with full-wave numerical EM modeling in the analysis of arbitrary antenna arrays or other OAM radiating structures. The infinitesimal dipole equations enable exact, yet efficient, modeling of the sub-array positioning in space and its influence on the overall EM fields. The use of numerical EM modeling for the sub-array radiation patterns can take into account the coupling of closely positioned antennas and other effects on the sub-array level. The presented examples consider the simplest possible OAM UCA array consisting of only short dipoles as array elements, as is often used in other works on the use of OAM waves in communications.

Additionally, we have mentioned the possibility to use the proposed method in optimizing the non-uniform as well as non-circular arrangements of the antenna sub-arrays. Such designs might be very useful in practical applications, yet there are some challenges to resolve. Firstly, non-uniform and non-circular antenna arrangements will require antenna phasing optimization, to produce high quality OAM waves. We will be comparing the OAM mode quality of non-circular versus the circular antenna arrangements. Then, complex designs with many elements might not be cost-effective; therefore, a compromise between the OAM mode quality and cost might be necessary. Such investigations will be conducted as a part of our future work.

The developed infinitesimal dipole modeling allowed us to efficiently analyze the short-range EM fields at different frequencies of operation and carry out an in-depth analysis of the effects of array electrical sizes and link distances on the radiation properties. To facilitate the interpretation of results, distances were normalized with respect to the Rayleigh distance estimate. To the best of our knowledge, no such detailed analysis was previously available in the literature.

Data availability statement

All data that support the findings of this study are included within the article (and any supplementary information files).

Acknowledgments

Funding

ORCID iDs

Andjelija Ž Ilić   https://orcid.org/0000-0003-0859-6358
Jelena Z Trajković   https://orcid.org/0000-0002-2246-0097

References

[1] Chen S, Liang Y, Sun S, Kang S, Cheng W and Peng M 2020 Vision, requirements, and technology trend of 6G: how to tackle the challenges of system coverage, capacity, user data-rate and movement speed *IEEE Wirel. Commun.* **27** 218–28
[2] Berry M V 2005 Phase vortex spirals *J. Phys. A: Math. Gen.* **38** L745–51
[3] Berry M V 2013 Curvature of wave streamlines *J. Phys. A: Math. Theor.* **46** 395202
[4] Berry M V and Liu W 2022 No general relation between phase vortices and orbital angular momentum *J. Phys. A: Math. Theor.* **55** 374001
[5] Liu K, Liu H, Qin Y, Cheng Y, Wang S, Li X and Wang H 2016 Generation of OAM beams using phased array in the microwave band *IEEE Trans. Antennas Propag.* **64** 3850–7
[6] Mari E, Spinello F, Oldoni M, Ravanelli R A, Romanato F and Parisi G 2015 Near-field experimental verification of separation of OAM channels *IEEE Antennas Wirel. Propag. Lett.* **14** 556–8
[7] Feng H, Ye L, Zhang Y, Li W, Chen H and Liu Q H 2020 Bidirectional multi-mode microwave vortex beam generation enabled by spoof surface plasmon paritons *Appl. Phys. Lett.* **117** 241601
[8] Mahmouli F E and Walker S D 2013 4-Gbps uncompressed video transmission over a 60-GHz orbital angular momentum wireless channel *IEEE Wirel. Commun. Lett.* **2** 223–6
[9] Yan Y *et al* 2014 High-capacity millimetre-wave communications with orbital angular momentum multiplexing *Nat. Commun.* **5** 4876
[10] Guo Z and Yang G 2017 Radial uniform circular antenna array for dual-mode OAM communication *IEEE Antennas Wirel. Propag. Lett.* **16** 404–7
[11] Xiong X, Zheng S, Zhu Z, Yu X, Jin X and Zhang X 2020 Performance analysis of plane spiral OAM mode-group based MIMO system *IEEE Commun. Lett.* **24** 1414–8
[12] Lee I, Sawant A and Choi E 2021 High-directivity orbital angular momentum antenna for millimeter-wave wireless communications *IEEE Trans. Antennas Propag.* **69** 4189–94
[13] Xu X, Mazzinghi A, Freni A and Hirokawa J 2021 Simultaneous generation of three OAM modes by using a RLSA fed by a waveguide circuit for 60 GHz-band radiative near-field region OAM multiplexing *IEEE Trans. Antennas Propag.* **69** 1249–59
[14] Li J-S and Zhang L-N 2020 Simple terahertz vortex beam generator based on reflective metasurfaces *Opt. Express* **28** 36403
[15] Chang Z, You B, Wu L-S, Tang M, Zhang Y-P and Mao J-F 2016 A reconfigurable graphene reflectarray for generation of vortex THz waves *IEEE Antennas Wirel. Propag. Lett.* **15** 1537–40
[16] Gou P, Kong M, Yang G-M, Guo Z-G, Zhang J, Han X, Xiao J and Yu J 2018 Integration of OAM and WDM in optical wireless system by radial uniform circular array *Opt. Commun.* **424** 159–62
[17] Xie G *et al* 2015 Performance metrics and design considerations for a free-space optical orbital-angular-momentum multiplexed communication link *Optica* **2** 357–65
[18] Lin P-C, Gibson G M and Padgett M J 2022 Real-time visualisation and optimisation of acoustic waves carrying orbital angular momentum *J. Phys. A: Math. Theor.* **55** 264007
[19] Willner A E *et al* 2016 Design challenges and guidelines for freespace optical communication links using orbital-angular-momentum multiplexing of multiple beams *J. Opt.* **18** 074014
[20] Bachmann D, Shatokhin V N and Buchleitner A 2019 Universal entanglement decay of photonic orbital angular momentum qubit states in atmospheric turbulence: an analytical treatment *J. Phys. A: Math. Theor.* **52** 405303
[21] Edfors O and Johansson A J 2012 Is orbital angular momentum (OAM) based radio communication an unexploited area? *IEEE Trans. Antennas Propag.* **60** 1126–31

[22] Nguyen D K, Pascal O, Sokoloff J, Chabory A, Palacin B and Capet N 2015 Antenna gain and link budget for waves carrying orbital angular momentum *Radio Sci.* **50** 1165–75

[23] Craeye C 2016 On the transmittance between OAM antennas *IEEE Trans. Antennas Propag.* **64** 336–9

[24] Morabito A F, di Donato L and Isernia T 2018 Orbital angular momentum antennas: understanding actual possibilities through the aperture antennas theory *IEEE Antennas Propag. Mag.* **60** 59–67

[25] Sawant A, Lee I, Jung B C and Choi E 2021 Ultimate capacity analysis of orbital angular momentum channels *IEEE Wirel. Commun.* **28** 90–96

[26] Ilić A Ž, Vojnović N M, Savić S V, Grass E and Ilić M M Optimized planar printed UCA configurations for OAM waves and the associated OAM mode content at the receiver manuscript under review

[27] Yuan T, Cheng Y, Wang H and Qin Y 2017 Mode characteristics of vortical radio wave generated by circular phased array: theoretical and experimental results *IEEE Trans. Antennas Propag.* **65** 688–95

[28] Balanis C A 1997 *Antenna Theory: Analysis and Design* 2nd edn (New York: Wiley)

[29] Clauzier S, Mikki S M and Antar Y M M 2015 Design of near-field synthesis arrays through global optimization *IEEE Trans. Antennas Propag.* **63** 151–65

[30] Padgett M J, Miatto F M, Lavery M P J, Zeilinger A and Boyd R W 2015 Divergence of an orbital-angular-momentum-carrying beam upon propagation *New J. Phys.* **17** 023011

[31] Kolundzija B and Djordjevic A 2002 *Electromagnetic Modeling of Composite Metallic and Dielectric Structures* (Norwood, MA: Artech House) (available at: www.wipl-d.com/)

[32] Kolundzija B and Sumic D 2008 Electromagnetic simulation of complex and electrically large structures in WIPL-D Pro *IEEE Microw. Mag.* **9** 159–62

[33] Klopf E M, Sekeljic N J, Ilic M M and Notaros B M 2012 Optimal modeling parameters for higher order MoM-SIE and FEM-MoM electromagnetic simulations *IEEE Trans. Antennas Propag.* **60** 2790–801

[34] Vojnović N M, Savić S V, Ilić M M and Ilić A Ž 2020 Performance analysis of low-cost printed antenna array elements for 5G LOS-MIMO arrays at 60 GHz *Wirel. Pers. Commun.* **111** 2641–58

Investigation of the OAM EM wave tissue irradiation at millimeter-wave frequencies

Andjelija Ž. Ilić [a,*], Jelena Z. Trajković [a], Slobodan V. Savić [b], Milan M. Ilić [b]

[a] *Institute of Physics Belgrade, University of Belgrade, Pregrevica 118, 11080, Zemun, Belgrade, Serbia*
[b] *School of Electrical Engineering, University of Belgrade, 11120, Belgrade, Serbia*

ARTICLE INFO

ABSTRACT

Recently, there has been an increase of interest in the use of electromagnetic (EM) waves with helical wavefronts, known as the orbital angular momentum (OAM) waves. Applications in the field of biomedicine have been foreseen, such as medical imaging and diagnosis, deep-tissue imaging, biosensing, and communication with medical implants. Other possible applications include various localized tissue treatments or tissue ablation. The available references mainly study the interaction of OAM light with biological structures, offering some insights into the biophotonics effects, but without the investigation of how to plan tissue exposures or how to estimate the EM field parameters in a particular case of application. We use the previously developed short dipole modeling of OAM EM fields to study the above problems by altering the OAM beam parameters and the distance from the target tissue. The results could guide the design of components and devices based on OAM EM waves.

1. Introduction

Recently, there has been an increase of interest in the use of electromagnetic (EM) waves with helical wavefronts, known as the orbital angular momentum (OAM) waves (Forbes, 2022; Weng and Pan, 2023; Willner et al., 2022). Apart from the proposed use as optical tweezers for manipulating trapped particles (Macdonald et al., 2002), one of the first proposed applications of the OAM EM waves was for free-space optical (FSO) communications with improved data transfer security (Gibson et al., 2004). The emergence of 5G and beyond 5G mobile communications led to the high capacity and high spectral efficiency offered by OAM EM waves to become the main benefit of their use in that field (Wang et al., 2022; Willner et al., 2022). The use of many other frequencies and waves has also been proposed, including acoustic waves for high-rate underwater communications (Lin et al., 2022), radio-frequency waves (Mohammadi et al., 2010), microwaves (Liu et al., 2016; Golubović et al., 2023), millimeter waves (Mahmouli and Walker, 2013; Xu et al., 2021), terahertz waves (Willner et al., 2022), and optical waves (Anguita and Cisternas, 2022; Wang et al., 2022; Zhiyuan et al., 2022).

Additionally, biomedical applications of OAM EM waves have been foreseen: medical imaging and diagnosis, deep-tissue imaging, biosensing, as well as communication with medical implants (Biton et al., 2021; Chen et al., 2017; Perez et al., 2022). Other possible applications include various localized tissue treatments or tissue ablation. The available literature mainly studies the interaction of OAM light with biological structures, offering some novel insights into the biophotonics effects. Given that the OAM EM waves have been successfully generated over a wide span of frequencies, investigation of the OAM EM wave interaction with tissue at different frequencies is of interest. Here we discuss the situation, where it is desired to design applicators to deliver EM energy to a certain area of the tissue surface from some predefined distance (or given a range of distances). In some sense, it is a canonical problem, as tissue irradiation can be aimed at tissue ablation, but also, at somewhat lower frequencies and lower doses it can be a first step in producing a scattered EM wave to be received and analyzed in biomedical imaging.

The proposed study is also important in the context of body area networks utilizing OAM, e.g. currently very popular wearable antennas (Noor et al., 2022). Recently, methods to produce OAM beams at soft or hard X-ray frequencies have been devised; therefore, both ionizing and non-ionizing tissue irradiations with OAM beams are in principle possible. Possibilities for use of these technologies will be discussed in the next section, explaining the OAM EM waves, their properties, and several methods of generating those waves. Subsequently, noting the quite general nature of our expressions and models, the investigation

---

will be steered mainly to the millimeter waves, where a simple single harmonic wave is usually employed. At X-rays, short pulses would have to be used, which would have to be represented by a sum of spectral components. However, the design methods will in all cases be similar to the ones explained here in detail for millimeter wave frequencies.

The rest of the paper is organized as follows. Second section summarizes some OAM EM wave properties and ways of their generation. Third section presents the analysis results for several OAM EM wave modes for a range of irradiated tissue spot sizes, i.e., surface areas where most EM energy is delivered, and a range of distances from the target tissue. The results offer insights into what could be expected in different cases of application. Fourth section considers two design examples of biomedical applicators using the OAM modes. Fifth section concludes the paper with several brief points resulting from the performed analysis.

2. OAM waves and their generation

In the general case, the EM field momentum consists of both the linear momentum and angular momentum component. The angular momentum of the EM field, **J**, is obtained by summing two components: spin angular momentum (**S**) and orbital angular momentum (**L**). It is calculated as (Allen et al., 1992)

$$\mathbf{J} = \varepsilon_0 \int_v \mathbf{r} \times \mathrm{Re}\{\mathbf{E} \times \mathbf{B}^*\}\mathrm{d}v = \mathbf{L} + \mathbf{S}, \tag{1}$$

where the spin angular momentum is calculated as

$$\mathbf{S} = \varepsilon_0 \int_v \mathrm{Re}\{\mathbf{E}^* \times \mathbf{A}\}\mathrm{d}v, \tag{2}$$

and the orbital angular momentum, **L**, is found using

$$\mathbf{L} = \varepsilon_0 \int_v \mathrm{Re}\{j\mathbf{E}^*(\widehat{\mathbf{L}} \bullet \mathbf{A})\}\mathrm{d}v, \widehat{\mathbf{L}} = -j(\mathbf{r} \times \nabla) \tag{3}$$

In the above, **A** denotes the magnetic vector potential, **E** the electric field vector, **B** the magnetic induction, **r** the position vector, * the complex conjugate, and $\widehat{L}$ the auxiliary vector operator used in the OAM calculations, and ε_0 is the free-space permittivity.

It is of interest to explain some ways of generating the OAM waves. Generation of the optical OAM waves is often carried out using spiral phase plates, holograms, and spatial light modulators (Chen et al., 2020). These methods have also been successfully used at millimeter wave frequencies (Mahmouli and Walker, 2013). A summary of OAM generation methods at different frequencies can be found in (Chen et al., 2020). In the microwave and millimeter wave frequency range, many dedicated antenna types have also been developed, including ring-slot traveling-wave antennas (Hui et al., 2015) and twisted parabolic antennas (Mari et al., 2015). The phased UCAs have been used from acoustic (Lin et al., 2022) to optical frequencies (Li et al., 2022), using spatial light modulators to control the phases of concentric UCAs in the optical case. The generation of radiating multi-mode OAM beams from a single aperture has been studied in detail in (Chen et al., 2020). The multi-mode OAM UCA configurations used to generate the OAM fields in this work are shown in Fig. 1.

Recently, generating both soft X-rays carrying the OAM modes (Kong et al., 2017) and hard X-rays with the OAM (Huang and Deng, 2021), has been proposed. These studies open the possibilities of OAM beam use in generating both types of radiation used clinically: ionizing and non-ionizing radiation (Kilicoglu et al., 2023). In (Kong et al., 2017), wave mixing is applied to a tabletop high-harmonic source. The main merit of the proposed approach, where a strong Gaussian infrared laser beam is perturbed by a weak beam carrying the OAM, is in the possibility to place topological charge on high harmonics rather than on the fundamental beam. Therefore, the first-order OAM beams with the
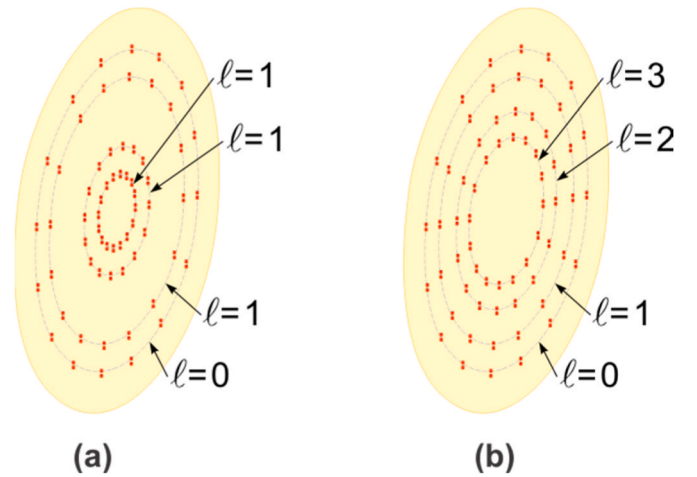

Fig. 1. The multi-mode OAM UCA configurations for producing relatively wide and uniform beam spots at the irradiated tissue surface. The outermost UCA generates the $\ell = 0$ mode, providing the central part of the beam spot at the tissue surface. The outermost UCA radius for the shown arrays equals 7 λ_0, i.e., 35 mm at 60 GHz. The rest of the UCAs use either (a) the same (lowest helical $\ell = 1$) OAM mode, or (b) the combination of different OAM modes. In both cases, larger radius of the UCA producing a mode of a desired mode order, results in a narrower annular region at the irradiated tissue surface.

smallest possible divergence and intensity null in the center were produced at extreme ultraviolet frequencies. In (Huang and Deng, 2021), Bragg mirrors and longitudinal to transverse mode coupling were proposed to enable mode selection in X-ray free-electron laser oscillators (XFELOs). XFELOs are low-gain multipass devices which can produce intense, fully coherent hard X-rays at a high repetition rate. In both soft and hard X-ray cases, high energy pulses at a repetition rate on an order of 1 MHz have been planned. The analysis would thus require the representation of short pulses as a sum of spectral components including the very high frequencies. Noting that technological implementations at different frequencies pose different limitations, e.g., higher losses at microwave and millimeter wave frequencies in comparison to optical ones, the basic properties of OAM EM waves are similar at different frequencies. Planning of the tissue exposure to the OAM beams, or OAM beam applicator design methods, should therefore remain relatively similar. Having that in mind, our analysis will further focus on the millimeter wave frequencies and simple harmonic OAM EM waves, striving to use a general approach to the problem.

Fig. 2 shows the instantaneous OAM fields, i.e., the real part of the electric field y-component, $E_{y,\mathrm{re}}$, produced by the single OAM UCA. These fields are characterized by spiral intensity patterns. The OAM wavefronts rotate about the propagation axis, while advancing in its direction. The simplest form of the OAM EM fields exhibits helical wavefronts with the wave phase varying as shown in the central parts of Fig. 2 (b) plots. In cases, when the entire circular source area is covered by radiating elements, a single annular ring of EM field maximal magnitude is formed in a plane parallel to the source. Away from the main lobe, the OAM EM field intensity drops rapidly. Very similar OAM EM fields in an area close to the propagation axis can be generated by discrete arrangements of source radiating elements, such as the uniform circular antenna arrays (UCA) at microwave and millimeter wave frequencies. For the same annular ring radii on irradiated surfaces, an OAM UCA radius, R_a, is taken approximately as two thirds of what would be a radius of an entire circular source area. Instead of the entire apertures, discrete radiating elements (antennas) facilitate generating multiple OAM modes through a single source aperture. However, spatial discretization of the OAM wave sources, with antenna spacing significantly larger than a wavelength, results in multiple annular rings in the EM field magnitude distributions, indicating the presence of higher radial
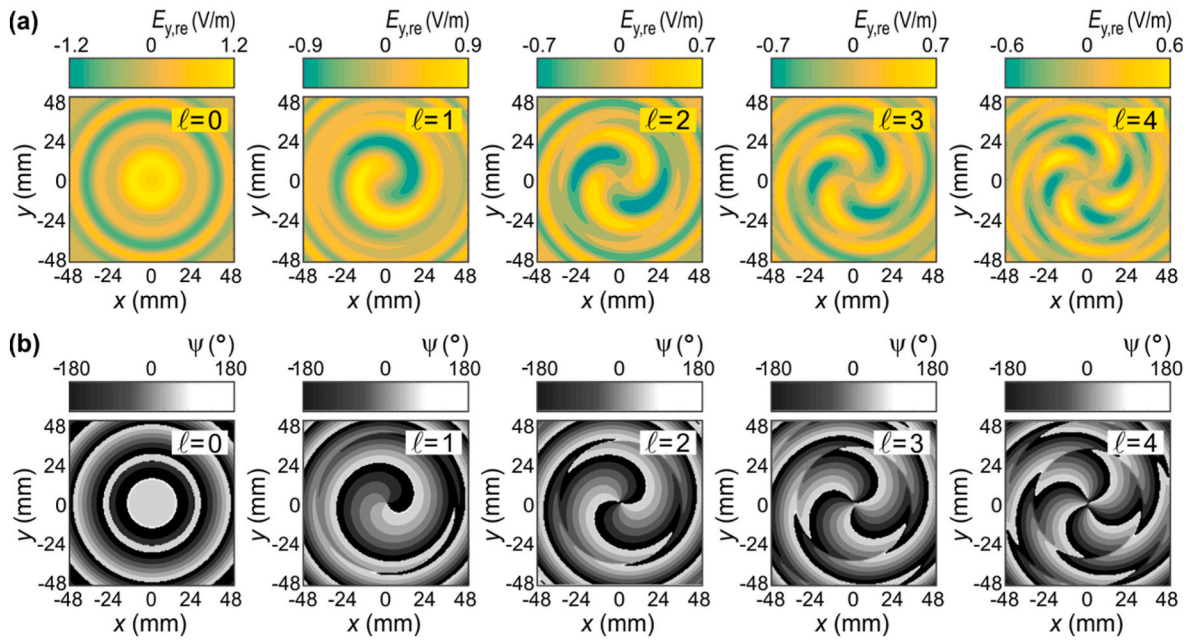
Fig. 2. The OAM EM wave consists of the OAM modes which rotate about the propagation axis, while advancing in its direction. The OAM modes are sometimes denoted as vortex waves. (a) In the planes perpendicular to the propagation axis (xOy planes, here), the instantaneous EM fields, $E_{y,re}$, are characterized by spiral intensity patterns. The number of the spiral arms equals the mode number, ℓ. (b) The EM wave phase of the ℓ-th OAM mode, denoted by ψ, exhibits a phase change from zero to $2\pi\ell$ for one revolution in the xOy planes, around the propagation axis, z.

order OAM modes (Zhao et al., 2017; Ilić et al., 2019). Therefore, as shown in Fig. 3, there are multiple maxima of the OAM EM wave complex magnitudes. OAM modes of higher azimuthal order, ℓ, have narrower maxima, more densely positioned to each other in comparison with the lower-order modes. Also, OAM modes of higher azimuthal order, ℓ, have deeper and more sharp zeros at the propagation axis (z-axis). Namely, the OAM modes can be represented by an expansion in terms of Bessel functions of the first kind (Yuan et al., 2017). Accordingly, the field power reduction at larger distances, z, follows the $z^{-2(|\ell|+1)}$ dependence along the z-axis. However, we have shown that the OAM mode maxima other than the central ones ($\ell = 0$ mode) can be partially suppressed by using three to four closely positioned concentric OAM UCA (Ilić et al., 2019). The field power decrease along the z-axis can be avoided by properly sizing the source, in short-range application scenarios, to obtain the desired positions of OAM mode maxima in the observation plane (at the tissue surface).

The relation between the OAM source size and the position of an ℓ-th OAM mode maximum at the tissue surface can be estimated as (Ilić et al., 2023)

$$R_a \bullet R_{ss} = \frac{\lambda_0(|\ell|+1)z_{ts}}{2\pi} \tag{4}$$

In the above, R_a denotes an OAM UCA radius, R_{ss} denotes a radius corresponding to a maximum of an ℓ-th OAM mode at the tissue surface, λ_0 the free-space wavelength corresponding to the central frequency of operation, and z_{ts} the distance of a biomedical applicator from the target tissue surface. This expression took in the account different vortex spreading angles, θ_v, for different OAM modes. The angle θ_v is measured from the positive z-axis, as in other works on paraxial beams. It can be approximated as

$$\theta_v \approx \frac{\lambda_0(|\ell|+1)}{2\pi R_a} \tag{5}$$

We have recently developed a general method for the analysis of UCA-generated OAM EM waves. Based on short (Hertz) dipole modeling, it is computationally efficient for large antenna arrays and many calculations, such as thorough parametric studies (Ilić et al., 2023). The advantage of the method in comparison with other works in literature is in the very precise modelling of the position vectors from the field points to the observation points, allowing precise short-range calculations, its efficiency, and the possibility to combine it with the numerical calculations for even better results. Main limitations of the methodology are linked to the low losses assumption of the Hertz dipoles, resulting in the upper limit or the best-case scenario of what can be expected for the OAM fields in studied cases. In practice, atmospheric
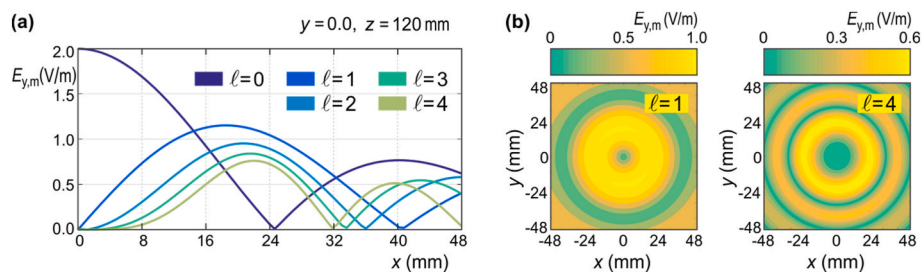

Fig. 3. The OAM EM wave complex magnitudes, $E_{y,m}$, have annular magnitude patterns in the xOy planes. (a) Comparison of OAM field magnitudes above the x-axis for the desired annular ring radius of about $R_{ss} = 20.0$ mm at a distance $z = 120.0$ mm from the source, OAM UCA, plane. (b) Examples of OAM field magnitudes in the xOy plane. Higher order OAM modes have narrower maxima which are more densely positioned to each other in comparison with the lower order modes.

absorption depends on frequency, making certain frequencies more suitable for wireless transmission. Additionally, different technological implementations in various bands result in lower or higher losses due to feeding structures, OAM wave generation methods, and other factors, which depend on the materials used and specific design details. Please refer to (Ilić et al., 2023) for more detailed description and equations. Here, we employed short dipole modeling to accurately represent the OAM modes, shown in Figs. 2 and 3, as well as to study the energy delivered to the tissue surface for different sets of OAM wave and irradiation setup parameters. When generating Figs. 2 and 3, we decided to represent the OAM EM field patterns for the first several OAM modes, for identical radii of OAM mode maxima at the tissue surface, rather than the same size of the OAM UCA producing these modes. We believe that such a choice of system sizing allows a more meaningful comparison of the OAM field patterns, as well as the complex magnitude plots shown in Fig. 3 (a). We set the source UCA radii to obtain the $R_{ss} = 20$ mm, at a distance $z_{ts} = 120$ mm, and defined an irradiated tissue spot size as $D_{ss} = 2 R_{ss}$. The identical spot sizes required different sizes of the source UCA, which were obtained from (4) as $1.910 \lambda_0$, $2.864 \lambda_0$, $3.820 \lambda_0$, and $4.774 \lambda_0$, for $\ell = 1$ to $\ell = 4$, respectively, at 60 GHz. The corresponding free-space wavelength, λ_0, equals 5 mm. For $\ell = 0$, the complex magnitude is always maximal at the z-axis. As a reference, in this section as well as in Section 3, for $\ell = 0$ we used the same source UCA radius as the one producing $R_{ss} = 20$ mm for $\ell = 1$. In all cases shown in Figs. 2 and 3, UCA consisted of 32 short dipoles, $0.04 \lambda_0$ long, excited uniformly by the current having rms value of 1 mA. For different OAM modes, UCA elements are differently phased, according to

$$I_n = I_0 e^{j(\varphi_0 + \ell \varphi_n)} = I_0 e^{j(\varphi_0 + 2\pi \ell n/N_a)} \quad (6)$$

where n is the ordering number of a UCA element. The number of UCA elements, N_a, limits the number of achievable OAM modes to $|\ell_{max}| = \frac{1}{2}(N_a - 1)$, as EM source fields are defined in a finite number of points. As can be seen from Fig. 3 (a), the positions of OAM mode maxima obtained in this way are somewhat approximate and could be further fine-tuned by optimization. For the first part of this study, that is not critical, as the level of EM fields complex magnitude does not vary too much close to the maxima.

3. EM energy delivered to the tissue

In biomedical applications, one of the main questions of interest is the amount of EM energy which can be delivered to the tissue surface. Therefore, we need an assessment of the complex magnitude of the Poynting vector component perpendicular to the tissue surface, i.e., in the direction of z-axis, which directly gives us the EM power flux through the tissue surface. Another important objective is to define ways of designing biomedical applicators, or choosing certain parameters, which would result in enabling the desired irradiation of tissue. In this section, basic analysis results will be presented first. We focus on two frequencies, which were designated to be widely used in millimeter-wave applications, 28 GHz and 60 GHz. The free-space wavelength corresponding to the central frequency of operation equals $\lambda_0 = 10.7$ mm at 28 GHz, and $\lambda_0 = 5.0$ mm at 60 GHz. It has been demonstrated, in our previous work (Ilić et al., 2023; Ilić et al., 2023; Golubović et al., 2023), as well as the work of other groups (Gil et al., 2021; Yagi et al., 2022), that the most benefit of the OAM EM fields could be gained in short-range applications. Functioning of the OAM-based systems was optimal up to the Rayleigh distance and for somewhat larger distances, but still close to the Rayleigh distance. The wavelength, λ_0, defines the Rayleigh distance, z_R, for a given source size. For the OAM UCA of a radius R_a, it can be approximated as

$$z_R = \pi R_a^2 / \lambda_0 \quad (7)$$

For example, $R_a = 30$ mm corresponds to $z_R = 264$ mm at 28 GHz, and $z_R = 565$ mm at 60 GHz, respectively. Biomedical applications often

use such short-range distances; therefore, the electric field strength and mode quality of the OAM modes could be adequate for the planned applications. We have also previously shown (Ilić et al., 2023), that the OAM EM field pattern formation might not be very good if the source and target surface are placed too close. For that reason, extremely short distances to the tissue, taking into account the electrical size of an OAM field source, are not recommendable.

To assess what could be expected from the use of OAM modes in certain application cases, we consider the above two frequencies and a range of distances of a UCA from the tissue surface. We consider distances, z_{ts}, from 80 mm to 280 mm, with a step of 4 mm, in a parametric study of the EM power flux in the z-axis direction for the first several modes. Without the loss of generality, the results in this study were obtained with the linearly polarized electric field of the short dipoles, in the y-direction, E_y, situated in the free space without other objects. We note that circular polarization can be easily produced by two perpendicular linearly polarized and phase shifted fields, e.g. by the use of crossed dipoles.

However, the here presented OAM modes analysis does not depend, in any way, on the choice of EM field polarization. In all analyses, the OAM UCA consisted of 16 short dipoles, 0.2 mm long, which is $0.04 \lambda_0$ at 60 GHz, and about $0.02 \lambda_0$ at 28 GHz. The dipoles were set, in all calculations, as excited by the 1 mA uniform rms input current. The Poynting vector has annular magnitude patterns in planes parallel to the xOy plane, similar as the OAM EM wave complex magnitudes. However, when considering multiple OAM modes, which are mutually orthogonal, one should be adding the z-components of the Poynting vector. The angle of the Poynting vector while precessing about the propagation axis differs for different modes, and the wavefronts are under different angles for different modes. Complex magnitudes of the Poynting vector, $P_{z,m}$, have been used and presented as results throughout this work. In order to somehow define the irradiated tissue spot size, we have defined it as a radius corresponding to the maximal $P_{z,m}$ at a given surface, noting that annular regions are being exposed. Figs. 4 and 5 show the required source OAM UCA radii to obtain the desired spot sizes at considered distances from the tissue, as well as the resulting z-components of the Poynting vector at the tissue surface. The results are given for the first several OAM modes for 28 GHz in Fig. 4 and for 60 GHz in Fig. 5, respectively. In both figures, the so defined spot size ranged from 12 mm to 52 mm with a calculation step of 0.8 mm, while the applicator distance from the tissue varied from 80 mm to 280 mm. The results were obtained for the single OAM UCA case. Since the EM field modeling required an input of the UCA radius, we used equation (4) to estimate the UCA radii for various distance – spot size combinations (shown in upper parts of the plots, denoted as (a), of Figs. 4 and 5). The source size (UCA radius) is proportional to wavelength, distance, and mode number increased by one, and inversely proportional to the desired spot size. The mode $\ell = 0$ has its maximal $P_{z,m}$ at the propagation axis and equation (4) is not applicable to this mode. For this mode, we take the same source UCA radius as the one producing the spot size of 40 mm for $\ell = 1$, at a given distance. The data for $\ell = 0$ were used as a reference. We can clearly notice, from the parts (a) of Figs. 4 and 5, that larger radii R_a are needed for larger distances and to produce the smaller spot sizes. We also observe, from parts (b) of Figs. 4 and 5, that the obtained Poynting vector mainly depends on the distance. However, it can be seen that at 28 GHz it is more difficult to produce small spot sizes than at the 60 GHz. Also, the power flux carried by the OAM modes is lower than that for the $\ell = 0$ case, requiring the appropriate scaling of input currents. Figs. 4 and 5, therefore, present the ranges of Poynting vectors which can be obtained from the OAM-based biomedical applicators, under usual conditions.

Finally, the same $P_{z,m}$ data is shown in Fig. 6 as normalized by the $P_{z,m}$ corresponding to $\ell = 0$, for the same considered distance and expressed in percents. In this way, we are able to critically compare the possibilities of obtaining the desired spot sizes at different distances
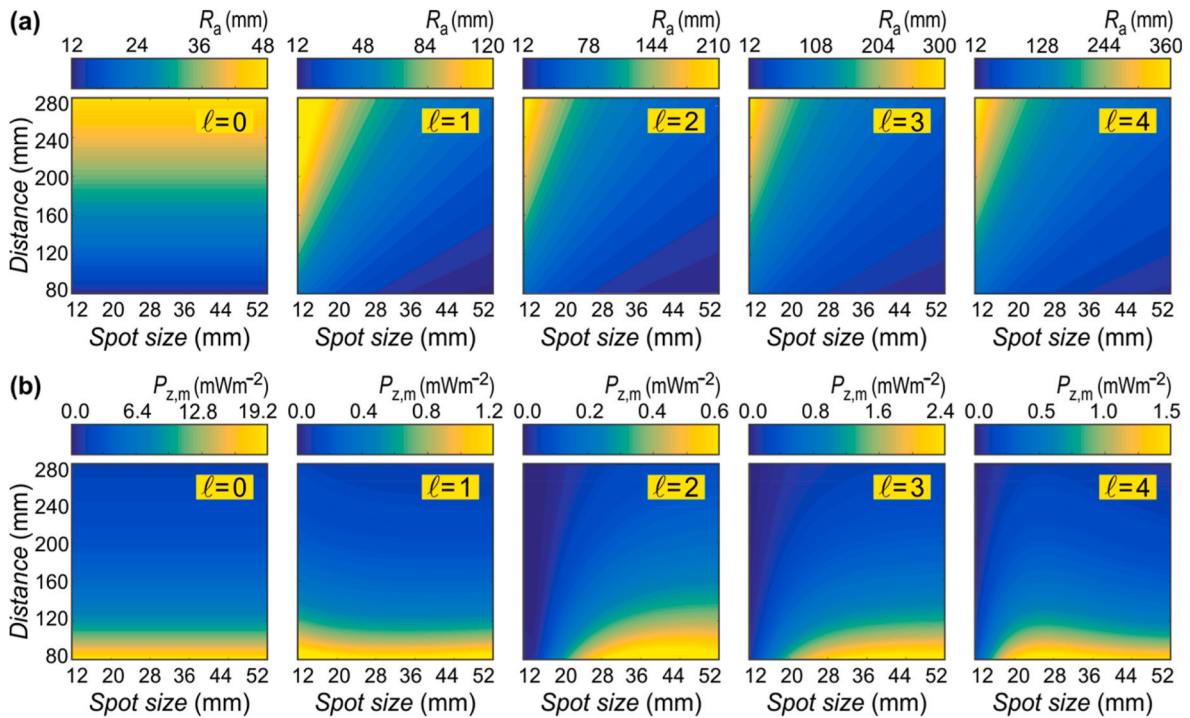
Fig. 4. The required OAM UCA radii, R_a, and the resulting z-components of the Poynting vector, $P_{z,m}$, for the first several OAM modes at 28 GHz. (a) The required R_a to obtain the desired spot size, R_{ss}, at a distance, z_{ts}, from the OAM UCA to the tissue surface. (b) The dependence of the Poynting vector component delivered on the tissue surface, $P_{z,m}$, on two main parameters of interest – the desired spot size and the distance of an applicator from the tissue surface.
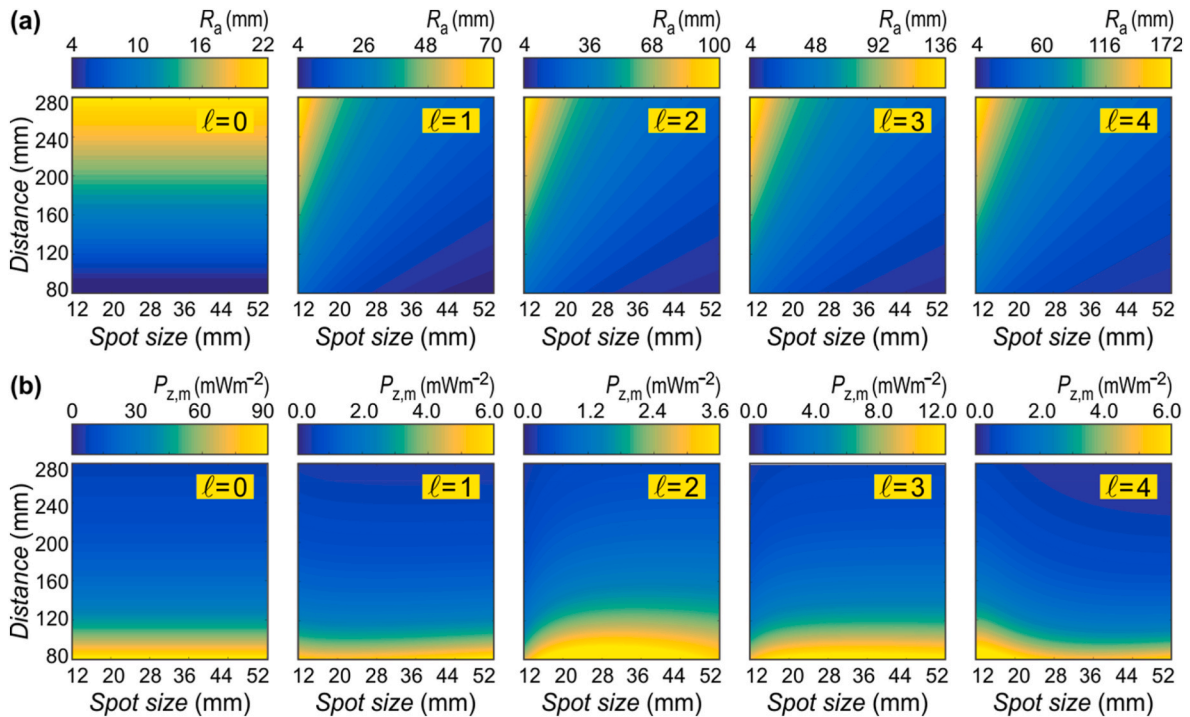

Fig. 5. The required OAM UCA radii, R_a, and the resulting z-components of the Poynting vector, $P_{z,m}$, for the first several OAM modes at 60 GHz. (a) The required R_a to obtain the desired spot size, R_{ss}, at a distance, z_{ts}, from the OAM UCA to the tissue surface. (b) The dependence of the Poynting vector component delivered on the tissue surface, $P_{z,m}$, on two main parameters of interest – the desired spot size and the distance of an applicator from the tissue surface.

from the source. We confirmed that obtaining smaller spot sizes at 28 GHz is challenging for higher-order OAM modes. We can now also clearly notice, that for the larger spot sizes, for $\ell = 1$, the OAM fields decrease faster than that for $\ell = 0$.

4. Design of OAM beam applicators

Using the insights on the OAM EM wave behavior, we designed two example biomedical applicators for OAM beams. To obtain filled rather
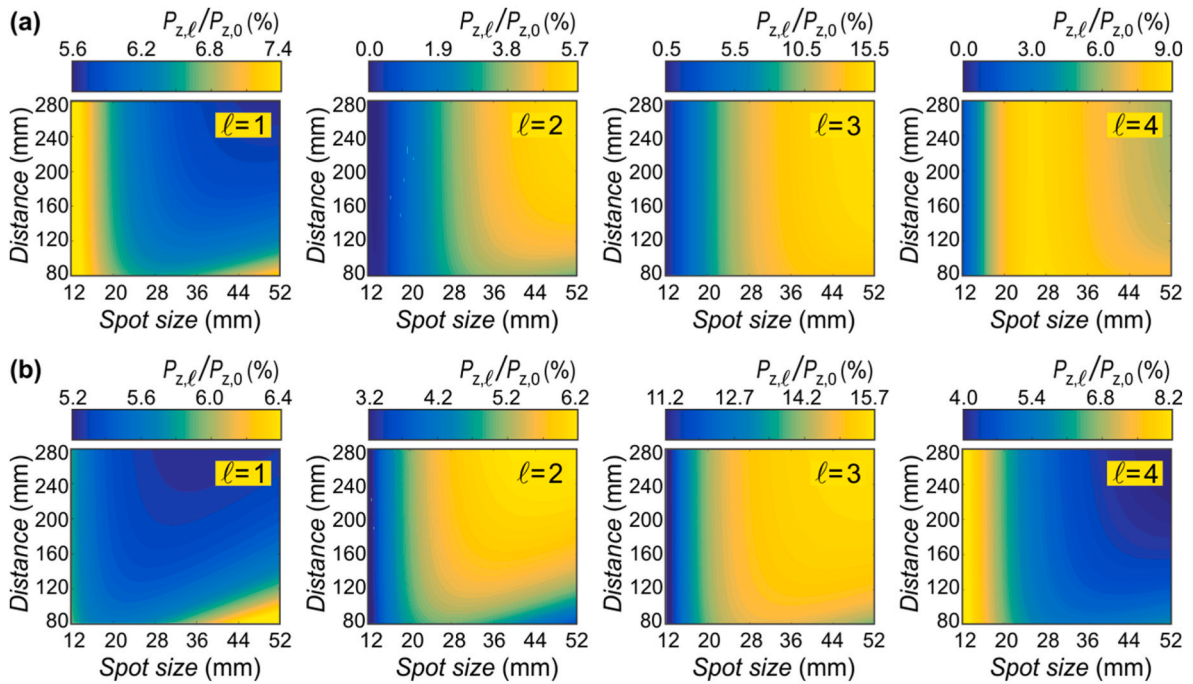
Fig. 6. The complex magnitudes of Poynting vector component in the direction of propagation axis, $P_{z,m}$, for the first four OAM modes, normalized with respect to the EM field corresponding to $\ell = 0$ for the considered distance (shown in %). (a) Frequency of operation: 28 GHz. (b) Frequency of operation: 60 GHz.

than annular regions of the irradiated tissue, both examples use the $\ell = 0$ EM fields to provide radiation in the central parts of areas of interest. The applicator designs, shown in Figs. 7 and 8, use the same $\ell = 1$ OAM mode and the combination of different OAM modes, respectively. The frequency of operation for all shown examples was taken as 60 GHz. We set the desired distance of biomedical OAM beam applicators from the tissue surface at $z_{ts} = 120$ mm. Several irradiated tissue spot sizes, $D_{ss} = 2\,R_{ss}$, were considered. Firstly, a relatively narrow but highly uniform beam spot can be obtained by surrounding the $\ell = 0$ EM power flux maximum by a single annular region corresponding to $\ell = 1$. We set $R_{a,0} = 7.0\lambda_0$, $R_{a,1} = 5.8\lambda_0$, and scale the input currents to 1.0 mA and 1.7 mA to produce the $P_{z,m}$ shown in Fig. 7 (a) by the thick dashed blue line, while the individual contributions from OAM UCA are shown by the solid lines (dark blue and blue). The Poynting vector for this case is also shown in Fig. 7 (c). We aimed to place the first maximum of the $\ell = 1$ mode (blue line in Fig. 7 (a)) at the location of the first zero of $\ell = 0$. The required source UCA radius, $R_{a,1}$, was adjusted based on Eq. (4). As a result, a significantly wider flattop maximum was obtained in comparison with the $\ell = 0$ only. To attain even wider flattop maxima, one would need to take smaller UCA radii, both $R_{a,0}$ and $R_{a,1}$, which in turn would result in wider both central maximum and the annular pattern corresponding to the $\ell = 1$ mode. We further add two UCA, at $R_{a,2} = 2.8\lambda_0$ and $R_{a,3} = 1.6\lambda_0$, set their currents to 1.1 mA and 1.2 mA, respectively, and downscale the current of $R_{a,1}$ to 1.3 mA to obtain the sum of all Poynting vector z-components shown by the thick green line in Fig. 7 (b), and in Fig. 7 (d). This final design corresponds to the arrangement of UCAs shown in Fig. 1 (a). One could use modes $\ell = 0$ and $\ell = 2$, instead of the above ones; however, that would somewhat increase the applicator size due to the larger required source UCA size.

Another possibility, for the applicator design, is to use the combination of different OAM modes in an arbitrary ordering. Here, we wanted to start the design with the same two positions of $R_{a,0}$ and $R_{a,1}$, for $\ell = 0$ and $\ell = 1$. That somewhat limited the possibilities, since the overlapping of UCA was avoided, to the ordering shown in Fig. 8 (a). The innermost two UCA were set as $R_{a,2} = 4.3\lambda_0$ and $R_{a,3} = 3.2\lambda_0$. The input currents for the first, second, and third OAM mode were set as 1.6 mA, 1.8 mA, and 1.8 mA, respectively. The described UCAs arrangement is

shown in Fig. 1 (b). The resulting $P_{z,m}$ is shown by the thick dashed lines in Fig. 8 (a) and Fig. 8 (b), and also in Fig. 8 (c) and 8 (d), when three or four UCA were used, respectively. In any case, wider beam spots can be attained by using additional UCAs, and performing the optimization of UCA positions and input currents.

5. Conclusions

In this work, we have utilized the previously developed short dipole OAM UCA modeling to study the possibilities of using the OAM beams for tissue irradiation. The study is also of relevance to other biomedical applications of OAM EM waves in short-range scenarios, such as sensing, imaging, and wearable antenna applications. The main results are the estimates of the Poynting vector component in the propagation direction, giving the power flux delivered to the tissue surface area of interest, and the design examples demonstrating the possibilities to combine multiple UCA, generating the same or the different OAM modes, for achieving more uniform distribution of EM energy on the tissue surface. The obtained insights into the OAM EM wave properties should be guiding the design of biomedical components and devices based on OAM EM waves.

CRediT authorship contribution statement

Andjelija Ž. Ilić: Writing – review & editing, Writing – original draft, Visualization, Validation, Resources, Project administration, Methodology, Investigation, Formal analysis, Data curation, Conceptualization. **Jelena Z. Trajković:** Writing – original draft, Visualization, Investigation, Formal analysis, Data curation. **Slobodan V. Savić:** Writing – original draft, Validation, Methodology, Investigation, Formal analysis. **Milan M. Ilić:** Writing – review & editing, Validation, Project administration, Methodology, Investigation, Conceptualization.
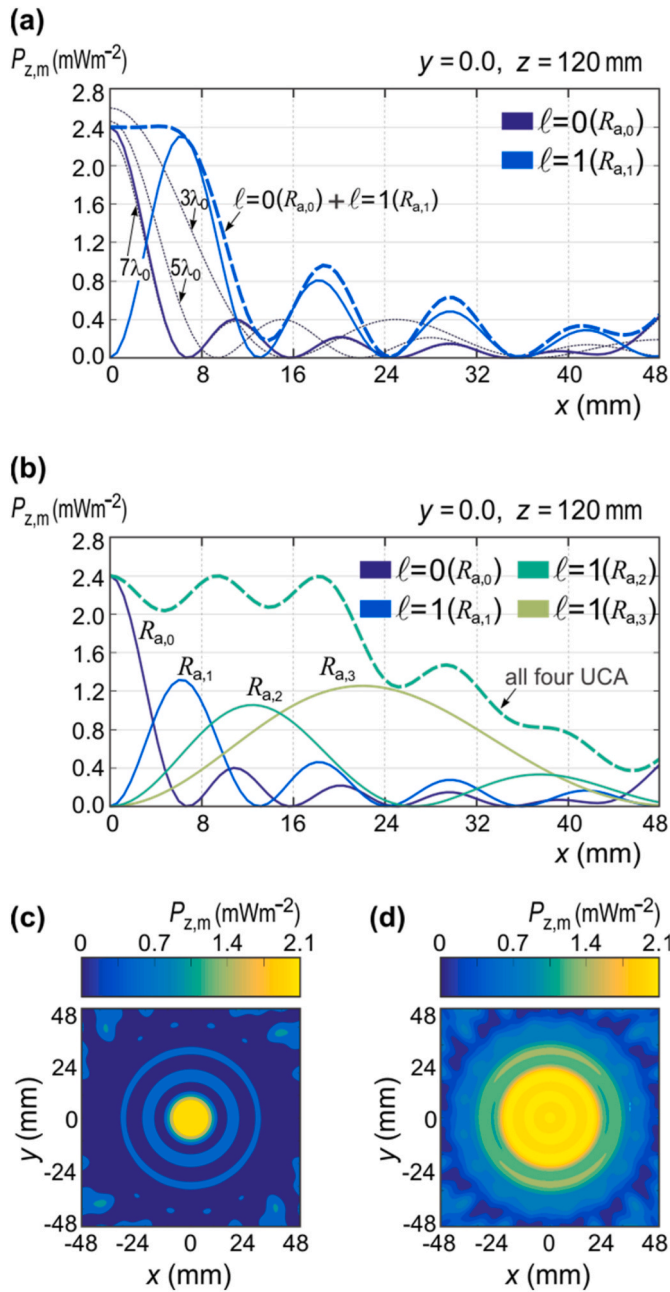
Fig. 7. The OAM beam biomedical applicator design example using only the modes $\ell = 0$ and $\ell = 1$. (a) The $\ell = 0$ EM field profiles, for the UCA radii of 3 λ_0, 5 λ_0, and 7 λ_0, are shown by the thin dark blue lines. The here chosen UCA radius of $R_{a,0} = 7\,\lambda_0$ is shown by the thicker dark blue line. The first maximum of the $\ell = 1$ mode (blue line) is produced by the UCA of a radius $R_{a,1}$, and placed to coincide with the first zero of $\ell = 0$. The resulting power flux profile in the z-direction is shown by the very thick dashed blue line. (b) Two more UCA of radii $R_{a,2}$ and $R_{a,3}$ can be adjusted to produce the first $\ell = 1$ mode maxima at the locations of consecutive zeros of the power flux profile. In that case, the input currents of the $R_{a,1}$ UCA were scaled down as shown by the solid blue line, and the input currents of UCA at $R_{a,2}$ and $R_{a,3}$ were properly scaled to give the resultant power flux profile shown by the very thick dashed green line. (c) The flattop maximum of $P_{z,m}$ produced by UCAs at $R_{a,0} = 7\,\lambda_0$ and $R_{a,1}$ (very thick blue line). (d) Relatively uniform, with ripples, $P_{z,m}$, shown by the very thick green line, produced by four UCA.
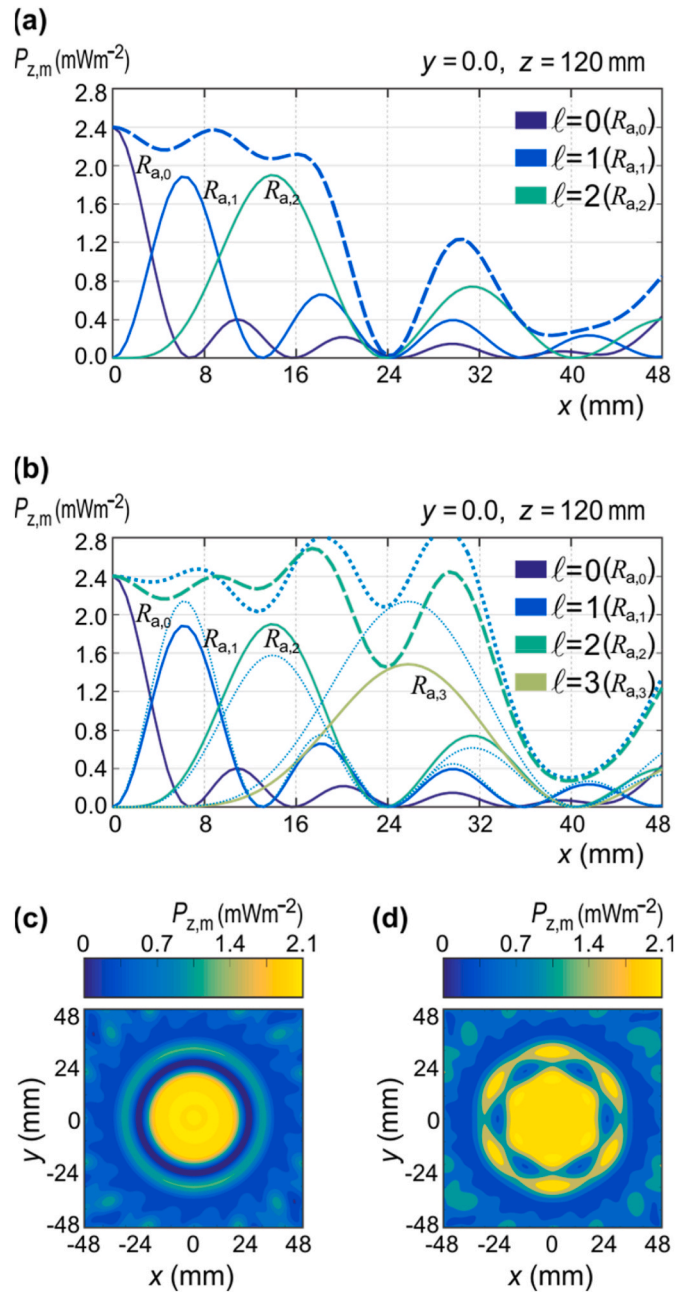
Fig. 8. The OAM beam biomedical applicator design example using a combination of different OAM modes. (a) The UCA of radii $R_{a,0}$, $R_{a,1}$, and $R_{a,2}$, were designed to produce the modes $\ell = 0$, $\ell = 1$, and $\ell = 2$ respectively. Using only the modes $\ell = 0$, $\ell = 1$, and $\ell = 2$, the power flux profile shown by the very thick dashed blue line is obtained. (b) By using all four UCA, with the one of radius $R_{a,3}$ producing the $\ell = 3$ mode, the power flux profile shown by the thick dashed green line is obtained. By a slight adjustment of UCA input currents (mode scaling shown by the thin dotted lines), a deep minimum at $x = 24$ mm can be slightly improved (thick dotted line). (c) The $P_{z,m}$, obtained by using the outermost three UCA (very thick dashed blue line). (d) The $P_{z,m}$, obtained when the fourth, innermost, UCA is added to the previous three UCA (very thick dashed green line).

Declaration of competing interest

The authors declare that they have no known competing financial interests or personal relationships that could have appeared to influence the work reported in this paper.

Data availability

Data will be made available on request.

Acknowledgements

References

Allen, L., Beijersbergen, M.W., Spreeuw, R.J.C., Woerdman, J.P., 1992. Orbital angular momentum of light and the transfor-mation of Laguerre-Gaussian laser modes. Phys. Rev. 45 (11), 8185–8189. https://doi.org/10.1103/physreva.45.8185.

Anguita, J.A., Cisternas, J.E., 2022. Algorithmic decoding of dense OAM signal constellations for optical communications in turbulence. Opt Express 30 (8), 13540–13555. https://doi.org/10.1364/OE.455425.

Biton, N., Kupferman, J., Arnon, S., 2021. OAM light propagation through tissue. Sci. Rep. 11, 2407. https://doi.org/10.1038/s41598-021-82033-6.

Chen, M., Yu, L., Zhang, Y., 2017. Signal/noise ratio of orbital angular momentum modes for a partially coherent modified Bessel-correlated beam in a biological tissue. J. Opt. Soc. Am. A 34 (11), 2046–2051. https://doi.org/10.1364/JOSAA.34.002046.

Chen, R., Zhou, H., Moretti, M., Wang, X., Li, J., 2020a. Orbital angular momentum waves: generation, detection, and emerging applications. IEEE Commun. Surveys Tutorials 22 (2), 840–868. https://doi.org/10.1109/COMST.2019.2952453.

Chen, R., Long, W.-X., Wang, X., Li, J., 2020b. Multi-mode OAM radio waves: generation, angle of arrival estimation and reception with UCAs. IEEE Trans. Wireless Commun. 19 (10), 6932–6947. https://doi.org/10.1109/TWC.2020.3007026.

Forbes, A., 2022. Perspectives on the orbital angular momentum of light. J. Opt. 24 (12), 124005 https://doi.org/10.1088/2040-8986/aca109, 5.

Gibson, G., Courtial, J., Padgett, M.J., Vasnetsov, M., Pas'ko, V., Barnett, S.M., Franke-Arnold, S., 2004. Opt Express 12 (22), 5448–5456. https://doi.org/10.1364/OPEX.12.005448.

Gil, G.-T., Lee, J.Y., Kim, H., Cho, D.-H., 2021. Comparison of UCA-OAM and UCA-MIMO systems for sub-THz band Line-of-Sight spatial multiplexing transmission. J. Commun. Netw. 23 (2), 83–90. https://doi.org/10.23919/JCN.2021.000013.

Golubović, A.Z., Savić, S.V., Ilić, A.Ž., Ilić, M.M., 2023. Short-range transmission using OAM-carrying waves generated by uniform circular arrays. Int. J. Electron. Commun. 165, 154643 https://doi.org/10.1016/j.aeue.2023.154643 (9 pp).

Huang, N., Deng, H., 2021. Generating X-rays with orbital angular momentum in a free-electron laser oscillator. Optica 8 (7), 1020–1023. https://doi.org/10.1364/OPTICA.428341.

Hui, X., Zheng, S., Chen, Y., Hu, Y., Jin, X., Chi, H., Zhang, X., 2015. Multiplexed millimeter wave communication with dual orbital angular momentum (OAM) mode antennas. Sci. Rep. 5, 10148 https://doi.org/10.1038/srep10148.

Ilić, A.Ž., Trajković, J.Z., Savić, S.V., Ilić, M.M., 2023a. Near-field formation of the UCA-based OAM EM fields and short-range EM power flux profiles. J. Phys. Math. Theor. 56, 255701 https://doi.org/10.1088/1751-8121/acd5bf.

Ilić, A.Ž., Vojnović, N.M., Savić, S.V., Grass, E., Ilić, M.M., 2023b. Optimized planar printed UCA configurations on OAM waves and the associated OAM mode content at the receiver. Int. J. Commun. Syst. 36, e5623 https://doi.org/10.1002/dac.5623.

Ilić, A.Ž., Vojnović, N.M., Savić, S.V., Maletić, N., Grass, E., Ilić, M.M., 2019. Performance assessment for OAM antenna arrays. In: 2019 IEEE-APS Topical Conf.

Antennas Propag. Wirel. Comm. APWC, Granada, Spain, pp. 171–173. https://doi.org/10.1109/APWC.2019.8870549, 2019.

Kilicoglu, O., Sayyed, M.I., Kara, U., Aladag, H.I., Karadem, K.B., 2023. Ionized and non-ionized radiation effects on coronary stent implantation. Appl. Radiat. Isot. 192, 110600 https://doi.org/10.1016/j.apradiso.2022.110600.

Kong, F., Zhang, C., Bouchard, F., Li, Z., Brown, G.G., Ko, D.H., Hammond, T.J., Arissian, L., Boyd, R.W., Karimi, E., Corkum, P.B., 2017. Controlling the orbital angular momentum of high harmonic vortices. Nat. Commun. 8, 14970 https://doi.org/10.1038/ncomms14970.

Li, S., Liu, Y., Tao, R., Chen, J., Yang, Y., 2022. Programmable multi-beam steering with optical phased array. In: Proc. SPIE 12166, 7th Asia Pacific Conf. Optics Manufacture (APCOM/YSAOM 2021, 1216635. https://doi.org/10.1117/12.2616205.

Lin, P.-C., Gibson, G.M., Padgett, M.J., 2022. Real-time visualisation and optimisation of acoustic waves carrying orbital angular momentum. J. Phys. Math. Theor. 55, 264007 https://doi.org/10.1088/1751-8121/ac717f.

Liu, K., Liu, H., Qin, Y., Cheng, Y., Wang, S., Li, X., Wang, H., 2016. Generation of OAM beams using phased array in the microwave band. IEEE Trans. Antenn. Propag. 64 (9), 3850–3857. https://doi.org/10.1109/TAP.2016.2589960.

Macdonald, M.P., Paterson, L., Volke-Sepúlveda, K., Arlt, J., Sibbett, W., Dholakia, K., 2002. Creation and manipulation of three-dimensional optically trapped structures. Science 296 (5570), 1101–1103. https://doi.org/10.1126/science.1069571.

Mahmouli, F.E., Walker, S.D., 2013. 4-Gbps uncompressed video transmission over a 60-GHz orbital angular momentum wireless channel. IEEE Wirel. Commun. Lett. 2 (2), 223–226. https://doi.org/10.1109/WCL.2013.012513.120686.

Mari, E., Spinello, F., Oldoni, M., Ravanelli, R.A., Romanato, F., Parisi, G., 2015. Near-field experimental verification of separa-tion of OAM channels. IEEE Antenn. Wireless Propag. Lett. 14, 556–558. https://doi.org/10.1109/LAWP.2014.2369536.

Mohammadi, S.M., Daldorff, L.K.S., Bergman, J.E.S., Karlsson, R.L., Thide, B., Forozesh, K., Carozzi, T.D., Isham, B., 2010. Orbital angular momentum in radio—a system study. IEEE Trans. Antenn. Propag. 58 (2), 565–572. https://doi.org/10.1109/TAP.2009.2037701.

Noor, S.K., Mawardi Ismail, A., Mohd Yasin, M.N., Osman, M.N., Ramli, N., 2022. Orbital angular momentum vortex waves generation using textile antenna array for 5G wearable applications. 2022. IEEE Symp. Wirel. Tech. Appl. (ISWTA). https://doi.org/10.1109/ISWTA55313.2022.9942785.

Perez, N., Preece, D., Wilson, R., Bezryadina, A., 2022. Conservation of orbital angular momentum and polarization through biological waveguides. Sci. Rep. 12, 14144 https://doi.org/10.1038/s41598-022-18483-3.

Wang, J., Liu, J., Li, S., Zhao, Y., Du, J., Zhu, L., 2022. Orbital angular momentum and beyond in free-space optical communications. Nanophotonics 11 (4), 645–680. https://doi.org/10.1515/nanoph-2021-0527.

Weng, Y., Pan, Z., 2023. Orbital angular momentum based sensing and their applications: a review. J. Lightwave Technol. 41 (7), 2007–2016. https://doi.org/10.1109/JLT.2022.3202184.

Willner, A.E., Su, X., Zhou, H., Minoofar, A., Zhao, Z., Zhang, R., Tur, M., Molisch, A.F., Lee, D., Almaiman, A., 2022. J. Opt. 24 (12), 19. https://doi.org/10.1088/2040-8986/ac9c16, 124002.

Xu, X., Mazzinghi, A., Freni, A., Hirokawa, J., 2021. Simulta-neous generation of three OAM modes by using a RLSA fed by a waveguide circuit for 60 GHz-band radiative near-field region OAM multiplexing. IEEE Trans. Antenn. Propag. 69 (3), 1249–1259. https://doi.org/10.1109/TAP.2020.3016428.

Yagi, Y., Sasaki, H., Lee, D., 2022. Prototyping of 40 GHz band orbital angular momentum multiplexing system and evaluation of field wireless transmission experiments. IEEE Access 10, 130040–130047. https://doi.org/10.1109/ACCESS.2022.3228545.

Yuan, T., Cheng, Y., Wang, H., Qin, Y., 2017. Mode characteristics of vortical radio wave generated by circular phased array: theoretical and experimental results. IEEE Trans. Antenn. Propag. 65 (2), 688–695. https://doi.org/10.1109/TAP.2016.2635620.

Zhao, Z., Xie, G., Li, L., Song, H., Liu, C., Pang, K., Zhang, R., Bao, C., Wang, Z., Sajuyigbe, S., Talwar, S., Nikopour, H., Willner, A.E., 2017. Performance of using antenna arrays to generate and receive mm-wave orbital-angular-momentum beams. In: 2017 IEEE Global Comm. Conf. GLOBECOM, Singapore, Singapore, pp. 1–6. https://doi.org/10.1109/GLOCOM.2017.8254906, 2017.

Zhiyuan, X., Zhe, S., Yaochun, S., 2022. Quasi-perfect vortices generated by Pancharatnam-Berry phase metasurfaces for optical spanners and OAM communication. Sci. Rep. 12, 1053. https://doi.org/10.1038/s41598-022-05017-0.

Free-space OAM wave transmission: a short dipole modeling study

A.Ž. Ilić[1], J.Z. Trajković[1], S.V. Savić[2] and M.M. Ilić[2]

[1]*Institute of Physics Belgrade, University of Belgrade, Serbia*
[2]*School of Electrical Engineering, University of Belgrade, Serbia*
e-mail: andjelijailic@ieee.org

Orbital angular momentum (OAM) multiplexing is, since recently, considered to be one of the key technology enablers for enhancing wireless and free-space optical communications channel capacity, whether implemented separately or in combination with existing multiplexing techniques. The OAM wave generation systems have been a topic of a number of recent publications. The actual possibilities and limitations of the free-space OAM wave transmission have also been investigated in several studies, e.g. [1-4]. The results have pointed out the most probable utility of the free-space OAM waves for short-range transmission distances that are on the order of magnitude of the Rayleigh distance. However, there are just a few in-depth investigations into the properties of such short-range OAM wave transmission. Here we report on the recently proposed use of the short (Hertz) dipole method customized for the detailed analysis of the OAM waves [5]. Employing that method and focusing on the uniform circular antenna arrays (UCA), as a very representative example of easily reconfigurable discrete OAM wave sources, we studied the properties of the short-range transmission at different frequencies, for different UCA electrical sizes, and different distances from the source plane [5]. Guidelines for using the proposed methodology and the obtained results in the future designs of free-space communication systems employing OAM multiplexing were provided.

As expected, short (Hertz) dipole modeling proved highly efficient and versatile in an investigation of electrically large discrete OAM EM wave sources. A general framework of combining the short dipole method with full-wave numerical EM modeling for the analysis of arbitrary antenna arrays or other OAM wave radiating structures was also presented.
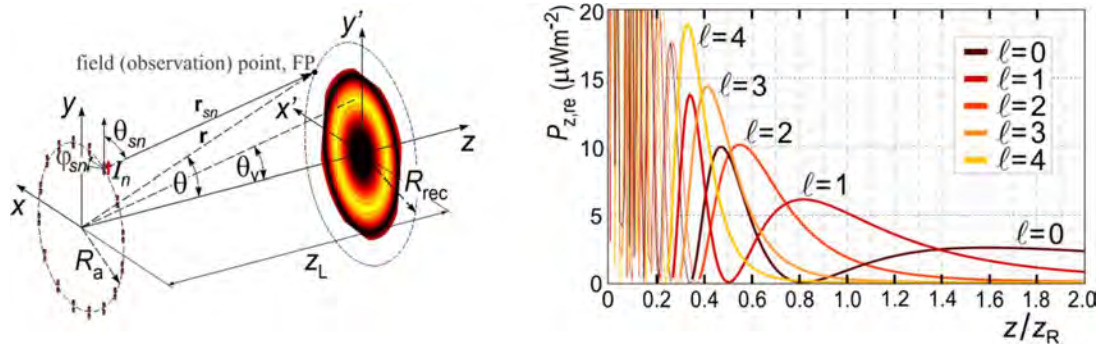

Figure 1. Short (Hertz) dipole modeling, computationally efficient for electrically large discrete EM wave sources (plot on the left). The vortex angle, θ_v, corresponds to the OAM EM field maximum. The link distance is denoted as z_L. Dependence of the axial Poynting vector for $x=0$, $y=R_{rec}=z_L\tan(\theta_v)$, on the distance from the source plane, z, is plotted on the right (R_{rec} represents the radius of receiving UCA). The Rayleigh distance is denoted as z_R. The optimal receiving distance, i.e., link range, corresponds to the axial coordinates of OAM EM field maxima.

REFERENCES
[1] A.F. Morabito *et al.*, IEEE Antennas Propag. Mag. 60, 59 (2018).
[2] A. Sawant *et al.*, IEEE Wirel. Commun. 28, 90 (2021).
[3] A.E. Willner *et al.*, J. Opt. 18, 074014 (2016).
[4] A.Z. Golubović *et al.*, Int. J. Electron. Commun. (AEÜ) 165, 154643 (2023).
[5] A.Ž. Ilić *et al.*, accepted for publication in J. Phys. A: Math. Theor.

OAM mode quality comparisons for discrete EM radiating sources

J.Z. Trajković[1], A.Ž. Ilić[1], S.V. Savić[2], N. Maletić[3], E. Grass[3,4] and M.M. Ilić[2]
[1]Institute of Physics Belgrade, University of Belgrade, Serbia
[2]School of Electrical Engineering, University of Belgrade, Serbia
[3]IHP – Leibniz-Institut für innovative Mikroelektronik, Frankfurt (Oder), Germany
[4]Humboldt-Universität zu Berlin, Berlin, Germany
e-mail: jelena.trajkovic@ipb.ac.rs

Electromagnetic (EM) waves carrying the orbital angular momentum (OAM) are currently being considered for use in optical wireless communications, as well as wireless communications at terahertz and millimeter wave frequencies [1,2]. The apertures radiating with their entire surfaces, often used in the optical domain, produce very high quality OAM EM waves. However, partial radiating apertures and discrete OAM wave sources, considered here, facilitate OAM source reconfiguration as well as multiplexing of different OAM modes through a single aperture. Moreover, at terahertz and millimeter wave frequencies, powering and phasing of discrete OAM EM wave sources often becomes increasingly more complex and costly, especially for a very large number of elements of radiating antenna arrays. Therefore, it is of interest to use low-cost, low-profile, efficiently powered and phased antenna arrays consisting of a limited number of elements, while optimizing the OAM mode quality.
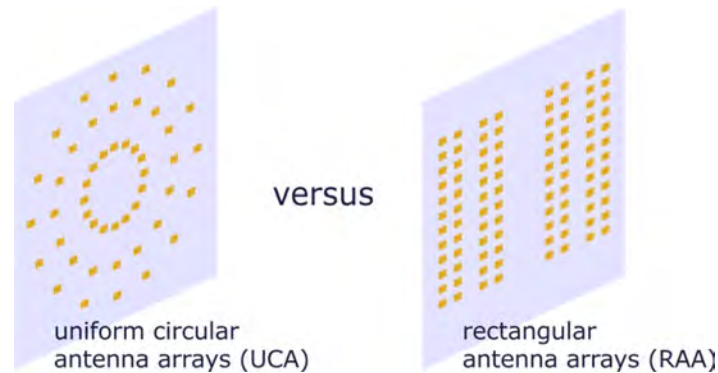

Figure 1. Uniform circular antenna arrays (UCA) are often used to produce the OAM EM waves at millimeter wave frequencies. Rectangular antenna arrays (RAA) could offer some additional flexibility to the designer; however, the calculation of the RAA element phase shifts is more complex, and additional optimization might be required to attain similar OAM mode quality in comparison with the UCA.

Utilization of uniform circular antenna arrays (UCA) as discrete OAM EM wave sources has been successful in the millimeter wave frequency band; phasing of the UCA is quite straightforward and symmetrical antenna arrangements are advantageous from the OAM mode quality viewpoint. However, the OAM EM wave sources for use in wireless communications have to be electrically large [2,3], to allow the desired system performance. From that point of view, either uniform or non-uniform rectangular antenna arrays (RAA) provide additional flexibility to the designer and could benefit from the well-developed theory and implementation methods of conventional antenna arrays [4]. We compare the OAM mode quality of different antenna array arrangements at millimeter wave frequencies to define the prerequisites for the RAA for attaining high wireless data transfer performance.

REFERENCES
[1] A.E. Willner *et al.*, J. Opt. 18, 074014 (2016).
[2] A.Z. Golubović *et al.*, Int. J. Electron. Commun. (AEÜ) 165, 154643 (2023).
[3] A.Ž. Ilić *et al.*, J. Phys. A: Math. Theor. 56, 255701 (2023).
[4] Y.H. Cho, W.J. Byun, Electron. Lett. 55, 503 (2019).

Investigation of the OAM EM wave interaction with tissue at microwave and millimeter wave frequencies

Jelena Trajković[1], Slobodan Savić[2], Milan Ilić[2], Andjelija Ilić[1]

1 Institute of Physics Belgrade, University of Belgrade, Belgrade, Serbia
2 School of Electrical Engineering, University of Belgrade, Belgrade, Serbia

Recently, there has been an increase of interest in use of electromagnetic (EM) waves with helical wavefronts, known as the orbital angular momentum (OAM) waves. The OAM waves are considered to be among the key technological resources to improve optical / wireless communication system capacity and transmission data rates. Additionally, applications in the field of biomedicine have been foreseen, such as medical imaging and diagnosis, deep-tissue imaging, biosensing, and communication with medical implants (doi: 10.1038/s41598-022-18483-3; doi: 10.1038/s41598-021-82033-6; doi: 10.1364/JOSAA.34.002046). Other possible applications include various localized tissue treatments or tissue ablation. The available references mainly study the interaction of OAM light with biological structures, offering some novel insights into the biophotonics effects. Investigations are needed and should also be carried out for other frequency ranges, such as microwaves and millimeter waves. These studies are also important for the design of recently very popular wearable antennas, in the context of body area networks that utilize OAM and the specific absorption rate (SAR) in that case (doi: 10.1109/ISWTA55313.2022.9942785).

Here we use semi-analytical modeling and full-wave numerical computations of OAM EM fields to investigate their interaction with biological tissues. Specifically, we compare the results for various OAM modes by altering the OAM beam parameters and the distance from the target tissue. The output variables of interest include the spot size obtained and the energy delivered to the tissue, expressed in terms of the Poynting vector. We also explore the possibility of combining several OAM modes. The results provide insights into potential biomedical applications of OAM EM waves at the examined frequencies and should guide the design of components and devices based on OAM EM waves.

Transmission and attenuation of the millimeter-wave OAM beams through the layers of tissue

Jelena Trajković[1,2], Slobodan Savić[3], Milan Ilić[3], Andjelija Ilić[1]

1 Institute of Physics Belgrade, University of Belgrade, Belgrade-Zemun, Serbia
2 Faculty of Physics, University of Belgrade, Belgrade, Serbia
3 School of Electrical Engineering, University of Belgrade, Belgrade, Serbia

The orbital angular momentum (OAM) waves, from microwave and millimeter waves to optical frequencies have lately been recognized as one of the key technological enablers of high-data-rate wireless communications. Given their planned use in short-distance line-of-sight (LoS) application scenarios in B5G / 6G wireless communications, such as immersive extended reality (IXR) or wearable antennas / monitoring devices within the body-area networks (doi: 10.1007/978-3-030-72777-2_6; doi: 10.1109/ISWTA55313.2022.9942785), it is important to study the interaction of OAM waves with tissue. Moreover, the OAM waves have been proposed for medical imaging and diagnosis, deep-tissue imaging, biosensing, and communication with medical implants (doi: 10.1038/s41598-021-82033-6; doi: 10.1364/JOSAA.34.002046). Our previous study addressed the amounts of EM energy which can be delivered to the tissue surface, in terms of the Poynting vector obtained under the various specified conditions (doi: 10.1016/j.apradiso.2024.111261). There, biomedical applicator designs aiming at localized tissue treatments or tissue ablation by OAM beams were proposed.

In this work, we consider different OAM beam parameters and different properties of tissue layers, aiming at the detailed analysis of the effects of propagation of OAM waves through the biological tissue. The investigation is carried out utilizing full-wave numerical simulations of OAM EM fields. Attention is particularly directed to the attenuation of different OAM modes during propagation with various initial vortex angles, possible decrease in OAM mode quality, and amounts of energy delivered to the tissue layers. The results could guide the design of components utilizing mutually orthogonal OAM modes for biomedical or communication purposes.

New experimental setup for exposure of gas-phase bio-aerosols to small air ions

Stefan Mijatović[1], Irena Aranđelović[1], Andrea Radalj[2],
Marko Janković[1], Stefan Đoković[2], Jelena Trajković[3], Anđelija Ilić[3], Predrag Kolarž[3]

1 Faculty of Medicine, University of Belgrade, Belgrade, Serbia
2 Faculty of Veterinary Medicine, University of Belgrade, Belgrade, Serbia
3 Institute of Physics Belgrade, Belgrade, Serbia

The COVID-19 pandemic has once again steered the attention of the public to not only medical but also economic and societal problems, caused by airborne microorganism infections. As one of the means of controlling airborne pathogens, there has been a revived interest in using air ionizers to purify the indoor air in closed spaces. The major benefit of newer corona air ionizers stems from the use of carbon fibres to produce small air ions without the harmful side effect of producing ozone (doi: 10.1080/02786820802339553). In addition to speeding up the natural deposition of particles in the air (doi: 10.1016/j.jaerosci.2023.106199), including the bio-aerosol particles, small air ions have been reported also to produce a biocidal action on airborne microorganisms (doi: 10.1186/1471-2180-7-32, doi: 10.1016/j.jhin.2022.04.004, doi: 10.1128/Spectrum.00651-21). In order to perform a detailed study of the effects of small air ions to the gas-phase bio-aerosol, we have developed a dedicated experimental setup for bio-aerosol exposure, able to provide accurate measurements even with moderate bio-aerosol concentrations.

Here we describe the newly invented air ion exposure setup and its principles of work. We report on the experiments with *Aspergillus fumigatus* and *Mycobacterium gordonae*. We study the effects of air ions of different air ion concentrations, polarity ratios, and exposure times. The increased efficiency of particle deposition as well as the noticed biocidal effects are reported.

In vitro experimental model of reactivated toxoplasmosis through the prism of computational image analysis

Jelena Trajković[1], Andjelija Ilić[1], Jelena Srbljanović[2], Olivera Lijeskić[2], Neda Bauman[2], Đorđe Zlatković[2], Dragana Vujić[3,4], Vladimir Dobričić[5], Branko Bobić[2], Tijana Štajner[2]

1 Institute of Physics, University of Belgrade, Zemun, Belgrade, Serbia
2 National Reference Laboratory for Toxoplasmosis, Group for Microbiology and Parasitology, Centre of Excellence for Food- and Vector-borne Zoonoses, Institute for Medical Research, National Institute of Republic of Serbia, University of Belgrade, Belgrade, Serbia
3 Faculty of Medicine, University of Belgrade, Belgrade, Serbia
4 Mother and Child Health Care Institute of Serbia "Dr Vukan Čupić", Belgrade, Serbia
5 Department of Pharmaceutical Chemistry, Faculty of Pharmacy, University of Belgrade, Belgrade, Serbia

Computational image analysis has recently gained increased importance in medical research and diagnostics. Precisely established tissue and cell properties, resulting from dedicated image analyses, are quantitative, repeatable, and free from subjective judgement bias possible with human observers. We were the first group to apply fractal analysis for the description of structural complexity of *Toxoplasma gondii* tissue cysts, in combination with the morphological and particle analyses (doi.org/10.1371/journal.pone.0234169). The majority of analyzed parameters were stable among cysts, indicating a highly uniform structure and occupancy of the *T. gondii* brain cysts of different age and parasite strains, as well as of those derived from mice of different genetic background.

In this work, we present the results of our most recent investigation in this field. Photographs of the *in vitro* conversion of bradyzoites to tachyzoites simulating reactivated toxoplasmosis (RT) in an immunocompromised host, but also cellular invasion and intracellular proliferation (parasitophorous vacuole, rosettes, etc.), will be obtained in experimental settings with (sulfadiazine and/or acridines/acridones) and without (control group) treatment. High resolution digitalized microscopic images will be analyzed using the ImageJ software. The optimization of the morphological, particle, and fractal analyses to the acquired data, as well as investigation of usefulness of other methods, e.g. texture analysis will be carried out.